UNIVERSITY OF OSLO
Department of
Mathematics

Wave–current interactions in coastal tidal currents

PhD Thesis

by
Karina Bakkeløkken Hjelmervik

*"He alone stretches out the heavens,
and treads on the waves of the sea."*

Job 9:8

Preface

There are four papers making up my thesis. I am the first author of all papers, though with substantial contributions, comments, and corrections from the co–authors.

The first paper is a technical report which describes the implementation of nonlinear advection terms in a high resolution tidal model, some sensitivity tests, and validations. The numerical model is written in Fortran77. I have been responsible both for the implementation and the simulations, while co–authors have guided the research work and duplicated some of the simulations for control.

The second paper is an article submitted to *Ocean Dynamics*. This article is a summary of a cooperative research project where I am mainly responsible for the first part concerning tidal currents, and Birgit Kjoss Lynge for the second part concerning storm surges.

The third paper is a technical report which describes the derivation of current–modified nonlinear Schrödinger equations, a corresponding numerical model, and some results. The numerical model is written in C. I am responsible for the derivation, the numerical model, and the simulations. An extract of this paper is submitted as a proceeding for the Rogue Wave workshop in Brest 2008.

The fourth paper is an article submitted to *Journal of Fluid Mechanics*. Here specific results concerning waves on collinear currents are presented. I am responsible for the derivation, the numerical model, and the simulations.

Acknowledgement

It is a privilege to work with my supervisors, Professor Karsten Trulsen and Professor Bjørn Gjevik. Their deep insight and solid guidance have navigated me safely through my thesis. I strongly appreciate their help and support.

I would like to thank colleagues at the Institute of Mathematics for giving me the chance and following me up on my PhD–work. Particularly Atle Ommundsen at FFI, and Phd–students Birgit Kjoss Lynge and Odin Gramstad deserve gratitude for fruitfull discussions and co–working. A few words of thanks is addressed pilot master Andor Antonsen at Lødingen pilot station for relevant information.

I am grateful for the encouragement and knowledge my teachers have offered me since I was seven until I finished my cand. scient. at the University of Bergen under the excellent guidance of professor Peter Haugan. The important work of teachers and supervisors at all levels should not be underestimated in any case.

I also acknowledge the encouragement from my whole family including my in–laws. You have all believed in me. I am especially grateful to my parents for their constant support and for urging me to independent thoughts. I would not have made it this far without my inherited determination and mantra of never giving up. Special gratitude also goes to my husband, Karl Thomas. Words can not describe what your support, love, stability, and patience mean to me on a daily basis. Finally I thank my three kids, Mathias, Anne Maline, and May Alise for sharing their childlike wisdom and earnest joy of life.

Contents

Paper 1   Hjelmervik, K., Ommundsen, A. & Gjevik, B. 2005
Implementation of non–linear advection terms in a high resolution tidal model.
University of Oslo, preprint.

Paper 2   Hjelmervik, K., Lynge, B. K., Ommundsen, A. & Gjevik, B. 2008
Interaction of tides and storm surges in the Tjeldsund channel in northern Norway.
Ocean Dynamics (submitted).

Paper 3   Hjelmervik, K. & Trulsen, K. 2009
New current modified Schrödinger equations.
University of Oslo, preprint.

Paper 4   Hjelmervik, K. & Trulsen, K. 2009
Freak wave statistics on collinear currents.
Journal of Fluid Mechanics (accepted).

"But the expressions must not be applied too literally, for that
would imply that the tidal wave behave as it ought to do;
. . . which is not the case."
Unna (1947)

Introduction

Almost 100 ships were piloted safely through the beautiful Tjeldsund channel during June and July 2008. The longest cruise ship was "Albatros", 205.46 meters long with a draught of 7.75 meters. Particularly the narrow sections of the Tjeldsund channel is prone to strong tidal currents, and therefore difficult to pilot large ships through. The effect of squat is large for such long ships in shallow water. Strong currents create an area of lowered pressure under the keel and reduces the buoyancy of the ship, particularly at the bow. The squat effect can thereby lead to unexpected groundings and handling difficulties. The local pilots have generations of experience starting early in the 1900s.

The surrounding mountains protect the Tjeldsund channel from strong winds producing large waves in ocean current regions. An example of difficult sailing conditions due to wave–current interaction is found in the strong tidal currents around the Lofoten Islands in northern Norway (Gjevik *et al.*, 1997). The most spectacular example is in the region close to the south–east coast of South Africa, where waves originating from the Antarctic Ocean are trapped in the relatively narrow and strong Aghulas current headed south–west. Many sailors taking advantage of strong westward ocean currents were unaware that they headed for the most extreme waves (Mallory, 1974). Further examples include the navigation in outlets from fjords or rivers, where the combination of incoming waves and outgoing tides cause difficult sailing conditions (The Norwegian Pilot 1, 1997; González, 1984; Bottin & Thompson, 2002). On the 13th of February 2000 a high–speed passenger ferry going out through the mouth of the Trondheimsfjord suffered an accident caused by steep waves. The steepness was probably due to wave–current interaction. The front window of the passenger salon was broken by a large wave (*Verdens Gang*, 14 February 2000).

High resolution models for prediction of tidal currents have recently been developed partly motivated by the navigational problems often experienced in Norwegian coastal waters (e.g. Moe *et al.*, 2002, 2003). Tidal currents can now be computed with down to 25 meter resolution, which is comparable to wavelengths associated with a typical wind–wave spectrum.

Given the high resolution current modelling, modelling of wave–current interactions may now enter a new era. It is meaningful to consider the deterministic nonlinear phase–resolved evolution of wind–wave fields in coastal tidal currents. This can be realized in at least two different manners: Predicting the deterministic phase–resolved evolution of specific realizations of a wind–wave field, or the simulation of a large ensemble of deterministic evolutions of stochastic wind–wave fields. The latter approach may lead to a statistical description of wave

Figure 1: *The cruise ship "M/S Funchal" passing through the Tjeldsund channel 23 June 2007.*
"M/S Funchal" was built in 1961. It is 153.51 meters long and 19 meters wide.
The photo is taken southwards by the bridge at Steinsland. Here the channel is wide (≈ 1 km) with weak currents (< 0.1 m/s). The channel is more narrow (down to 0.5 km) with stronger currents (up to 3 m/s) in other parts of the channel.

Photo: Ingrid Bakkeløkken.

conditions in coastal waters with an unprecedented level of accuracy, and can possibly lead to the description of local wave properties beyond the capabilities of todays spectral wave models (STWAVE, SWAN, etc.).

The work with this thesis is organised as two interconnected tasks:

- Numerical modelling of tidal currents in Norwegian coastal waters.

- Modelling of wave transformation in tidal currents due to wave–current interaction.

During the first task the nonlinear advection terms are implemented in a high resolution coastal tidal model. The model is set up for the Tjeldsund and Ramsund channels in northern Norway. Various methods for implementation of the nonlinear advection terms is tested and effects on nonlinear flow features as jet and eddy formation is studied. This work is reported in a *preprint report* published at Department of Mathematics, UiO, (Paper 1), and an article submitted to *Ocean Dynamics* (Paper 2).

From the results of tidal modelling for the Tjeldsund and Ramsund channels, models with idealised bottom topography and coastlines are designed in order to study special important features of the tidal currents in coastal waters. Then idealised currents are designed and used to model wave–current interaction in the second task.

Our starting point for modelling nonlinear phase–resolving wave–current interactions was to use higher–order nonlinear Schrödinger equations (Dysthe, 1979; Trulsen *et al.*, 2000) properly modified to account for space varying currents. The higher–order nonlinear Schrödinger equation already account for wave–current interactions, although limited to currents induced by the waves themselves. Extension to surface currents due to internal waves or other causes was done by Dysthe & Das (1981) and Stocker & Peregrine (1999). Different configurations require different treatments: angle of incidence, shearing or potential current, include or exclude reflection, etc. A nonlinear Schrödinger equations is derived for waves on both potential and shearing collinear currents. This work is reported in a *preprint report* published at Department of Mathematics, UiO, (Paper 3), and an article submitted to *Journal of Fluid Dynamics* (Paper 4).

Figure 2: *Wave breaking in the convergence zone of a tidal front in the Fraser Estuary in British Columbia, Canada (Baschek, 1999).*
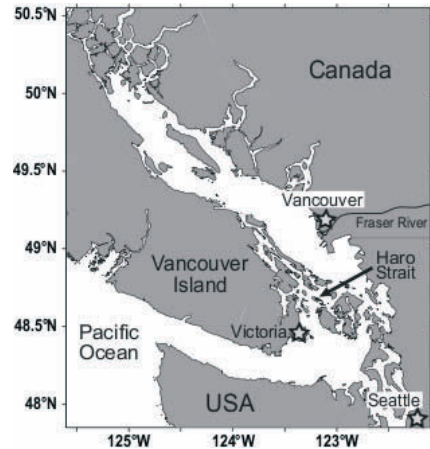
1 Tidal modelling

The first version of the tidal model used in this project, was developed in the early 1990s and used for simulations of tides in the Norwegian and Barents Sea (Gjevik, 1990; Gjevik *et al.*, 1994). More recently an upgraded version of the model has been used for simulation of tides around the Lofoten islands with a horizontal grid resolution of 500 meters (Moe *et al.*, 2002) and in the outer Trondheimsfjord with a horizontal grid resolution of 50–100 meters (Moe *et al.*, 2003; Gjevik *et al.*, 2006). The tidal model is built on the depth–integrated shallow water equations suitable for tidal currents in well–mixed coastal waters. The nonlinear advection terms were neglected.

In 2004 the University of Oslo was hired by the Norwegian Defence Research Establishment to set up the model for the Tjeldsund and Ramsund channels east of the Lofoten Islands in northern Norway (Hjelmervik *et al.*, 2006). To model the tidal currents in these narrow and shallow channels, the nonlinear advection terms clearly had to be included. In narrow straights and channels with strong tidal currents it is well known that nonlinear effects can lead to eddies and nonlinear distortion of shallow water tides. The challenge was to find robust and accurate numerical schemes which are stable, even with complex coastlines and bottom topography, without introducing too strong smoothing or damping of the current fields. Due to one sided differences the nonlinear advection terms are approximated along the coastline. Several methods for including the nonlinear advection terms in the original tidal model have been tested.

When the nonlinear advection terms were included, the simulated current fields showed an intricate system of intensified jets and eddies (see example in figure 3). Both propagating and topographically trapped eddies where discovered. Some of the eddies are described in The Norwegian Pilot 1 (1997) and observed by inspection. To validate the model, both elevation and current measurements are carried out and analysed (Lynge, 2004; Lynge & Hareide, 2005), and then compared with simulations.

Simulated current fields are displayed in Geographical Information System (GIS) tools and network browsers, and thus made available for operational use by the Navy during several military operations; Armatura Borealis 2008, Cold Respons 2006, and November 2005 (Ommundsen *et al.*, 2005). As a pilot project, current fields are also implemented in electronic chart
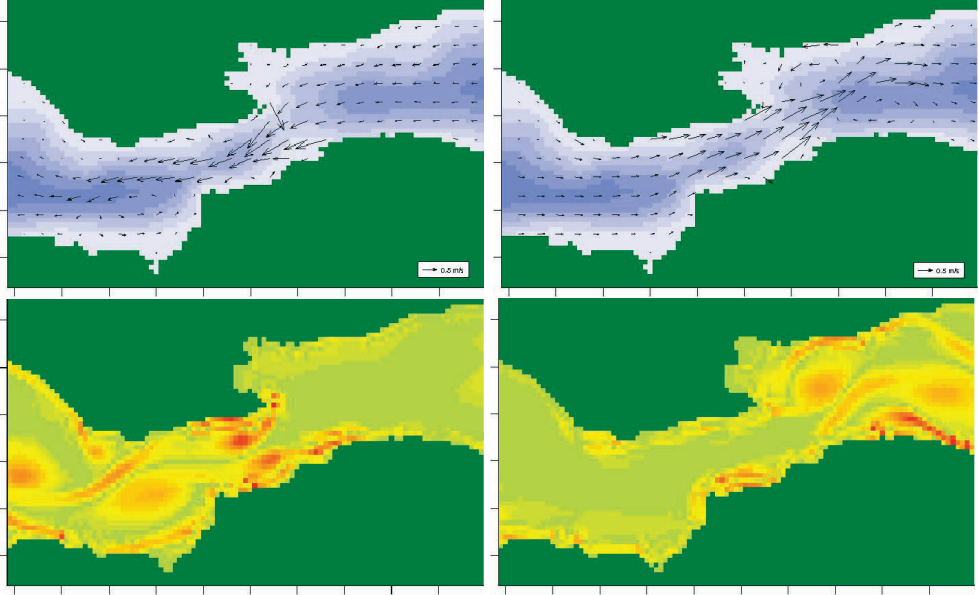
Figure 3: *Simulated current (upper) and vorticity (lower) fields at maximum flow westward (left) and eastward (right) near Ballstad in the Tjeldsund channel. The distance between the tick marks correspond to 500 meters. Near Ballstad the cross section area is reduced to one fourth, the current is doubled, and the surface elevation is reduced by about five percent over a length scale of 1000 meters. The maximum value of the current strength lies around 1.00 ms^{-1} and the maximum value of the vorticity lies around 0.30s^{-1}. The stronger vorticity the more red. With westward flow, a topographically trapped eddy appears southeast of the intensified current jet, while a propagating eddy appears northwest of the jet. With eastward flow, a topographically trapped eddy appears northwest of the intensified current jet, while a propagating eddy appears southeast of the jet. (Further details in paper 3.)*

systems (Gjevik *et al.*, 2006).

The flow pattern in the Tjeldsund channel is quite complex. To better understand the current fields, long idealised channels with different sills and narrow passages where designed (figure 4). Such constrictions lead to strong gradients in the current field with possible formation of eddies and will therefore affect wind waves and swell significantly. It was found that the length of the narrow passage was of minor importance, but steepness and height of the sill have large impact on the current strength.

Since the current fields in idealised channels are still quite complex, an idealised current jet, $\boldsymbol{U} = U(x,y)\boldsymbol{i}$, without eddies was designed:

$$U = \begin{cases} U_0 \sin^2\left(\frac{\pi x}{2X}\right) \cos^2\left(\frac{\pi y}{2Y}\right) & \text{when } x < X \\ U_0 \cos^2\left(\frac{\pi y}{2Y}\right) & \text{when } x \geq X \end{cases} \tag{1}$$

U_0 is the maximum current strength, Y is half the width of the jet, and X is the current build–up length. To a certain extend (1) mimics the current jet in figure 5.

Current jets with different widths, strengths, forms, and build–up lengths are found not only
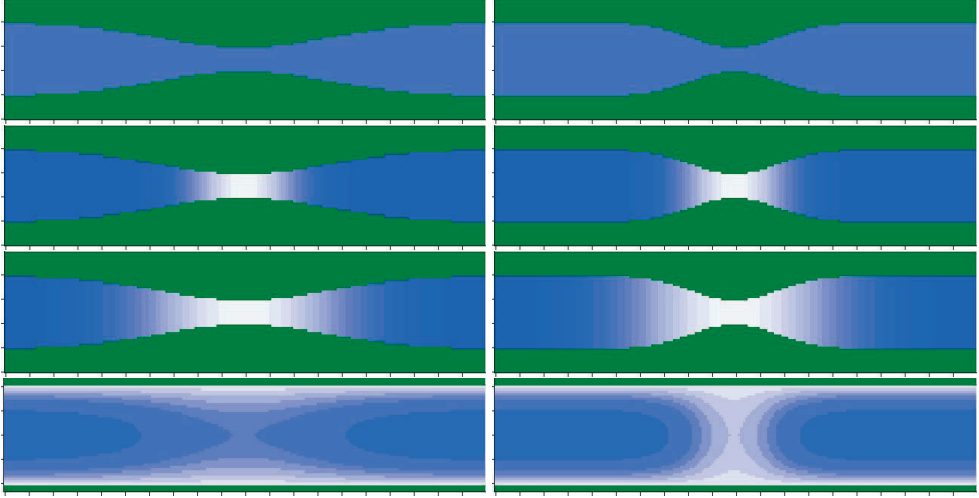
4

Figure 4: *Different constrictions in some idealised channels (east–west length 100 km). The constrictions are sills and/or narrow passages. The depth is uniform ($h = 100m$) except for the sills where the depth is remarkable reduced ($h_{sill} = 20m$ in the above examples). The space between the tick marks represent 500 meters. The maximum strength of the current through a narrow passage depends on the width of the passage and the steepness of the sill.*

Figure 5: *Example of a current field over a sill in an idealised channel with U–formed bottom. The current is more uniform upstream from the constriction. The flow separation at the constriction results in a narrow current jet with eddies on each side after the constriction.*
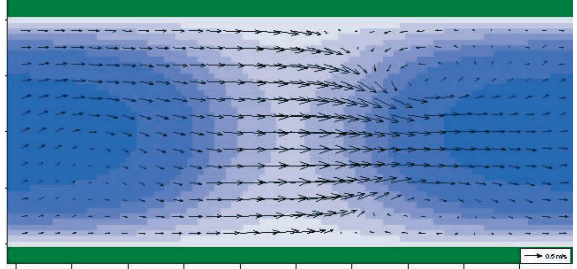
in tidal flows in the coastal zone, but also in river estuaries, entrances in fjords during outgoing tides, rip off currents, and large ocean currents like the Aghulhas and Kuroshio current. In accordance with data the transverse profile of the velocity distribution current $\boldsymbol{U} = U(y)\boldsymbol{i}$ in the Aghulhas current can be approximated by the relation (Schumann, 1976; Lavrenov, 1998):

$$U = \frac{\alpha}{1 + \beta y^2} \tag{2}$$

$\alpha = 2.2$m/s and $\beta = 6.26 \cdot 10^{-10}$m^{-2} for $y > 0$, and $\beta = 10^{-8}$m^{-2} for $y < 0$. (2) gives an asymmetric jet. A symmetric jet like (1) is easier to handle.

2   Wave–current interactions

Rogue waves, also known as freak waves, monster waves or extreme waves, are relatively large and spontaneous ocean surface waves that are a threat even to large ships, ocean liners, and
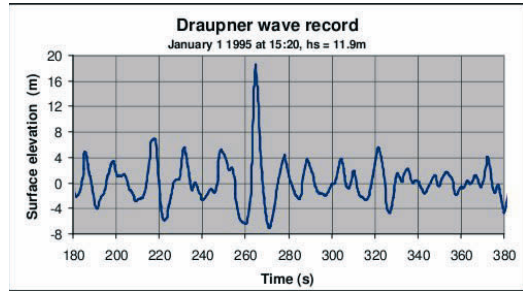
Figure 6: *The Draupner wave is the first rogue wave detected by a measuring instrument. It was measured at Draupner oil platform in the North Sea off the coast of Norway on January 1, 1995 (Haver, 2003). The Draupner wave had a maximum wave height of 25.6 meters and occurred in a sea state with a significant wave height of 11.9 metres. Minor damage was inflicted on the platform during this event, confirming the validity of the reading made by a downwards–pointing laser sensor. Prior to this measurement, freak waves were known to exist only through anecdotal evidence provided by those who had encountered them at sea.*

offshore installations. There is no unique definition of rogue waves, but it is generally agreed that they belong to the extreme tail of the probability distribution. The most common definition is that a wave is freak when its wave height exceeds a threshold related to the significant wave height. Therefore rogue waves are not necessarily the biggest waves found at sea. Rogue waves are surprisingly large waves for a given sea state. Two important reviews of rogue waves have been published (Kharif & Pelinovsky, 2003; Dysthe *et al.*, 2008).

There are several theories on what causes rogue waves to appear. It is well known that wave–current interactions can provoke large waves and cause navigational problems, e.g. in the Aghulas current, river estuaries, rip currents, entrances in fjords during outgoing tides, and in tidal flows in the coastal zone (**?**Peregrine, 1976; González, 1984; Jonsson, 1990; Lavrenov, 1998; Baschek, 1999; Bottin & Thompson, 2002; Mori *et al.*, 2002; MacMahan, Thornton & Reniers, 2006).

Short gravity waves, when superposed on much longer waves of the same type, have a tendency to become both shorter and steeper at the crests of the longer waves, and correspondingly longer and lower in the troughs (**?**). Linear refraction occur when the velocity of the opposing current equals the stopping velocity, $U = -\frac{g}{4\omega}$, (Peregrine, 1976; White & Fornberg, 1998, and others).

Laboratory measurements of long crested waves on a transversally uniform current show that strong opposing currents induce partial wave blocking significantly elevating the limiting steepness and asymmetry of freak waves (Wu & Yao, 2004). Experimental studies of interactions between waves and collinear current jets are difficult due to the lack of suitable facilities. (Baschek, 1999) argued that tidal fronts are natural laboratories for studying wave–current interactions. Recordings from the coast of Cornwall, England, show fluctuations of ± 1 second in wave period of swells with wave velocity of 30 m/s (Barber & Ursell, 1948; Barber, 1949). The fluctuations are due to time changing tidal currents of ± 0.5 m/s. The wave period is longer for waves on co-currents than on counter currents.

Several different equations are used to study wave–current interactions. Phase–resolved

Figure 7: *The significant wave height, kurtosis, and amount of freak waves across an idealised current jet given by (1) shortly after the build–up. In this case, the jet is three wave lengths wide, the build–up is 16 wave lengths long, and the maximum current strength is 20% of the phase velocity of the waves. The incoming waves are unidirectional with random phase and Gaussian distributed Fourier amplitude of the envelope. Monte Carlo simulations are performed with a second order scheme and 30 simulations in each ensemble.*
Kurtosis and amount of freak waves is reduced with shorter crest lengths, in linear simulations, and when the waves are adjusted to the current jet.
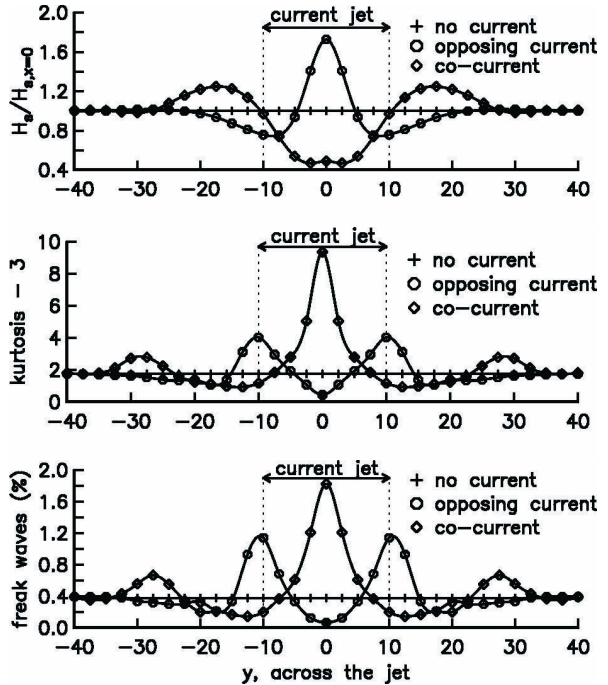
models as Schrödinger equations, are preferred when studying wave statistics. Most current modified Schrödinger equations in literature has only one horizontal dimension, are built on potential theory, or both (Stewartson, 1977; Turpin *et al.*, 1983; Gerber, 1987; Stocker & Peregrine, 1999; Dysthe, 1979). When considering an inhomogeneous current with horizontal shear, potential theory cannot be used since vorticity in the current field introduces vorticity in the induced flow of the waves. Therefore a new current–modified cubic Schrödinger equation which allows vorticity in the induced flow had to be derived. A split–step scheme is used in the numerical simulations using both Fourier methods and finite difference methods (Lo & Mei, 1985; Weidman & Herbst, 1986; Stocker & Peregrine, 1999). Fourier methods are used on the linear terms with constant coefficients. Finite difference methods are used on the nonlinear term and the linear terms with variable coefficients. A first, second, and fourth order scheme is implemented and properly checked following Muslu & Erbay (2004).

Interesting properties as distributions of elevation, wave heights, and freak waves are studied for waves encountering both a transverse uniform current, and a collinear current jet. Surface gravity wind–waves will typically have periods 5–10 seconds, while the main period of tidal currents is about 12 hours. The current is therefore assumed stationary in our study. The current is also assumed negligible affected by the waves. Of primary interest are relatively steep surface waves, such that a linear description would be insufficient. It is anticipated that the direct influence from topography and bathymetry is much weaker than the influence from tidal currents and nonlinear self interactions.

The statistical wave properties are calculated from averaging over ensembles of realizations. When waves propagate on inhomogeneous currents, spatial averaging at fixed times do not
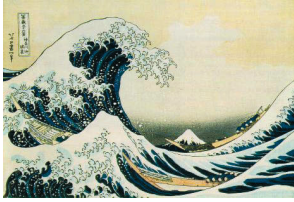
Figure 8: *"The Great Wave" by Katsushika Hokusai (1760–1849), Japanese artist. The wood block print portrays a grand struggle between man and nature. Earlier in situ experience was the only weapon against the violence of nature. Now numerical simulations contribute to the experience.*

equal time averaging at fixed locations. To avoid averaging over inhomogeneous currents and ensure that freak waves belong to the upper tail of the probability distribution, we recommend to use time series at fixed locations with constant current as data basis for the statistical wave properties. The current is not constant at fixed locations in tidal currents and fluttering ocean currents such as the Aghulas current and the Gulf Stream. In such cases new ensembles of wave realizations are needed for each realization of the current in order to calculate the statistical wave properties for a given current case.

It is found that we are less likely to encounter freak waves in the centre of an opposing current jet than in the ocean elsewhere (figure 7). The amount of freak waves are large at the sides of an opposing jet and in the centre of a co–current jet. Freak waves are not high waves in general, but surprisingly high waves for a certain sea state. The amount of freak waves is well represented by the kurtosis. In linear simulations very few freak waves are found. Finally it is found that the wave statistics in the centre of a current jet cannot be represented by simulations with a transversally uniform current.

Note that we have not included wave generation by wind (e.g. SWAN). Phase–resolved evolution takes place on much faster scales than wind–growth of waves, and standard spectral wave models (WAM, SWAM) assume wind–growth to take place on the slow scales of spectrally averaged evolution.

3   Summary

A high resolution tidal model is set up and adjusted to the narrow and shallow Tjeldsund and Ramsund channels in northern Norway. Over tides, intensified jets, and eddy structures appear in the current fields of fully nonlinear simulations. Some comparisons with field measurements are done.

Nonlinear Schrödinger equations are derived to include the effects of inhomogeneous currents in order to study impacts on a wave field from coastal tidal currents. Distributions of wave heights, kurtosis, and amount of freak waves are studied. Linear refraction increase the wave heights in opposing currents. Nonlinear effects prove to have a large effect on the amount of freak waves. Extreme waves are normal in current jets, and therefore not freak or unexpected.

Accurate tidal current forecasting may improve the safety of sailing and reduce the risk for ship collisions and groundings. Predictions may also prove valuable during clean–up operations after oil–disasters, search, and surveillance operations during ship accidents. Wave–current interactions introduce additional complication for safe sailing, and forces on offshore installations. Better wave and current forecasting is desired for both economical and safety reasons.

Bibliography

BARBER, N. F. 1949 The behaviour of waves on tidal streams. *Proc. Roy. Soc.* A, **198**, 81–93.

BARBER, N. F. & URSELL, F. 1948 The generation and propagation of ocean waves and swell. I. Wave periods and velocities. *Phil. Trans.* A, **240**, 527–560.

BASCHEK, B. 1999 Wave–current interaction in tidal fonts. *Woods Hole Oceanographic Institution, MA, USA, preprint.*

BOTTIN, R. R. JR. & THOMPSON, E. F. 2002 Comparisons of physical and numerical model wave predictions with prototype data at Morro Bay harbor entrance, California. *U. S. Army Engineer.*

DYSTHE, K. B. 1979 Note on the modification to the nonlinear Schrödinger equation for appli–cation to deep water waves. *Proc. R. Soc. Lond. A* **369**, 105–114.

DYSTHE, K. B. & DS, K. P. 1981 Coupling between a surface–wave spectrum and an internal wave: modulational interaction. *J. Fluid Mech.*, **104**, 483–503.

DYSTHE, K. B., KROGSTAD, H. E. & MÜLLER, P. 2008 Oceanic Rogue Waves. *Annu. Rev. Fluid Mech.* **40**, 287–310.

GERBER, M. 1987 The Benjamin–Feir instability of a deep water Stokes wavepacket in the presence of a non–uniform medium. *J. Fluid Mech.* **176**, 311–332.

GJEVIK, B. 1990 Model simulations of tides and shelf waves along the shelves of the Norwegian–Greenland–Barrents Seas. *Modelling Marine Systems*, **I**, 187–219. Ed. A. M. Davies, CRC Press Inc. Boca Raton, Florida.

GJEVIK, B., HAREIDE, D., LYNGE, B. K., OMMUNDSEN, A., SKAILAND, J. H., & URHEIM, H. B. 2006 Implementation of high resolution tidal current fields in electronic chart systems. *Journal of Marine Geodesy*, **29**, No 1, 1–17.

GJEVIK, B., MOE, H. & OMMUNDSEN, A. 1997 Souces of the Maelstrom. *Nature*, **388**, 837–838.

GJEVIK, B., NØST, E., & STRAUME, T. 1994 Model simulations of the tides in the Barents Sea. *J. Geophysical Res.*, **99**, No C2, 3337–3350.

GONZÁLEZ, F. I. 1984 A case study of wave–current–bathymetry interactions at the Columbia river entrance. *J. Phys. Oceanogr.* **14**, 1065–1078.

HAVER, S. 2003 Freak wave event at Draupner jacket January 1 1995. *Statoil.*

HARSTAD TIDENDE *Norwegian newspaper.*

HJELMERVIK, K., OMMUNDSEN, A. & GJEVIK, B. 2006 Model simulations of tidal currents in Tjeldsundet and Ramsundet – End report, (in norwegian). *Preprint series*, Department of Mathematics, University of Oslo.

JONSSON, I. G. 1990 Wave–current interactions. In *The Sea, Ocean Eng. Sci.* (ed. by B. Le Méhauté & D. M. Hanes), pp. 65–120, Wiley–Interscience, Hoboken, N. J.

KHARIF, C. & PELINOVSKY, E. 2003 Physical mechanisms of the rogue wave phenomenon. *Eur. J. Mech. B/Fluids* **22**, 603–634.

LAVRENOV, I. V. 1998 The wave energy concentration at the Agulhas current off South Africa. *Natural Hazards* **17**, 117–127.

LO, E. Y. & MEI, C. C. 1985 A numerical study of water–wave modulation based on a higher–order nonlinear Schrödinger equation. *J. Fluid Mech.* **150**, 395–416.

LONGUET–HIGGINS, M. S. & STEWART, R. W. 1961 The changes in amplitude of short gravity waves on steady non–uniform currents. *J. Fluid Mech.* **10**, 529–549.

LYNGE, B. K. 2004 Water level observations from Tjeldsundet January – March 2004, Report DAF 04–2. *Norwegian Hydrographic Servide, Stavanger, Norway*.

LYNGE, B. K.& HAREIDE, D. 2005 Current and sea level observations from Tjeldsundet, November 2004–April 2005, Report DAF 05–3. *Norwegian Hydrographic Servide, Stavanger, Norway*.

MACIVER R. D., SIMONS, R. R. & THOMAS, G. P. 2006 Gravity waves interacting with narrow jet–like current. *J. Geophys. Res.* **111**, C03009.

MACMAHAN, J. H., THORNTON, E. B. & RENIERS, A. J. H. M. 2006 Rip current review. *Coastal Engineering* **53**, 191–208.

MALLORY, J. K. 1974 Abnormal waves in the sourth–east coast of South Africa. *Int. Hydrog. Rev.* **51**, 89–129.

MOE, H., GJEVIK, B. & OMMUNDSEN, A. 2002 A high resolution tidal model for the area around the Lofoten islands. *Continental Shelf Research*, **22**, 485–504. *IEEE Trans. Geosci. Remote Sens.* **42**, 1149–1160.

MOE, H., GJEVIK, B. & OMMUNDSEN, A. 2003 A high resolution tidal model for the coast of Møre and Trøendelag, Mid–Norway. *Norwegian Journal of Geography* **57**, 65–82.

MORI, N., LIU, P. C. & YASUDA, T. 2002 Analysis of freak wave measurements in the sea of Japan. *Ocean Engineering* **29**, 1399–1414.

MUSLU, G. M. & ERBAY, H. A. 2004 Higher–order split–step Fourier Schemes for the generalized nonlinear Schrödinger equation. *Mathematics and Computers in Simulation* **67**, 581–595.

OMMUNDSEN, A., HJELMERVIK, K. & GJEVIK, B. 2005 Tidevannstrømmen i Tjeldsund–Ramsund, 1.–3. november 2005, (in norwegian). *Norwegian Defence Research Establishment*, FFI/NOTAT–2005/03188

PEREGRINE, D. H. 1976 Interaction of water waves and currents. *Adv. Appl. Mech.* **16**, 9–117.

NORWEGIAN HYDROGRAPHIC SERVICE 1997 The Norwegian Pilot 1. *Norwegian Hydrographic Service, Stavanger, Norway*.

SCHUMANN, E. H. 1976 High waves in the Aghulhas Current. *Mariners Weather Log.* **20**(1), 1–5.

STEWARTSON, K. 1977 On the resonant interaction between a surface wave and a weak surface current. *Mathematika* **24**, 37–49.

STOCKER, J. D. & PEREGRINE, D. H. 1999 The current–modified nonlinear Schrödinger equation. *J. Fluid Mech.* **399**, 335–353.

TRULSEN, K., KLIAKHANDLER, I., DYSTHE, K. B., & VELARDE, M. G. 2000 On weakly nonlinear modulation of waves on deep water. *Phys. Fluids*, **12**, 2432–2437.

TURPIN, F–M., BENMOUSSA, C. & MEI, C. C. 1983 Efects of slowly varying depth and current on the evolution of a Stokes wavepacket. *J. Fluid Mech.* **132**, 1–23.

UNNA, P. J. H. 1947 Sea waves. *Nature* **159**, 239–242.

VERDENS GANG *Norwegian Newspaper.*

WEIDMAN, J. A. C. & HERBST, B. M. 1986 Split–step methods for the solution of the non-linear Schrödinger equation. *SIAM J. Numer. Analy.* **23**, 485–507.

WHITE, B. S. & FORNBERG, B. 1998 On the chance of freak waves at sea. *J. Fluid Mech.* **335**, 113–138.

WU, C. H. & YAO A. 2004 Laboratory measurements of limiting freak waves on currents. *J. Geophys. Res.* **109**, C12002.

Paper 1

Implementation of nonlinear advection terms in a high resolution tidal model

IMPLEMENTATION OF NONLINEAR ADVECTION TERMS IN A HIGH RESOLUTION TIDAL MODEL

Karina Hjelmervik[(1)], Atle Ommundsen[(2)], Bjørn Gjevik[(1)]

(1) Department of Mathematics, University of Oslo, Norway

(2) Norwegian Defence Research Establishment, Kjeller, Norway

Abstract

Various methods for approximating the nonlinear advection terms in a high resolution tidal model with complex coastal boundaries have been implemented and tested. The model, driven by the dominant M_2 tidal component at the open boundaries, has been applied to a model domain with 100 meter grid resolution for the Tjeldsundet channel in northern Norway. Overtides, intensivated jets and eddy structures appear in the current fields of the full nonlinear simulations. How these flow features depend on the way the friction terms are calculated and the way the nonlinear advection terms are calculated in a zone near the coastal boundaries, are discussed. Some comparison with field measurements have also been made.

1 Introduction

In the papers by Moe et al. (2002) and Moe et al. (2003) the tides in two regions on the western and northern coast of Norway were simulated with a high resolution numerical model with horizontal grid size of 500 meters. The first version of this model was developed in the early 1990s and used for simulations of the tides in the Norwegian and Barents Seas (Gjevik (1990), and Gjevik et al. (1994)). In this model the nonlinear advection terms were neglected, but the nonlinear bottom friction was retained. Also a nonlinear representation of the horizontal eddy viscosity was adapted (Smagorinsky (1963)). For this reason we shall refer to this model as the partially linearised

numerical model (PLN-model). More recently an upgraded version of the model has been used for simulation of the tide in the outer Trondheimsfjord with a horizontal grid resolution of 50 and 100 meters (Gjevik et al. (2004)).

In narrow straights and channels with strong tidal currents it is well known that nonlinear effects can lead to significant distortion of the tides. In these cases the nonlinear advection terms must clearly be included. This is for example the case, among many others, in the Tjeldsund and Ramsund channels east of The Lofoten Islands in northern Norway. These channels connect the Vestfjord and the Ofotfjord with the Vågsfjord in Vesterålen and are important sailing lanes for coastal traffic. In an attempt to model the tidal currents in these channels, with a horizontal grid resolution of 25-50 meters, the nonlinear terms have to be included. The challenge is to find robust and accurate numerical schemes which are stable, even with complex coastlines and bottom topography, without introducing too strong smoothing or damping of the current fields.

This report discusses, in details, several methods for including the nonlinear advection terms in the original PLN-model. As an example the model is set up for Tjeldsund and Ramsund channels and the results of these simulations are used to demonstrate how the simulated tidal currents are affected by the different implementations of the nonlinear advection terms. Martinsen and Engedahl (1987)

2 Model equations

The depth-integrated shallow water equations in a Cartesian coordinate system (x,y,z) with the x- and y-axis horizontal in the level of the undisturbed surface, are given by:

$$\frac{\partial \eta}{\partial t} = -\frac{\partial U}{\partial x} - \frac{\partial V}{\partial y} \tag{1}$$

$$\frac{\partial U}{\partial t} + \frac{\partial}{\partial x}\left(\frac{U^2}{H}\right) + \frac{\partial}{\partial y}\left(\frac{UV}{H}\right) - fV = -gH\frac{\partial \eta}{\partial x} + F^x + A^x \tag{2}$$

$$\frac{\partial V}{\partial t} + \frac{\partial}{\partial x}\left(\frac{UV}{H}\right) + \frac{\partial}{\partial y}\left(\frac{V^2}{H}\right) + fU = -gH\frac{\partial \eta}{\partial y} + F^y + A^y \tag{3}$$

where (U, V) are the components of volume flux vector per unit length in the horizontal plane, η the vertical displacement of the sea surface from the mean sea level, $H = H_0 + \eta$ the total depth, H_0 the mean depth, g the acceleration of gravity, and f the Coriolis parameter.

The bottom friction terms, F^x and F^y, are given by:

$$F^x = -c_D\frac{U}{H}\frac{\sqrt{U^2+V^2}}{H} \tag{4}$$

$$F^y = -c_D\frac{V}{H}\frac{\sqrt{U^2+V^2}}{H} \tag{5}$$

where c_D is the drag coefficient of the quadratic bottom shear stress. The horizontal eddy viscosity terms, A^x and A^y, are given by:

$$A^x = \nu\nabla^2 U \tag{6}$$

$$A^y = \nu\nabla^2 V \tag{7}$$

where ν is the eddy viscosity coefficient of the horizontal shear stress.

For the eddy viscosity coefficient the Smagorinsky model (Smagorinsky (1963)) is adapted:

$$\nu = ql^2\left[\left(\frac{\partial\overline{u}}{\partial x}\right)^2 + \frac{1}{2}\left(\frac{\partial\overline{u}}{\partial y} + \frac{\partial\overline{v}}{\partial x}\right)^2 + \left(\frac{\partial\overline{v}}{\partial y}\right)^2\right]^{\frac{1}{2}} \tag{8}$$

where q is a constant, l is a length scale which is set equal to the grid size, and $(\overline{u},\overline{v})$ denote the components of the depth mean current velocity defined to the first order by:

$$\overline{u} = \frac{U}{H}, \qquad \overline{v} = \frac{V}{H}$$

With q=0.1, a grid size of 100 meters, and a current speed of the order 1 m/s, eq. (8) leads to an eddy viscosity of the order 10 m^2/s. In some simulations a constant horizontal eddy viscosity with ν ranging from 1 to 10 m^2/s is applied instead of the flow dependent viscosity in eq. (8).

By neglecting the nonlinear advection terms and the horizontal shear stress, the shallow water eqs. (1) to (3), simplify to the following:

$$\frac{\partial\eta}{\partial t} = -\frac{\partial U}{\partial x} - \frac{\partial V}{\partial y} \tag{9}$$

$$\frac{\partial U}{\partial t} - fV = -gH_0\frac{\partial\eta}{\partial x} - c_D\frac{U}{H_0}\frac{\sqrt{U^2+V^2}}{H_0} \tag{10}$$

$$\frac{\partial V}{\partial t} + fU = -gH_0\frac{\partial\eta}{\partial y} - c_D\frac{V}{H_0}\frac{\sqrt{U^2+V^2}}{H_0} \tag{11}$$

3

This is the same set of equations as implemented in the PLN-model. The equations were discretized on a C-grid (Mesinger and Arakawa (1976)) shown in figure 1, with a uniform spatial grid resolution $\triangle s$ and time step $\triangle t$:

$$\frac{\eta_{i,j}(t+\triangle t)-\eta_{i,j}(t)}{\triangle t} = -\frac{U_{i+1,j}(t)-U_{i,j}(t)}{\triangle s} - \frac{V_{i,j+1}(t)-V_{i,j}}{\triangle s} \tag{12}$$

$$\frac{U_{i,j}(t+\triangle t)-U_{i,j}(t)}{\triangle t} = f\overline{V}_{i,j}(t) - g\overline{H}_{0i,j}^i\frac{\eta_{i,j}(t+\triangle t)-\eta_{i-1,j}(t+\triangle t)}{\triangle s}$$
$$-c_D\frac{U_{i,j}(t)}{\overline{H}_{0i,j}^i}\frac{\sqrt{U_{i,j}^2(t)+\overline{V}_{i,j}^2(t)}}{\overline{H}_{0i,j}^i} \tag{13}$$

$$\frac{V_{i,j}(t+\triangle t)-V_{i,j}(t)}{\triangle t} = -f\overline{U}_{i,j}(t+\triangle t) - g\overline{H}_{0i,j}^j\frac{\eta_{i,j}(t+\triangle t)-\eta_{i,j-1}(t+\triangle t)}{\triangle s}$$
$$-c_D\frac{V_{i,j}(t)}{\overline{H}_{0i,j}^j}\frac{\sqrt{\overline{U}_{i,j}^2(t+\triangle t)+V_{i,j}^2(t)}}{\overline{H}_{0i,j}^j} \tag{14}$$

where

$$\overline{H}_{0i,j}^i = \frac{1}{2}(H_{0i,j}+H_{0i-1,j})$$
$$\overline{H}_{0i,j}^j = \frac{1}{2}(H_{0i,j}+H_{0i,j-1})$$
$$\overline{V}_{i,j} = \frac{1}{4}(V_{i,j}+V_{i-1,j}+V_{i,j+1}+V_{i-1,j+1})$$
$$\overline{U}_{i,j} = \frac{1}{4}(U_{i,j}+U_{i+1,j}+U_{i,j-1}+U_{i+1,j-1})$$

The simulations are started from rest ($\eta=U=V=0$) and are driven by specified surface elevation η at the open boundaries. Boundary values are either obtained from a model covering a larger domain or by interpolating data from a model with coarser grid. The interior solution are adjusted to the specified boundary conditions with the flow relaxation scheme (*FRS*), Martinsen and Engedahl (1987). The *FRS* softens the transition from an exterior solution to an interior solution by use of a grid zone where the two solutions dominate at each ends respectively. How a FRS zone can be implemented in tidal models is described by Moe et al. (2002) and Moe et al. (2003). Further details about the PLN-model, are given in the same papers.
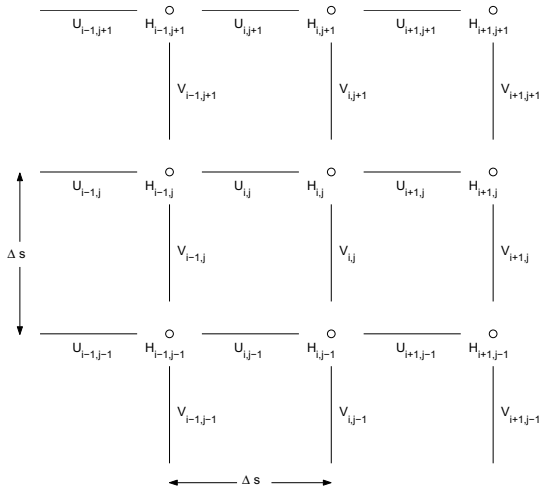
Figure 1: *C-grid stencil with a uniform spatial grid resolution $\triangle s$. The circles denotes grid points where both sea surface displacement, η, and depth, H, are specified. Lines represent grid nodes for volume fluxes U and V.*

3   Implementation of nonlinear terms

3.1   The total depth

The first and easiest modification of the PLN-model is to use the total depth, H, instead of the mean depth, H_0. This is done by adding η to H_0 after η is calculated in every grid node, and then using H in the calculations for U and V.

In order to study the effect of replacing H_0 by $H = H_0 + \eta$ in the PLN-model, eqs. (12)-(14), some numerical tests have been made, see section 5.1.

3.2   The nonlinear advection terms

Following the same discretization as used in the linear equations, the non-linear advection terms in eqs. (2) and (3) have been represented with the numerical form:

$$N_{i,j}^x = \frac{1}{\triangle s}\left(\frac{\overline{U}_{i,j}^{i\ 2}}{H_{i,j}} - \frac{\overline{U}_{i-1,j}^{i\ 2}}{H_{i-1,j}}\right) + \frac{1}{\triangle s}\left(\frac{\overline{U}_{i,j+1}^{j}\overline{V}_{i,j+1}^{i}}{\overline{H}_{i,j+1}} - \frac{\overline{U}_{i,j}^{j}\overline{V}_{i,j}^{i}}{\overline{H}_{i,j}}\right) \qquad (15)$$
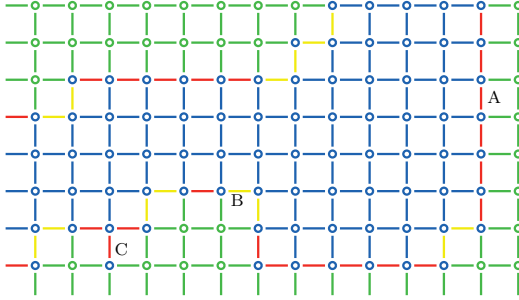
5

Figure 2: *Example of the grid mesh in the coastal zone. Red and yellow lines illustrate fluxes in the coastal zone, blue in the interior domain. Blue circles represent points for sea surface displacement. Green circles represent land points.*

$$N_{i,j}^y = \frac{1}{\triangle s} \left(\frac{\overline{U}_{i+1,j}^j \overline{V}_{i+1,j}^i}{\overline{H}_{i+1,j}} - \frac{\overline{U}_{i,j}^j \overline{V}_{i,j}^i}{\overline{H}_{i,j}} \right) + \frac{1}{\triangle s} \left(\frac{\overline{V}_{i,j}^j{}^2}{H_{i,j}} - \frac{\overline{V}_{i,j-1}^j{}^2}{H_{i,j-1}} \right) \qquad (16)$$

where

$$
\begin{aligned}
\overline{U}_{i,j}^i &= \frac{1}{2}(U_{i+1,j} + U_{i,j}) \\
\overline{U}_{i,j}^j &= \frac{1}{2}(U_{i,j} + U_{i,j-1}) \\
\overline{V}_{i,j}^i &= \frac{1}{2}(V_{i,j} + V_{i-1,j}) \\
\overline{V}_{i,j}^j &= \frac{1}{2}(V_{i,j+1} + V_{i,j}) \\
\overline{H}_{i,j} &= \frac{1}{4}(H_{i,j} + H_{i-1,j} + H_{i,j-1} + H_{i-1,j-1})
\end{aligned}
$$

For the nearest fluxes parallel to the coastline we have used a one-sided difference in the nonlinear advection terms. These fluxes are said to be located in a *coastal zone* as illustrated in figure 2.

To include the nonlinear advection terms also for the coastal zone, approximation methods must be used. The four approximation methods used for a straight coastline are illustrated by figure 3:

1. The nonlinear advection terms in the coastal zone, $f(0)$, are set to zero:

$$f_1(0) = 0$$

6
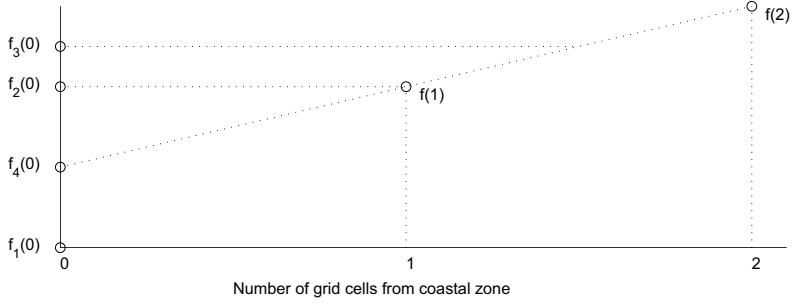
Figure 3: *Four methods to approximate a nonlinear advection term in the coastal zone, $f_n(0)$, where n=1,2,3,4 represents the method listed in the text. $f(1)$ is the value of the term one grid cell away from the coastal zone, and $f(2)$ the value two grid cells away from the coastal zone.*

2. The nonlinear advection terms in the coastal zone, $f(0)$, equal the nonlinear advection terms in the the nearest neighbouring grid cell, $f(1)$:

$$f_2(0) = f(1)$$

3. The nonlinear advection terms in the coastal zone, $f(0)$, equal the mean of the value of the terms in two grid points nearest to the coast, $f(1)$ and $f(2)$:

$$f_3(0) = \frac{1}{2}(f(1) + f(2))$$

4. The nonlinear advection terms in the coastal zone, $f(0)$, is determined by a linear extrapolation of the nonlinear advection terms from two grid cells close to the coast, $f(1)$ and $f(2)$:

$$f_4(0) = f(1) + \frac{f(2) - f(1)}{2 - 1}(0 - 1) = 2f(1) - f(2)$$

The following describe in detail how the four methods were modified in case of more complicated coastlines:

3.2.1 Special case: channel

In a narrow channel with only one or two grid cells, the nonlinear advection terms are set to zero as shown in figure 4.

7

Figure 4: *Example of a narrow channel. Red and yellow lines illustrate fluxes located in the coastal zone, blue in the interior domain. Dotted lines illustrates fluxes where t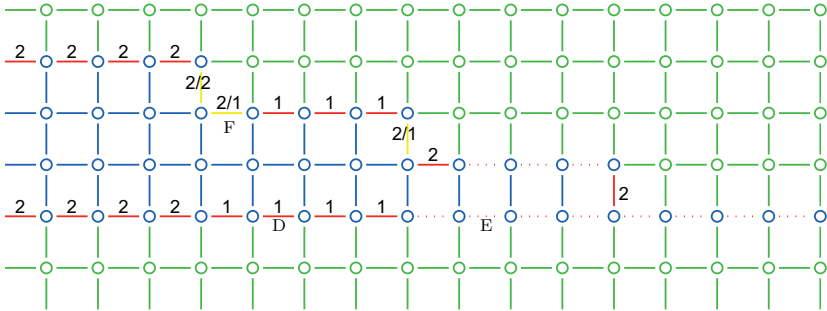he nonlinear advection terms are set to zero. Blue circles represent points for sea surface displacement. Green circles represent land points.*

In a channel with three grid cells, only the nonlinear advection terms in the middle of the channel are calculated without one-sided differences. The nonlinear advection terms in the coastal zone on each side of the channel, may be approximated using only the nonlinear advection terms in the middle of the channel. This is indicated with '1' in figure 4.

If the nonlinear advection terms in a coastal zone are approximated using two or more nonlinear advection terms in one direction, this in indicated with '2' in figure 4.

3.2.2 Special case: corners

A flux is said to be in the coastal zone *near a corner* if the parallel neighbouring fluxes in two directions is located in the water outside the coastal zone.

The nonlinear advection term for a flux in the coastal zone near a corner is approximated as the mean value of the approximation in these directions.

The flux marked with '2/2' in figure 4 and all the fluxes illustrated by yellow lines in figure 2 may use two nonlinear advection terms in each direction to approximate the nonlinear advection term in the coastal zone.

The fluxes marked with '2/1' in figure 4 may use two nonlinear advection terms in one direction and one term in another direction to approximate the terms in the coastal zone.

3.2.3 Implementation of the nonlinear advection terms

Before expressing the full equations for the nonlinear advection terms, four new parameters are defined[1]. $Z_{i,j}^x$ and $Z_{i,j}^y$ denote whether the fluxes are located in the coastal zone or in the interior domain:

$$Z_{i,j}^x = \begin{cases} 0, & \text{if the flux } U_{i,j} \text{ lies in the coastal zone or next to a land node} \\ 1, & \text{if the flux } U_{i,j} \text{ lies in the water outside the coastal zone} \end{cases}$$

$$Z_{i,j}^y = \begin{cases} 0, & \text{if the flux } V_{i,j} \text{ lies in the coastal zone or next to a land node} \\ 1, & \text{if the flux } V_{i,j} \text{ lies in the water outside the coastal zone} \end{cases}$$

and $C_{i,j}^x$ and $C_{i,j}^y$ denote the coast type for the fluxes in the coastal zone:

$$C_{i,j}^x = \begin{cases} 0, & \text{if the flux } U_{i,j} \text{ lies in the water outside the coastal zone} \\ & \text{or next to a land node} \\ 1, & \text{if the flux } U_{i,j} \text{ lies in a coastal zone, but not near a corner} \\ 0.5, & \text{if the flux } U_{i,j} \text{ lies in a coastal zone near a corner} \end{cases}$$

$$C_{i,j}^y = \begin{cases} 0, & \text{if the flux } V_{i,j} \text{ lies in the water outside the coastal zone} \\ & \text{or next to a land node} \\ 1, & \text{if the flux } V_{i,j} \text{ lies in a coastal zone, but not near a corner} \\ 0.5, & \text{if the flux } V_{i,j} \text{ lies in a coastal zone near a corner} \end{cases}$$

First the nonlinear advection terms are calculated in every grid cell, using eq. (15) and (16). Then the terms are completed by approximation in the coastal zone using one of the four methods:

Method 1:

$$\widetilde{N}_{i,j\,(1)}^x = Z_{i,j}^x N_{i,j}^x \tag{17}$$

$$\widetilde{N}_{i,j\,(1)}^y = Z_{i,j}^y N_{i,j}^y \tag{18}$$

Method 2:

$$\widetilde{N}_{i,j\,(2)}^x = Z_{i,j}^x N_{i,j}^x + C_{i,j}^x \left(N_{i-1,j}^x + N_{i+1,j}^x + N_{i,j-1}^x + N_{i,j+1}^x \right) \tag{19}$$

$$\widetilde{N}_{i,j\,(2)}^y = Z_{i,j}^y N_{i,j}^y + C_{i,j}^y \left(N_{i-1,j}^y + N_{i+1,j}^y + N_{i,j-1}^y + N_{i,j+1}^y \right) \tag{20}$$

Method 3:

$$\begin{aligned} \widetilde{N}_{i,j\,(3)}^x = \ & Z_{i,j}^x N_{i,j}^x + \tfrac{1}{2} C_{i,j}^x \big[\ (2 - Z_{i-2,j}^x)\, N_{i-1,j}^x + Z_{i-1,j}^x\, N_{i-2,j}^x \\ & + (2 - Z_{i+2,j}^x)\, N_{i+1,j}^x + Z_{i+1,j}^x\, N_{i+2,j}^x \\ & + (2 - Z_{i,j-2}^x)\, N_{i,j-1}^x + Z_{i,j-1}^x\, N_{i,j-2}^x \\ & + (2 - Z_{i,j+2}^x)\, N_{i,j+1}^x + Z_{i,j+1}^x\, N_{i,j+2}^x \ \big] \end{aligned} \tag{21}$$

---

[1]Note that Z^x is called uinl in the model code, Z^y is called vinl, C^x is called uik, and C^y is called vik.

$$\widetilde{N}^y_{i,j\,(3)} = \; Z^y_{i,j}\,N^y_{i,j} + \tfrac{1}{2}C^y_{i,j}\,[\;(2 - Z^y_{i-2,j})\,N^y_{i-1,j} + Z^y_{i-1,j}\,N^y_{i-2,j}$$
$$+(2 - Z^y_{i+2,j})\,N^y_{i+1,j} + Z^y_{i+1,j}\,N^y_{i+2,j}$$
$$+(2 - Z^y_{i,j-2})\,N^y_{i,j-1} + Z^y_{i,j-1}\,N^y_{i,j-2}$$
$$+(2 - Z^y_{i,j+2})\,N^y_{i,j+1} + Z^y_{i,j+1}\,N^y_{i,j+2}\;]$$
(22)

Method 4:

$$\widetilde{N}^x_{i,j\,(4)} = \; Z^x_{i,j}\,N^x_{i,j} + C^x_{i,j}\,[\;(1 + Z^x_{i-2,j})\,N^x_{i-1,j} - Z^x_{i-1,j}\,N^x_{i-2,j}$$
$$+(1 + Z^x_{i+2,j})\,N^x_{i+1,j} - Z^x_{i+1,j}\,N^x_{i+2,j}$$
$$+(1 + Z^x_{i,j-2})\,N^x_{i,j-1} - Z^x_{i,j-1}\,N^x_{i,j-2}$$
$$+(1 + Z^x_{i,j+2})\,N^x_{i,j+1} - Z^x_{i,j+1}\,N^x_{i,j+2}\;]$$
(23)

$$\widetilde{N}^y_{i,j\,(4)} = \; Z^y_{i,j}\,N^y_{i,j} + C^y_{i,j}\,[\;(1 + Z^y_{i-2,j})\,N^y_{i-1,j} - Z^y_{i-1,j}\,N^y_{i-2,j}$$
$$+(1 + Z^y_{i+2,j})\,N^y_{i+1,j} - Z^y_{i+1,j}\,N^y_{i+2,j}$$
$$+(1 + Z^y_{i,j-2})\,N^y_{i,j-1} - Z^y_{i,j-1}\,N^y_{i,j-2}$$
$$+(1 + Z^y_{i,j+2})\,N^y_{i,j+1} - Z^y_{i,j+1}\,N^y_{i,j+2}\;]$$
(24)

Note that for the fluxes in the water outside the coastal zone, eq. (17) to (24) become:

$$\widetilde{N}^x_{i,j\,(1)\to(4)} = \; N^x_{i,j} \qquad \widetilde{N}^y_{i,j\,(1)\to(4)} = \; N^y_{i,j}$$

since $Z^x_{i,j} = Z^y_{i,j} = 1$ and $C^x_{i,j} = C^y_{i,j} = 0$ in the water outside the coastal zone.

For our model setup the first and the last method proceed to be the most stable. Therefore section 5 only presents results from simulations with these two approximation methods.

Example A   The flux, $V_{i,j}$, marked 'A' in figure 2 is located in the coastal zone, and has water outside the coastal zone, in one direction. Therefore the nonlinear advection term is approximated in one direction. Eqs. (20), (22) and (24) become:

$$\widetilde{N}^y_{i,j\,(2)} = N^y_{i-1,j}$$
$$\widetilde{N}^y_{i,j\,(3)} = \frac{1}{2}(N^y_{i-1,j} + N^y_{i-2,j})$$
$$\widetilde{N}^y_{i,j\,(4)} = 2N^y_{i-1,j} - N^y_{i-2,j}$$

Example B The flux, $U_{i,j}$, marked 'B' in figure 2 is located in the coastal zone near a corner. Since the flux has water outside the coastal zone in two directions, the nonlinear advection term is approximated in these two directions. Eqs. (19), (21) and (23) become:

$$\widetilde{N}^x_{i,j\,(2)} = \frac{1}{2}(N^x_{i+1,j} + N^x_{i,j+1})$$

$$\widetilde{N}^x_{i,j\,(3)} = \frac{1}{4}(N^x_{i+1,j} + N^x_{i+2,j} + N^x_{i,j+1} + N^x_{i,j+2})$$

$$\widetilde{N}^x_{i,j\,(4)} = \frac{1}{2}(2N^x_{i+1,j} - N^x_{i+2,j} + 2N^x_{i,j+1} - N^x_{i,j+2})$$

Example C The flux, $V_{i,j}$, marked 'C' in figure 2 is located in the coastal zone, and has water outside the coastal zone, in one direction. The nonlinear advection term is approximated in the same way as the flux in example A: Eqs. (20), (22) and (24) become:

$$\widetilde{N}^y_{i,j\,(2)} = N^y_{i,j+1}$$

$$\widetilde{N}^y_{i,j\,(3)} = \frac{1}{2}(N^y_{i,j+1} + N^y_{i,j+2})$$

$$\widetilde{N}^y_{i,j\,(4)} = 2N^y_{i,j+1} - N^y_{i,j+2}$$

Example D The flux, $U_{i,j}$, marked 'D' in figure 4 is located in the coastal zone, and has water outside the coastal zone, in one direction. Since only one of the two nearest fluxes in that direction is located outside a coastal zone, only one grid cell is used in all the approximation methods. Eqs. (19), (21) and (23) become:

$$\widetilde{N}^x_{i,j\,(2)} = \widetilde{N}^x_{i,j\,(3)} = \widetilde{N}^x_{i,j\,(4)} = N^x_{i+1,j}$$

Example E The flux $U_{i,j}$, marked 'E' in figure 4 is located in the coastal zone, but does not have any neighbouring fluxes in water outside the coastal zone. Therefore this non-zero advection term is set to zero in all four approximation methods. Eqs. (19), (21) and (23) become:

$$\widetilde{N}^x_{i,j\,(2)} = \widetilde{N}^x_{i,j\,(3)} = \widetilde{N}^x_{i,j\,(4)} = 0$$

Example F The flux, $U_{i,j}$, marked 'F' in figure 4 is located in the coastal zone near a corner. Since the flux has water outside the coastal zone in two directions, the nonlinear advection term is approximated in these two

directions. In one of these direction, the flux two grid cells from the flux marked 'E' is located in a coastal zone. Eqs. (19), (21) and (23) become:

$$\widetilde{N}^x_{i,j\ (2)} = \frac{1}{2}(N^x_{i+1,j} + N^x_{i,j+1})$$

$$\widetilde{N}^x_{i,j\ (3)} = \frac{1}{4}(N^x_{i+1,j} + N^x_{i+2,j} + 2N^x_{i,j+1})$$

$$\widetilde{N}^x_{i,j\ (4)} = \frac{1}{2}(2N^x_{i+1,j} - N^x_{i+2,j} + N^x_{i,j+1})$$

3.3   Horizontal eddy viscosity

Following the same discretization as used in the original PLN-model, the horizontal eddy viscosities in eqs. (6) and (7) have the numerical form:

$$A^x_{i,j} = \frac{\nu}{(\triangle s)^2}(U_{i+1,j} + U_{i-1,j} + U_{i,j+1} + U_{i,j-1} - 4U_{i,j}) \qquad (25)$$

$$A^y_{i,j} = \frac{\nu}{(\triangle s)^2}(V_{i+1,j} + V_{i-1,j} + V_{i,j+1} + V_{i,j-1} - 4V_{i,j}) \qquad (26)$$

The PLN-model used in this report is without horizontal eddy viscosity. In order to make our nonlinear simulations stable, sufficient horizontal eddy viscosity has to be included. This will be discussed further in section 5.1.

Since central differencing cannot be used in the coastal zone, the horizontal eddy viscosity cannot be calculated to the same order of accuracy in the coastal zone as in the interior domain. The four suggested approximation methods used for the nonlinear advection terms, have also been evaluated for the eddy viscosity. The most stable method was to set the horizontal eddy viscosity to zero in the coastal zone. After calculating the various terms included in the horizontal eddy viscosity in the interior domain, the scheme is completed by setting these terms equal to zero in the coastal zone:

$$\widetilde{A}^x_{i,j} = Z^x_{i,j}\ A^x_{i,j}$$

$$\widetilde{A}^y_{i,j} = Z^y_{i,j}\ A^y_{i,j}$$

If the horizontal eddy viscosity is included closer than two grid cells from the FRS zone, the simulations become unstable in less than 20 hours simulated time. Therefore neither the horizontal eddy viscosity nor the nonlinear advection terms are included closer than two grid cells from the FRS zone.

3.4   Bottom shear stress

According to Crean et al. (1995) the bottom shear stress dominates the horizontal eddy viscosity near the coast. Crean et al. therefore set the

Colour	Z	C	Description
Green	-	-	land nodes where $H_0 = 0$
	0	0	fluxes next to land nodes
Blue	-	-	water nodes where $H_0 > 0$
	1	0	fluxes in the water outside the coastal zone where eqs. 15 and 16, 25 and 26 are all used directly
Red	0	1	fluxes in the coastal zone
Yellow	0	0.5	fluxes in the coastal zone near a corner
Dotted	0	0	fluxes in the coastal zone where all nonlinear terms are set to zero

Table 1: *Description of colour codes in figure 2 and 4. Z represent Z^x and Z^y, and C represent C^x and C^y*

horizontal eddy viscosity to zero, and increased the bottom shear stress near the coast. We shall adopt a similar approach.

In order to improve the stability of the nonlinear simulations we also found that the bottom shear stress coefficient has to be increased in the coastal zone. One way to increase the bottom shear stress in the coastal zone is simply to multiply the coefficient with a factor greater than unity. Another way to increase the bottom shear stress in the coastal zone, where the water depths usually are small, is to assume that the bottom friction coefficient depends on the water depth:

$$c_D = c_D^0 \left(1 + a e^{-\frac{H^2}{H_m^2}} \right) \tag{27}$$

where H is the water depth, H_m is a characteristic water depth in the coastal zone, $c_D^0 = 0.003$ is value of the coefficient in deep water ($H >> H_m$), and a is a positive scaling factor greater than unity.

In our simulations a suitable value of a was found to lie around five when the Smagorinsky formula, eq. (8) with $q = 0.3$, was used to calculate ν. When ν was constant, $\nu = 5m^2/s$, a was chosen around 15.

4   Model setup and boundary conditions

First the PLN-model with a 100 meter grid resolution was set up for a domain covering the Tjeldsund and Ramsund channels and the surrounding fjord areas as shown in figure 5. Boundary conditions in the FRS zone, ten grid cells wide, were obtained by interpolating surface elevation from the large-
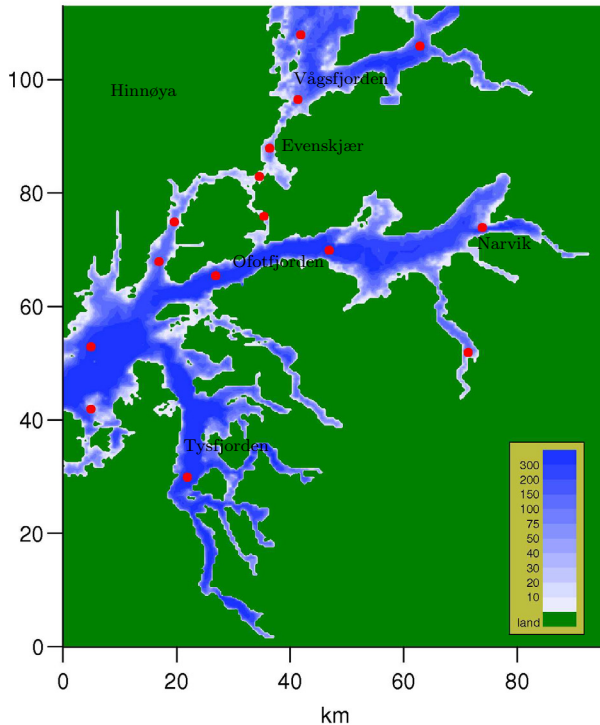
Figure 5: *The model domain covering the Tjeldsund and Ramsund channels and the surrounding fjord area. The red dots mark stations for output of time series.*

scale PLN-model for the area around the Lofoten Islands with 500 meter grid resolution (Moe et al. (2002)).

The high resolution depth matrix based on new bathymetric surveys of the model domain was not ready during this work. Therefore a test depth matrix with 100 meter grid grid resolution was constructed by interpolating from the depth matrix with 500 meter grid. Additional simulations will be conducted when a new depth matrix with 50 and 25 meter grid resolution becomes available.

Next the PLN-model with a 100 meter grid resolution was set up for a sub domain covering only the Tjeldsund and Ramsund channels as shown in figure 6. The boundary conditions in the FRS zone were obtained from the model covering the whole domain in figure 5. The results of the simulations
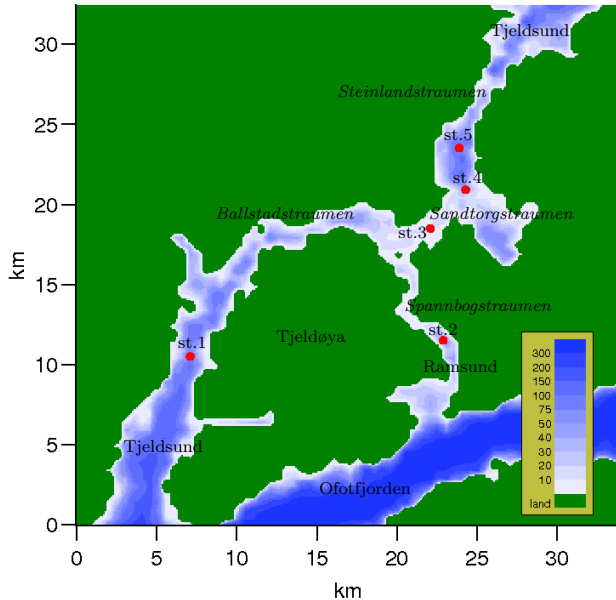
Figure 6: *The model domain for the full nonlinear model. The red dots mark the five stations for output of time series, st.1 - st.5, discussed in this report.*

for the two model domains in figure 5 and 6 were compared. Only minor differences in the current and the surface elevation were detected.

Then the full nonlinear model was set up for the domain in figure 6 with the same boundary conditions as for the PLN-model for the same domain. For the test depth matrix the mean water depth in the coastal zone, with special treatment of the nonlinear advection terms, was 5.6 meters. The maximum water depth in the coastal zone was 29.5 meters. The reference depth H_m in eq. (27) was therefore set H_m=5.6 m.

The tidal model reported here is driven only by surface amplitude and phase for the M_2 component at the open boundaries. The boundary forcing started from rest and increased in time with a ramping function, $(1 - \exp(-\sigma t))$. A value of $\sigma = 4.6 \times 10^{-5} s^{-1}$ has been used which implies full effect of boundary conditions after about 12 hours. This is similar to what was used for the PLN-model.

For every 180 seconds, surface elevation, current amplitude and phase at the output-stations were stored. Time series for the stations showed some noise due to the transient start. After 50 hours, full fields for current and

15

	ω	T	M_2	M_4	M_6	M_8
M_2	0.0805 cph	12.42 h	-	12.42 h	6.21 h	4.11 h
M_4	0.1610 cph	6.21 h	12.42 h	-	12.42 h	6.21 h
M_6	0.2415 cph	4.14 h	6.21 h	12.42 h	-	12.42 h
M_8	0.3220 cph	3.11 h	4.11 h	6.21 h	12.42 h	-

Table 2: *The frequents in cycles per hour (cph), the period of the tidal components, and the length of time series needed to separate the components by harmonic analysis.*

elevation are stored every hour. A total simulation time of 100 hours seems to be sufficient to reach an acceptable steady state.

Two stations (st3, st4) in Sandtorgstraumen are of special interest. Both stations are marked with red dots in figure 11.

4.1 Harmonic analysis

To calculate the amplitude and phase for the tidal components the program T_TIDE (Pawlowicz et al. (2002)) was used with time series for surface elevation and depth mean current from the simulations as input. T_TIDE consists of a set of programs written in Matlab and uses classical harmonic analysis for periods of about 1 year or shorter. In classical harmonic analysis, the tidal signal is simulated as the sum of a finite set of sinusoidal components with specific frequencies determined from astronomical parameters for the orbits of the Moon and the Sun.

For the simulations reported here only the dominant M_2 component is used for boundary forcing. Due to nonlinear effects the bottom friction generates the M_6 overtide with 4.1 hour period. The nonlinear advection terms and the nonlinearity in the eddy viscosity generates the M_4 and M_8 overtides with 6.2 and 3.1 hours period respectively.

The length of the time series needed to separate the component M_2 from M_4 by harmonic analysis is:

$$\frac{1}{\omega_4 - \omega_2} = 12.42 \text{ hours}$$

where ω_2 and ω_4 are the frequency in cycles per hour for M_2 and M_4 respectively.

Table 2 shows how long the time series must be, in order to separate some of the other tidal component.

	Bottom drag coefficient, c_D			
	depend on depths eq. 27		multiplied with n in coastal zone	
eddy viscosity coefficient, ν	$a = 2$	$a = 3$	$n = 4$	$n = 10$
constant $\quad\nu = 3$ m^2/s	unstable	unstable	unstable	unstable
$\nu = 4$ m^2/s	-	-	-	stable
$\nu = 5$ m^2/s	-	-	unstable	-
$\nu = 6$ m^2/s	-	-	stable	-
$\nu = 10$ m^2/s	-	unstable	-	-
$\nu = 15$ m^2/s	unstable	stable	stable	stable
Smagorinsky $\quad q = 0.1$	unstable	unstable	unstable	unstable
eq. 8 $\qquad q = 0.2$	stable	stable	unstable	stable
$q = 0.3$	-	-	stable	-
$q = 5$	-	-	stable	-
$q = 10$	stable	stable	unstable	stable

Table 3: *The stability after 100 hours of full nonlinear simulations with different choices of friction coefficients, and the nonlinear advection terms extrapolated in the coastal zone.*

5 Results

5.1 Currents and volume fluxes

Strong currents occur in Sandtorgstraumen north-east of Tjeldøya, in Steinlandsstraumen up north in Tjeldsundet and in Ballstadstraumen north of Tjeldøya. In Spannbogstraumen in Ramsundet east of Tjeldøya the currents are weaker, but since the water depths are small and the channel is narrow, the currents is considerable even here.

Among the many difficulties with nonlinear simulations, a crucial choice is to balance the amount of friction. With too little friction, the simulations become unstable, and too much friction, leads to an unrealistic strong damping of the current.

Table 3 shows which choices of ν and c_D that are suitable when the nonlinear advection terms are extrapolated in the coastal zone. Note that when the Smagorinsky formula, eq. (8), is used to calculate the eddy viscosity coefficient, the simulations are stable only for an interval of q.

This section presents results from the five full nonlinear simulations listed in table 4. For each of these simulations, the coefficients c_D and ν are chosen as small as possible for maintaining stable solutions for 100 hours simulation time. If the coefficients are chosen smaller, the simulations become unstable.

Run	Horizontal eddy viscosity coefficient	Bottom drag coefficient	nonlinear advection terms in coastal zone
1	$q = 0.3$ in eq. (8)	$a = 3$ in eq. (27)	extrapolated
2	$\nu = 6$ m^2/s, constant	x4 in coastal zone	extrapolated
3	$q = 0.3$ in eq. (8)	x4 in coastal zone	extrapolated
4	$\nu = 4$ m^2/s, constant	x4 in coastal zone	set to zero
5	$q = 0.1$ in eq. (8)		set to zero

Table 4: *The five full nonlinear simulations.*

These limits depend on the topography, the grid length, location, initial conditions, boundary conditions, and current magnitude.

Figure 11 to 18 show plots which are generated from PLN-simulations and the five full nonlinear simulations listed in table 4.

Figure 11 and 12 show the northern part of Sandtorgstraumen at the time of maximum flow northwards. Figure 11 shows results from one PLN model simulation and the three full nonlinear simulation where the nonlinear advection terms are extrapolated in the coastal zone. Figure 12 shows results from the two full nonlinear simulation where the nonlinear advection terms are set to zero in the coastal zone. Plots from the same simulations are shown for maximum flow southwards in Sandtorgstraumen, and for Steinlandsstraumen in figure 13 to 18.

The most important differences between the simulations with the PLN-model and with the full nonlinear model are the formation of intensified jets and eddies on various scales as shown in figure 11 to 18. Of course this is not unexpected, but we have been able to demonstrate how sensitive these current features are to various methods of implementing the nonlinear advection terms.

All the simulations with the full nonlinear model show an intensified jet flow and eddy structures on each side of the jet north-east of Sandtorgstraumen. The eddy structures have slightly different forms. A closer look at the plots from the full nonlinear simulations reveals currents in the opposite direction close to land in some places. This effect is probably due to the increased bottom friction applied in the coastal zone. This effect is stronger when the nonlinear advection terms are extrapolated in the coastal zone, compared to when the nonlinear advection terms are set to zero.

When the nonlinear advection terms are extrapolated in the coastal zone, and the horizontal friction coefficient, ν, is calculated using Smagorinsky formula, eq. (8), very strong currents occur close to land on the east side of the channel in the northern part of the domain as shown in figure 15b.
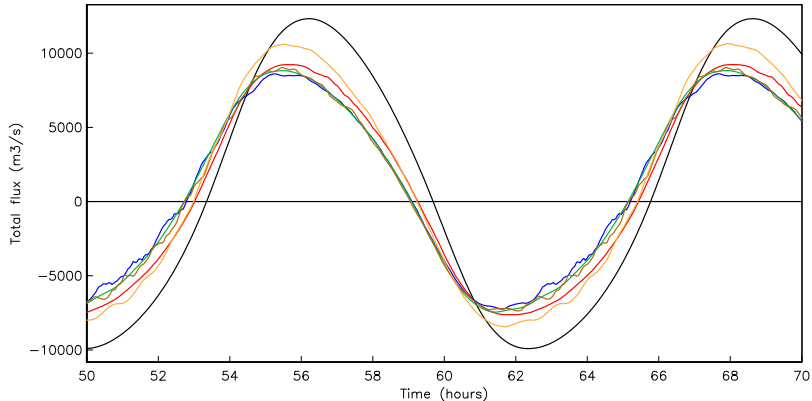
Figure 7: *Total volume flux through a cross-section in Sandtorgstraumen. The black line shows the result of the PLN-model. The other lines show results from the full nonlinear simulations listed in table 4: Red line (run 1), blue line (run 2), green line (run 3), brown line (run 4), and orange line (run 5).*

These strong currents follow the coastal zone and are reflected at the northern boundary. These currents are most likely a result of the extrapolation since the magnitude is decreased when the nonlinear advection terms are set to zero in the coastal zone.

Figure 7 displays the total volume flux through a cross-section in the middle of Sandtorgstraumen. The total volume flux at peak is up to 30% smaller in full nonlinear simulations compared to the PLN-model simulation. Since more friction is added in run 1-4 than in run 5, the total volume flux at peak in run 5 differ from the PLN-model simulation with less than 20%.

Figure 8 illustrates the impact of replacing H_0 with $H_0 + \eta$ in the PLN-model, compared with adding more friction in the PLN-model. The total volume flux at peak is decreased with up to 9% when $H_0 + \eta$ was used instead of H_0 in the PLN-model, and with up to 17 % when the friction of run 1 was added to the PLN-model.

5.2 Harmonic components

Figure 9 visualises the currents at station 4. The currents vector calculated by the PLN-model follow a typical tide ellipse, but the variability calculated by the full nonlinear model are more complicated. When T_TIDE is used
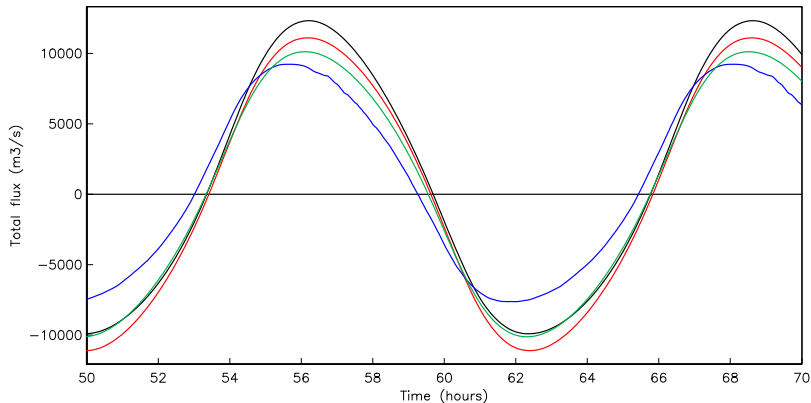
19

Figure 8: *Total volume flux through a cross-section in Sandtorgstraumen. The black line shows results of the PLN-model, and the red line shows results from the PLN-model modified with $H = H_0 + \eta$ instead of H_0. Both with constant bottom friction coefficient and no horizontal eddy viscosity.*
The blue line shows results from run 1 in table 4. The green line shows results from the PLN-model with the same friction choices as in the full nonlinear simulation.

to analyse the currents at station 4, it leads to a rather large rest current i.e. the difference between simulated currents and the currents T_TIDE recognises as tidal currents. This is clearly seen from figure 10. The rest current is stable and periodic. The period of the rest current is from 1-4 hours and the amplitude is about 40 percent of the M_2 tidal component. The magnitude of the rest current vary much from one station to another.

Table 5 and 6 show the calculated harmonic constants for the tidal components, sea level and current, for station 3 and 4. As the tables show, the amplitudes for M_4 and M_6 are, as expected, significantly larger in the full nonlinear simulation compared to the PLN-simulation.

The observed sea level amplitude and phase for the actual tidal components (Lynge, 2004) are shown in table 7. Table 7 also shows results from the PLN-model, and table 8 shows results from the full nonlinear model for the stations closest to the observed stations.

The simulated sea level amplitude for M_2 agrees well with the observed amplitude. The observed sea level amplitude for M_4 is somewhat larger than the simulated amplitudes. As expected the full nonlinear model leads to
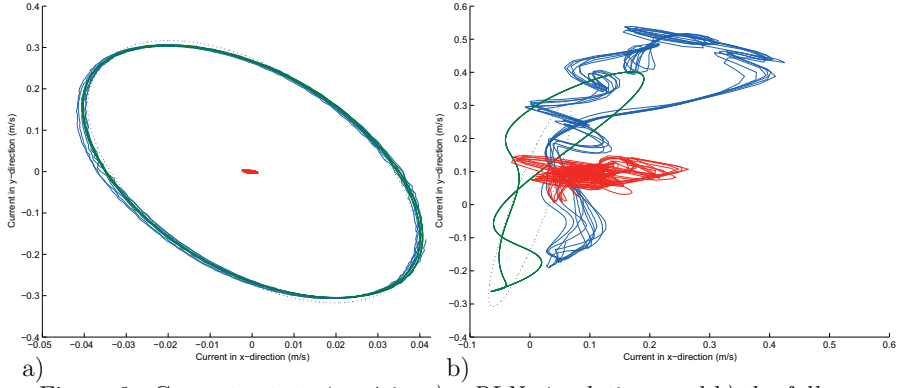
Figure 9: *Currents at station 4 in a) a PLN-simulation, and b) the full non-linear simulation with run 5. The blue curve represents the simulated current, green the current that T_Tide recognised as tide-currents, red represents the rest, and the dotted curve represents the tidal ellipse for M_2.*

larger amplitudes for M_4 than the PLN-model. The highest simulated sea level amplitude for M_4 is found when Smagorinsky formula is used instead of a constant eddy viscosity coefficient, and when the nonlinear advection terms are extrapolated in the coastal zone, instead of setting these terms to zero in the coastal zone. The sea level amplitude for M_6 is larger for the full nonlinear model than observed. This indicate that to much bottom friction is included.

st 3	PLN-model		Full nonlinear (run 5)	
const.	h_η [cm]	g_η [deg]	h_η [cm]	g_η [deg]
$\mathbf{M_2}$	83.94 ± 0.001	339.68 ± 0.05	84.94 ± 0.000	4.43 ± 0.03
$\mathbf{M_4}$			1.60 ± 0.000	205.42 ± 1.24
$\mathbf{M_6}$	0.64 ± 0.001	49.77 ± 7.32	0.85 ± 0.000	109.56 ± 2.41

st 4	PLN-model		Full nonlinear (run 5)	
const.	h_η [cm]	g_η [deg]	h_η [cm]	g_η [deg]
$\mathbf{M_2}$	74.20 ± 0.000	340.27 ± 0.04	75.11 ± 0.000	5.79 ± 0.01
$\mathbf{M_4}$			0.50 ± 0.000	347.40 ± 1.85
$\mathbf{M_6}$	0.67 ± 0.000	122.80 ± 3.82	1.04 ± 0.000	160.95 ± 0.99

Table 5: *The calculated harmonic constants for see level amplitude, h_η, and phase relative Greenwich, g_η, at station 3 and 4.*

6   Concluding remarks

Different strategies for including the nonlinear advection terms in tidal simulations are tested and results of simulations are presented. Near the coast the nonlinear advection terms can not be calculated with central differencing in the same manner as in the interior water. We have found that by extrapolating the nonlinear advection terms into a narrow zone near the coast the simulations are less stable than when the nonlinear advection terms are set to zero in this zone. Extrapolation leads however to stronger nonlinear effects in the interior domain manifested by higher amplitudes of the overtides.

To make our full nonlinear tidal simulations stable, sufficient horizontal eddy viscosity and bottom shear stress had to be included. If the nonlinear advection terms are extrapolated in the coastal zone, a constant horizontal eddy viscosity coefficient of 6 m^2/s is proved to be sufficient if the bottom shear stress is increased by a factor of 4 near the coast. When the Smagorinsky formula is used for the horizontal eddy viscosity coefficient, a value of $q = 0.3$ is sufficient if the bottom stress coefficient either is increased four times near the coast or exponentially increased with depth with a factor $a = 3$, (eq. 27). If the nonlinear advection terms are set to zero in the coastal zone, less friction need to be included. A constant horizontal eddy viscosity coefficient of 4 m^2/s is proved to be sufficient if the bottom stress coefficient is increased by a factor of 4 near the coast. And when the Smagorinsky formula is used for the horizontal eddy viscosity coefficient, a value of $q = 0.1$ is sufficient without increasing the bottom stress coefficients.

We advice to set the nonlinear advection terms to zero in a narrow zone

st 3	PLN-model				Full nonlinear (run 5)			
	A	B	θ	g_c	A	B	θ	g_c
const.	[cm/s]	[cm/s]	[deg]	[deg]	[cm/s]	[cm/s]	[deg]	[deg]
M_2	118.8	-3.9	27.1	28.4	115.3	-0.5	28.3	18.3
M_4					6.6	-0.3	21.1	16.3
M_6	6.0	-1.0	20.4	339.6	8.0	-0.6	18.2	305.2
M_8					0.7	-0.4	32.7	307.4

st 4	PLN-model				Full nonlinear (run 5)			
	A	B	θ	g_c	A	B	θ	g_c
const.	[cm/s]	[cm/s]	[deg]	[deg]	[cm/s]	[cm/s]	[deg]	[deg]
M_2	32.1	-3.4	93.5	46.7	35.3	3.0	76.5	29.0
M_4					9.0	2.5	46.9	43.1
M_6	0.13	-0.1	94.0	335.6	7.0	-0.1	27.3	34.3
M_8					3.9	0.9	24.1	23.8

Table 6: *The calculated parameters of current ellipse at station 3 and 4. Major and minor half axis denoted A and B respectively. Orientation, θ, of major axis relative east, and phase, g_c, degrees relative Greenwich, (east: $g_c = 0^o$, south: $g_c = 0^o$, etc.).*

near the coast, use Smagorinsky formula to calculate the horizontal eddy viscosity coefficient, and, if necessary, increase the bottom stress coefficient exponentially with depth (eq. 27). Note that when the Smagorinsky formula is used for the horizontal eddy viscosity coefficient, and sufficient bottom shear stress is included, the simulations are stable only for an interval of q.

For the 100 meter grid used here depth is interpolated from a depth matrix with 500 meter grid. More simulation tests will be conducted when a new depth matrix with grid resolution of 25 and 50 meter is constructed from new bathymetric data.

When a full nonlinear simulation is run with a new depth matrix we expect that the coefficients of both the bottom friction and the horizontal eddy viscosity have to be modified in order to make the simulations stable with a realistic amount of damping. The results presented in this report provide a guidance for how friction has to be adjusted.

OBSERVED	M$_2$		M$_4$		M$_6$	
	h	g [deg]	h [cm]	g [deg]	h [cm]	g [deg]
	[cm]	g [deg]	h [cm]	g [deg]	h [cm]	g [deg]
Lødingen	96.3	334.1	4.8	276.2	0.9	341.9
Ramsund	97.9	334.3	5.2	276.4	1.0	346.7
Fjelldal	87.5	340.0	2.5	285.1	0.7	4.1
Evenskjær	73.7	341.2	1.2	251.1	0.3	36.3
PLN-MODEL with $c_D = 0.03$, $\nu = 0$						
station 1	95.8	335.4	-	-	-	-
station 2	97.6	335.6	-	-	-	-
station 3	83.9	339.7	-	-	0.6	49.8
station 4	74.2	340.3	-	-	0.7	122.8
station 5	73.8	340.6	-	-	0.7	118.9

Table 7: *Observed and simulated amplitude and phase for sea level (PLN-model). Lødingen is located near station 1, Ramsund is located near station 2, Fjelldal near station 3, and Evenskjær is located between station 4 and 5.*

References

P.B. Crean, T.S. Murty, and J.A. Stronach. Mathematical Modelling of Tides and Estuarine Circulation. *Springer-Verlag, N.Y.*, 1988

B. Gjevik. Model simulations of tides and shelf waves along the shelves of the Norwegian-Greenland-Barents Seas. *Modelling Marine Systems*, Vol.I, p. 187-219. Ed. A.M. Davies, CRC Press Inc. Boca Raton, Florida, 1990.

B. Gjevik, E. Nøst, T. Straume. Model simulations of the tides in the Barents Sea. *J. Geophysical Res.*, Vol. 99, No C2, 3337–3350, 1994.

B. Gjevik, D. Hareide, B.K. Lynge, A. Ommundsen, J.H. Skailand, and H.B. Urheim. Implementation of high resolution tidal current fields in electronic navigational chart systems. *Preprint Series,* Department of Mathematics, University of Oslo. ISSN 0809-4403, 2004.

B.K. Lynge Water level observations from Tjeldsundet. January-March 2004. *Norwegian Hydrographic Service,* report nr. DAF 04-2, 2004.

E.A. Martinsen, and H. Engedahl. Implementation and testing of a lateral boundary scheme as an open boundary condition in a barotropic ocean model. *Coastal Engineering,* Vol. 11, 603–627, 1987.

F. Mesinger, and A. Arakawa. Numerical Methods Used in Atmospheric Models. *GARP Publications Series,* No.17. 64pp, 1976.

H. Moe, A. Ommundsen, and B. Gjevik. A high resolution tidal model for the area around the Lofoten Islands, Northern Norway. *Continental Shelf Research 22*, 485-504, 2002.

H. Moe, B. Gjevik, and A. Ommundsen. A high resolution tidal model for the coast of Møre and Trøndelag, Mid-Norway. *Norwegian journal of Geography,* Vol. 57, 65-82. Oslo. ISSN 0029-1951, 2003.

S. Orre, E. Åkervik, and B. Gjevik. Analysis of current and sea level observations from Trondheimsleia. *Preprint Series*, Department of Mathematics, University of Oslo. ISSN 0809-4403, 2004.

R. Pawlowicz, B. Beardsley, and S. Lentz. Classical Tidal Harmonic Analysis Icluding Error Estimated in MATLAB using T_TIDE. *Computers and Geosciences*, 28, 929-937, 2002.

J. Smagorinsky. General circulation experiments with the primitive equations. *Monthly Rewiew* 91 (1), 99-164, 1963.

SIMULATED full nonlinear	M$_2$		M$_4$		M$_6$	
	h [cm]	g [deg]	h [cm]	g [deg]	h [cm]	g [deg]
Run 1						
station 1	96.2	335.4	-	-	-	-
station 2	83.0	341.7	4.3	157.1	1.4	16.7
station 3	86.9	340.6	2.5	160.7	1.3	9.7
station 4	76.9	342.5	1.6	216.8	1.7	63.3
station 5	76.8	342.5	1.6	212.8	1.7	64.5
Run 2						
station 1	96.1	335.4	-	-	0.1	311.4
station 2	97.5	335.7	-	-	0.1	270.2
station 3	85.1	340.5	1.9	156.0	1.1	30.6
station 4	76.2	342.2	0.6	247.9	1.4	67.1
station 5	76.0	342.3	0.6	253.2	1.3	65.2
Run 3						
station 1	96.2	335.4	-	-	-	-
station 2	97.8	335.5	-	-	-	-
station 3	85.5	340.5	2.1	157.4	1.1	29.5
station 4	76.4	342.2	1.0	219.9	1.4	69.2
station 5	76.2	342.2	0.9	229.5	1.4	65.7
Run 4						
station 1	96.1	335.4	-	-	-	-
station 2	97.5	335.7	-	-	-	-
station 3	84.8	340.4	1.7	151.8	1.0	36.9
station 4	76.2	342.1	0.4	257.4	1.2	69.4
station 5	76.1	342.3	0.3	286.1	1.3	98.0
Run 5						
station 1	96.1	359.8	0.1	111.4	1.3	25.3
station 2	75.4	5.8	0.4	359.9	1.3	157.1
station 3	84.9	4.4	1.6	205.4	0.8	109.6
station 4	75.1	5.8	0.5	347.4	1.0	160.1
station 5	75.1	5.7	0.5	342.1	1.1	164.0

Table 8: *Simulated amplitude and phase for sea level from the full nonlinear model. For further explanations see legend table 7*
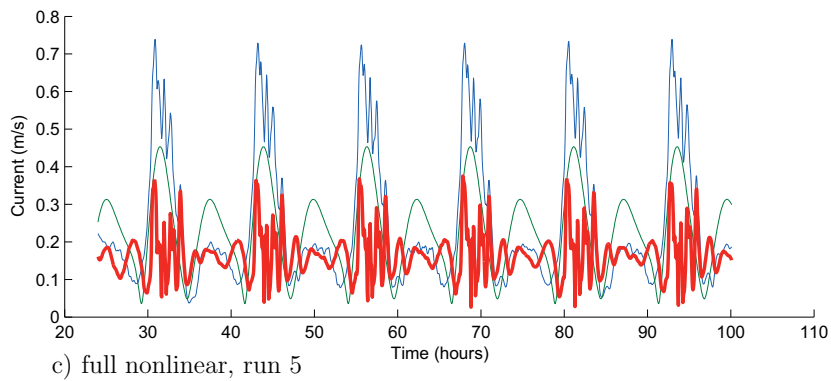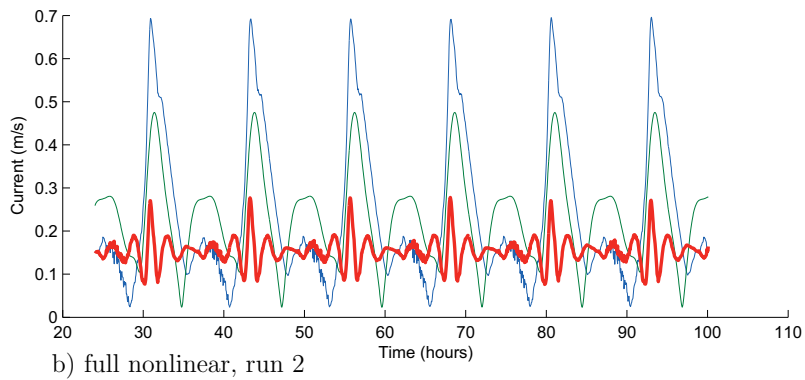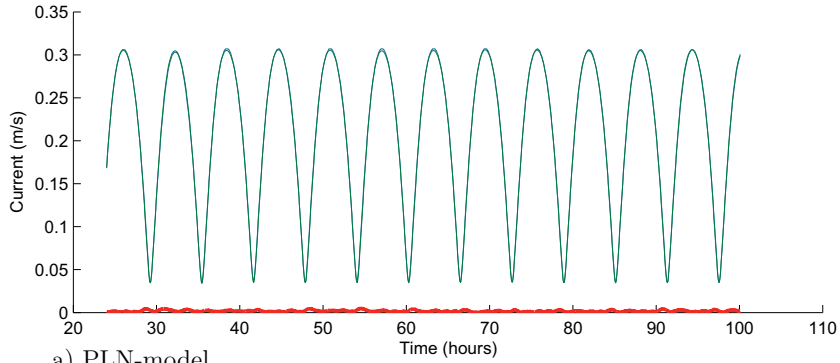
Figure 10: *Harmonic analysis of the current at station 4. The blue curve represents the simulated current, green the current that T_Tide recognized as tide-currents and red the rest current.*

a) PLN-model
   $c_D = 0.03$, $\nu = 0$

b) full nonlinear
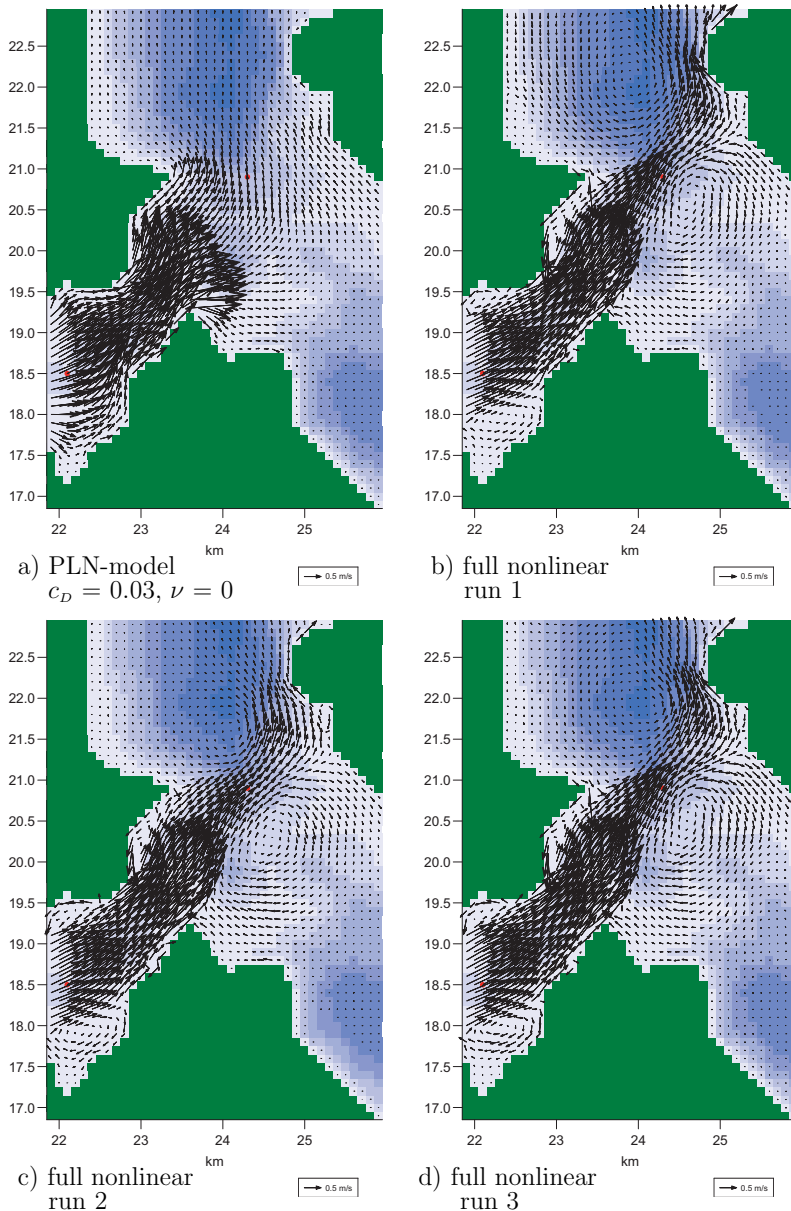   run 1

c) full nonlinear
   run 2

d) full nonlinear
   run 3

Figure 11: *Maximum flood currents northwards in Sandtorgstraumen when the nonlinear advection terms are extrapolated in the coastal zone .*
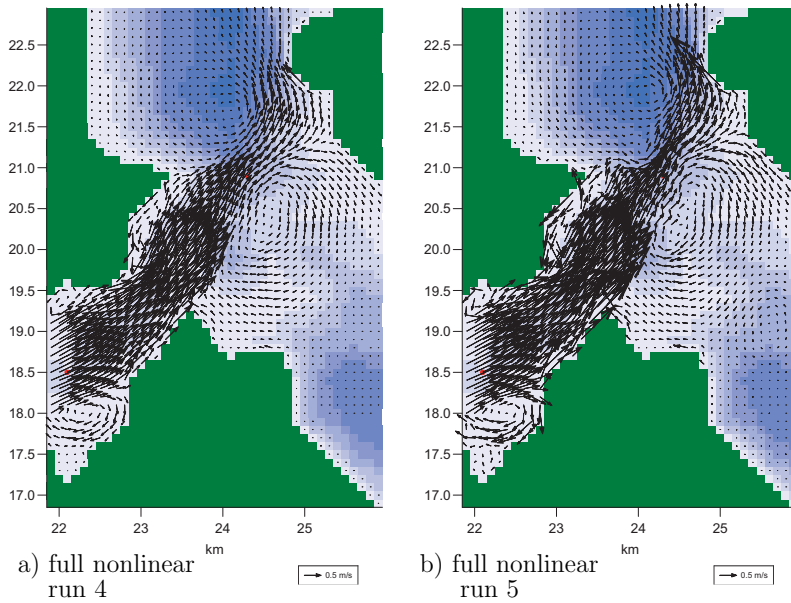
a) full nonlinear
run 4

b) full nonlinear
run 5

Figure 12: *Maximum flood currents northwards in Sandtorgstraumen when the nonlinear advection terms are set to zero in the coastal zone.*

a) PLN-model
$c_D = 0.03$, $\nu = 0$

b) full nonlinear
run 1

c) full nonlinear
run 2

d) full nonlinear
run 3

Figure 13: *Maximum ebb currents southwards in Sandtorgstraumen when the nonlinear advection terms are extrapolated in the coastal zone.*

a) full nonlinear
run 4

b) full nonlinear
run 5

Figure 14: *Maximum ebb currents southwards in Sandtorgstraumen when the nonlinear advection terms are set to zero in the coastal zone.*

31

a) PLN-model
$c_D = 0.03$, $\nu = 0$

b) full nonlinear
run 1

c) full nonlinear
run 2

d) full nonlinear
run 3

Figure 15: *Maximum flood currents northwards in Steinlandstraumen when the nonlinear advection terms are extrapolated in the coastal zone.*

32

a) full nonlinear
run 4

b) full nonlinear
run 5

Figure 16: *Maximum flood currents northwards in Steinlandstraumen when the nonlinear advection terms are set to zero in the coastal zone.*
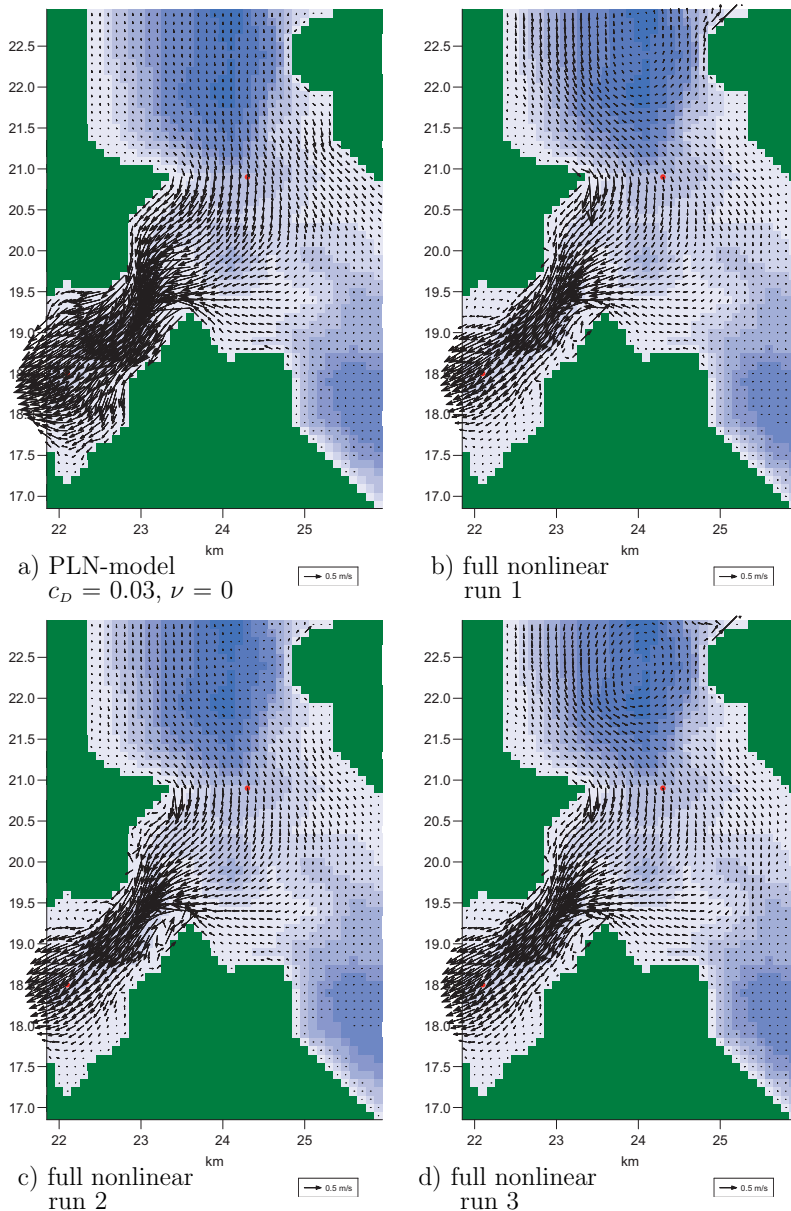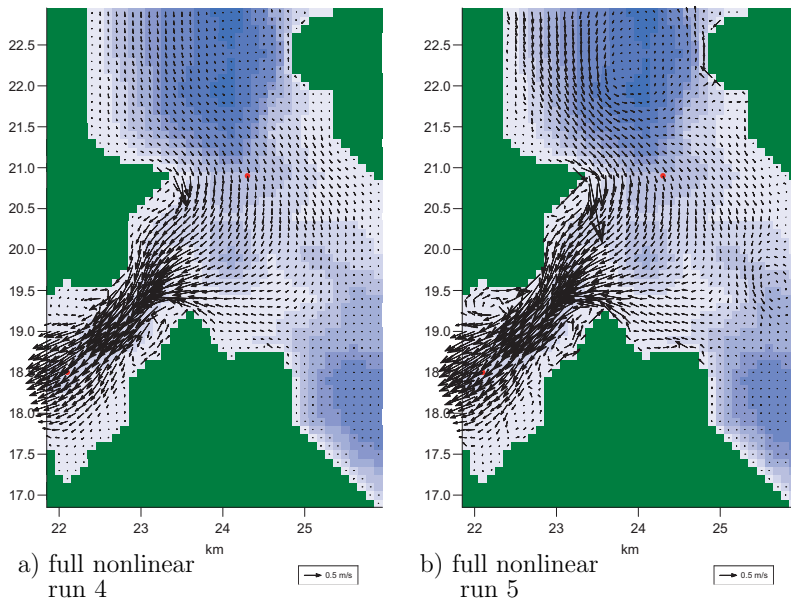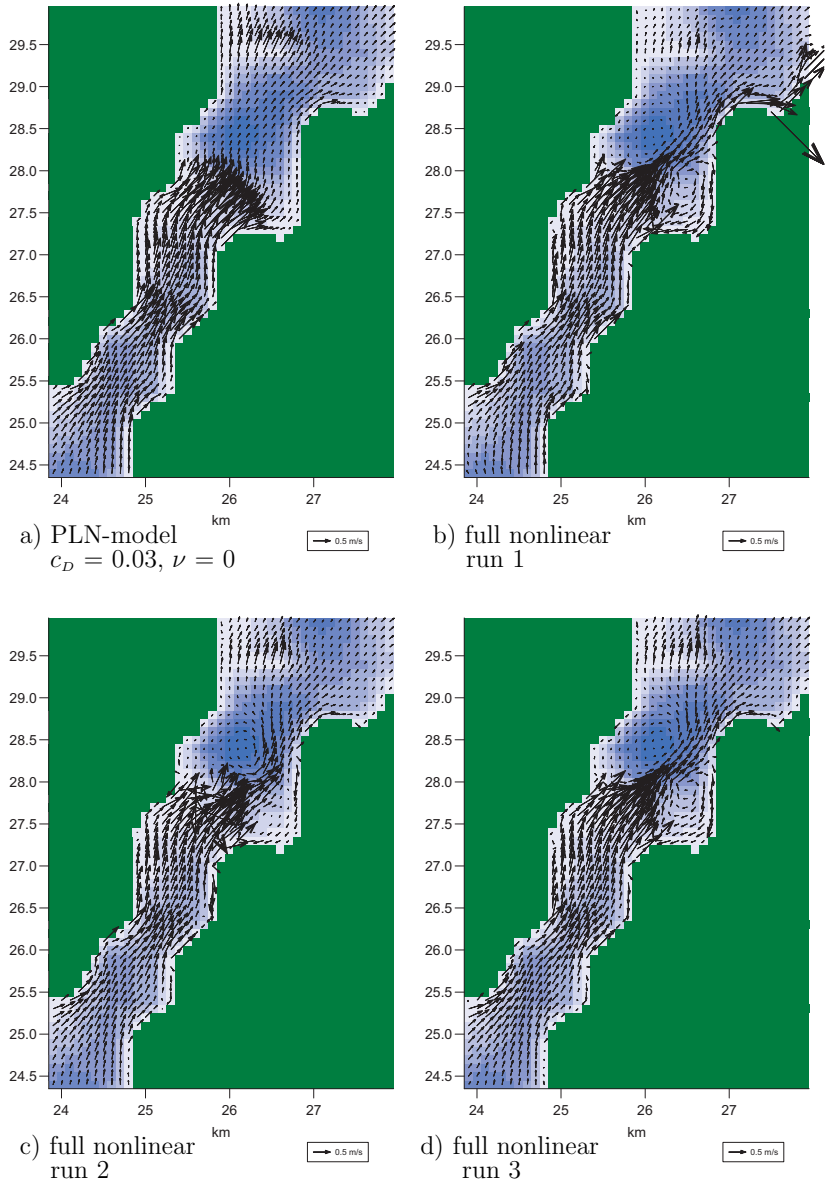
33

a) PLN-model
$c_D = 0.03$, $\nu = 0$

b) full nonlinear
run 1

c) full nonlinear
run 2

d) full nonlinear
run 3

Figure 17: *Maximum ebb currents southwards in Steinlandstraumen when the nonlinear advection terms are extrapolated in the coastal zone.*
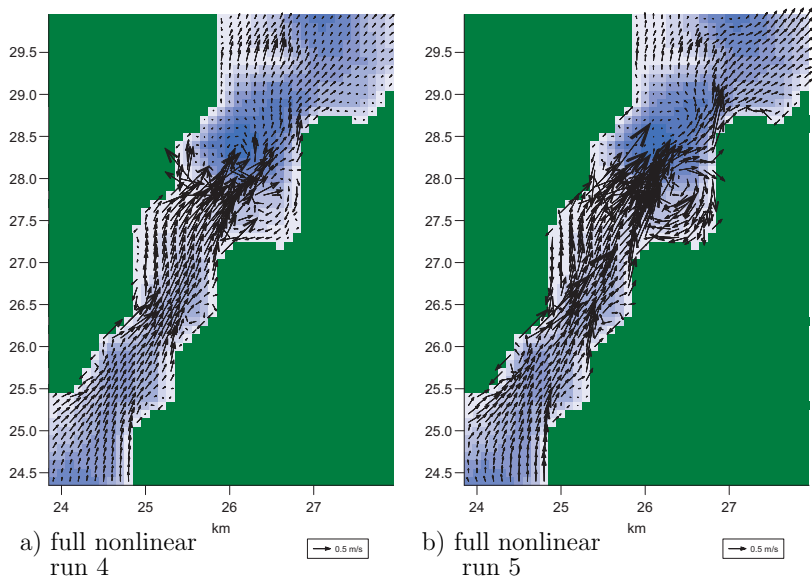
34

a) full nonlinear run 4

b) full nonlinear run 5

Figure 18: *Maximum ebb currents southwards in Steinlandstraumen when the nonlinear advection terms are set to zero in the coastal zone.*
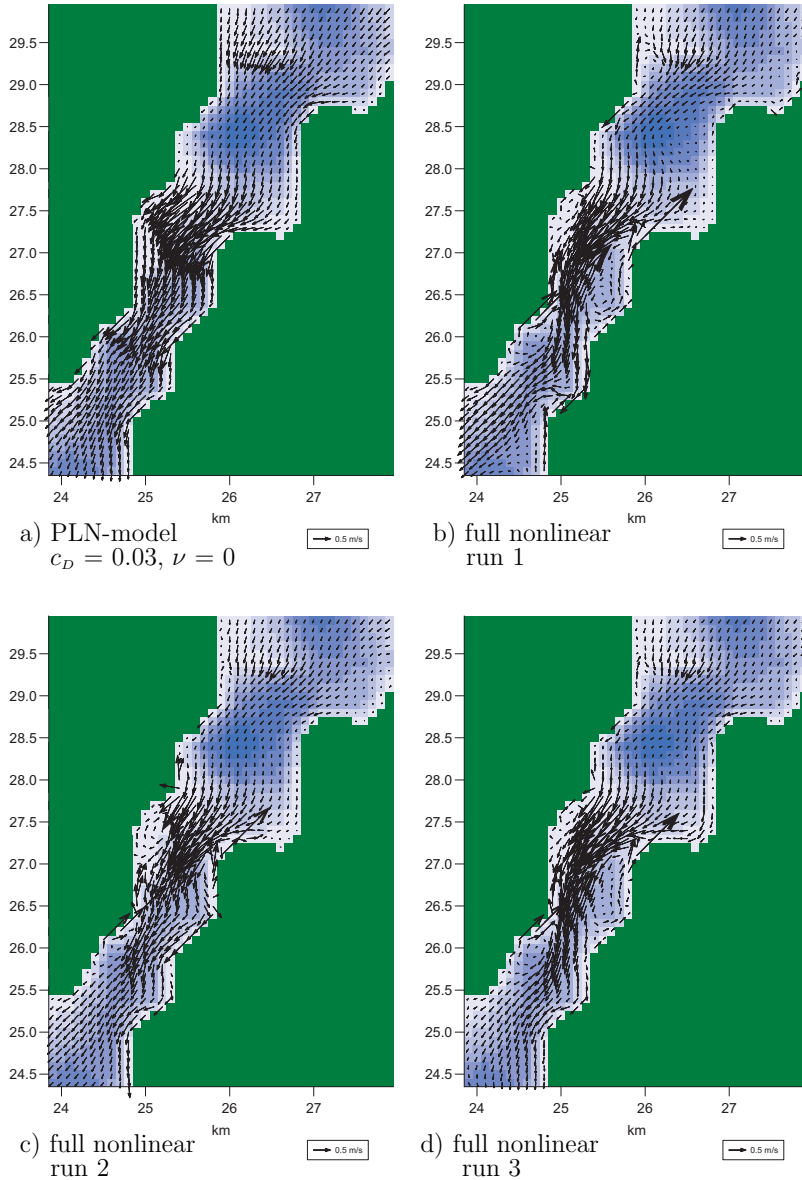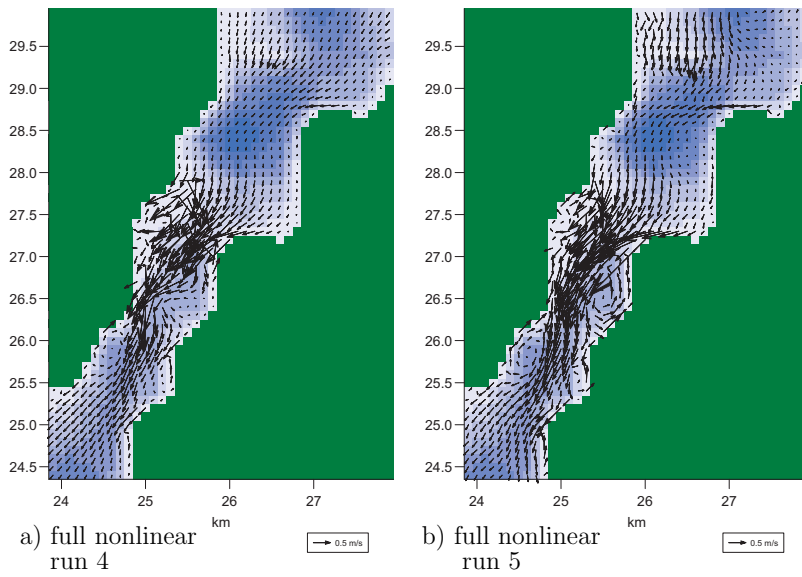
Paper 2

Modelling of tides and storm surges in the Tjeldsund channel in northern Norway

Paper 3

New current modified
Schrödinger equations

NEW CURRENT MODIFIED SCHRÖDINGER EQUATIONS

Karina B. Hjelmervik & Karsten Trulsen

Mechanics Division, Department of Mathematics, University of Oslo, Norway

Abstract

New current modified Schrödinger equations are derived suited to study waves on both potential and non–potential inhomogeneous currents. Split–step schemes of first, second, and fourth order are discussed. Different results are presented regarding the current terms and the model setup.

This paper mainly serve as background information for Hjelmervik & Trulsen (2009), but the current modified Schrödinger equations and model setup presented here are expected to have an even larger range of application possibilities.

1 Introduction

Studies of nonlinear wave–current interactions are of academic interest and important in order to reduce safety hazards in ocean currents.

Even linear interaction of waves and currents is still an active field of research. It is well known that linear refraction due to currents can provoke large waves. Waves encountering an opposing current may obtain reduced wave length and increased wave height and steepness. When waves encounter an opposing current jet, focusing can further enhance the wave intensity near the centre of the jet. Linear refraction of waves by currents is known to cause navigational problems, e.g. in the Agulhas current, river estuaries, rip currents, entrances in fjords during outgoing tides, and in tidal flows in the coastal zone, (Longuet-Higgins & Stewart, 1961; Peregrine, 1976; González, 1984; Jonsson, 1990; Lavrenov, 1998; Bottin & Thompson, 2002; Mori, Liu & Yasuda, 2002; MacIver, Simons & Thomas, 2006; MacMahan, Thornton & Reniers, 2006). When the steepness thus increases, enhanced nonlinear modulations is anticipated (Stocker & Peregrine, 1999; Lavrenov & Porubov,

2006). However, it is not well known how the enhanced effect of nonlinearity modify the wave height. Our goal is to investigate how current and nonlinearity modifies the wave heights for waves propagating on inhomogeneous stationary currents. In this paper we will derive equations and construct a numerical setup for this purpose. We will also study some results regarding the model setup, the current terms, and different current configurations.

Several different equations are used to study wave–current interactions. Our need to resolve wave phases on non–potential currents restricts us from employing several obvious candidates. White (1999) allowed a prescribed current with vorticity, and derived a wave action equation which is a phase averaged model. Ray theory (White & Fornberg, 1998) is used for tracking wave packets. Peregrine & Smith (1979) derived a nonlinear Schrödinger equation useful for caustics where ray theory breaks down. Schrödinger equations have bandwidth constraints which may be problematic. The Zakharov (1968) equation does not have bandwidth constraints, but makes it hard to include a prescribed current, and is limited to potential flows.

Here we derive a current modified cubic Schrödinger equation suited for waves on prescribed, stationary collinear currents. Some related models have already been published. Stewartson (1977) considered the effects of slowly varying depth and current, and derived a cubic Schrödinger equation limiting to potential theory. Turpin, Benmoussa & Mei (1983) considered the effects of slowly varying depth and current, and derived a cubic Schrödinger equation limiting to one horizontal dimension. Gerber (1987) used the variational principle to derive a cubic Schrödinger equation for a non–uniform medium, limiting to potential theory in one horizontal dimension. Stocker & Peregrine (1999) extended the modified nonlinear Schrödinger equation of Dysthe (1979) to include a slowly varying, periodic current and derived a current modified Schrödinger equation. As an application example of their theory, they studied the effect on a wave field from a potential surface current induced by an internal wave. Their dominant current term, UB, is of cubic order. We want to study stronger currents. Our equation will be taken up to cubic nonlinearity, and will include waves and currents in two horizontal dimensions allowing horizontal shear.

Several methods may be used to derive nonlinear Schrödinger equations for deep water waves: an averaged Lagrangian method (Yuen & Lake, 1982), a spectral method (Zakharov, 1968), and a multiple scales method (Hasimoto & Ono, 1972; Davey & Stewartson, 1974; Dysthe, 1979; Stocker & Peregrine, 1999). We have used a multiple scale expansion similar to Mei (1989).

Several numerical methods may be used to solve nonlinear Schrödinger equations. We employ a split–step method using both Fourier methods and finite difference methods (Lo & Mei, 1985; Weidman & Herbst, 1986; Stocker

& Peregrine, 1999). The Fourier methods are used on the linear terms with constant coefficients. The finite difference methods are used on the nonlinear terms and the linear terms with variable coefficients. Lo & Mei (1985) used a split–step scheme to solve the modified Schrödinger equation by Dysthe and compared their results with experiments.

2 Wave paths on prescribed currents

The linear dispersion relation for gravity waves on deep water is given by:

$$(\omega - \mathbf{k} \cdot \mathbf{U})^2 = gk \tag{1}$$

$\omega = \omega(k_x, k_y, x, y, t)$ is the angular frequency. $g = 9.81 \text{m/s}^2$ is the acceleration of gravity. $\mathbf{k} = k_x \mathbf{i} + k_y \mathbf{j}$ is the wave vector with wave number $k = \sqrt{k_x^2 + k_y^2}$. And $\mathbf{U} = U(x, y)\mathbf{i} + V(x, y)\mathbf{j}$ is the horizontal surface current which is assumed stationary and slowly varying spatially. Since $\boldsymbol{U}$ is the horizontal surface current, it does not have to be divergence free. The full current field has a vertical component which does not appear in the dispersion relation (1).

(1) may be made dimensionless using the characteristic length and time scales of the wave field in the absence of current:

$$(\omega - \mathbf{k} \cdot \mathbf{U})^2 = k \tag{2}$$

Figure 1: *The dimensionless linear dispersion relation (2) for long crested gravity waves, $\mathbf{k} = k_x \boldsymbol{i}$, on a collinear current, $\boldsymbol{U} = U(x)\boldsymbol{i}$. Here $\omega = 1$. Solutions for selected currents are marked with disks.*

There are up to four solutions of (2) for long crested waves, $\boldsymbol{k} = k_x \boldsymbol{i}$, on a collinear current, $\boldsymbol{U} = U(x)\boldsymbol{i}$, (figure 1 and 2). There exist only two
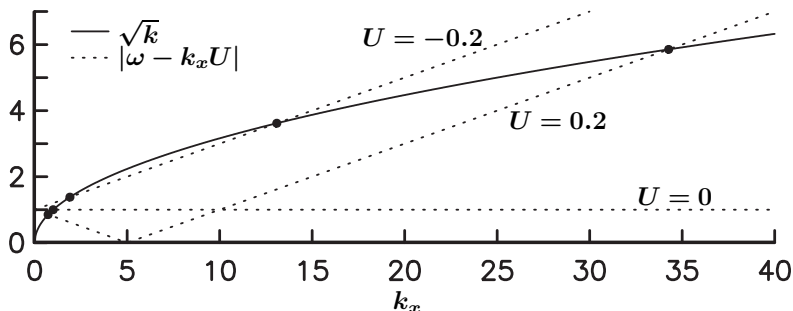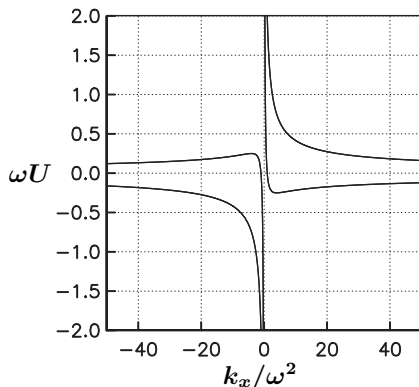
Figure 2: *The linear dispersion relation (2) for long crested gravity waves, $\mathbf{k} = k_x \boldsymbol{i}$, on a collinear current, $\boldsymbol{U} = U(x)\boldsymbol{i}$. Both coordinate axes are asymptotes for all curves. $\omega^2 = \pm k_x$ when $U = 0$. A local minimum is found in $(k_x/\omega^2, \omega U) = (4, -0.25)$.*

solutions when $U = 0$ or $|U| > \frac{1}{4\omega}$, three solutions when $|U| = \frac{1}{4\omega}$, and four solutions when $|U| < \frac{1}{4\omega}$.

Without any current the solutions are $\omega = \pm\sqrt{k}$, depending on the direction of the waves. If the waves encounter a co–current ($k_x U > 0$), the wavelength increases. If the waves encounter a counter current ($k_x U < 0$), the wavelength decreases. In both cases the phase velocity of the waves is stronger than the group velocity of the waves.

When $U = -\frac{1}{4\omega}\frac{k_x}{k}$, the group velocity of the waves has the same strength as the velocity of the counter current. If the counter current increases further in strength, there does not exist any solution of the dispersion relation because the energy of the waves cannot propagate on such strong counter currents. If the counter current decreases in strength, the wave train may split in two parts with decreasing and increasing wave number respectively. With decreasing wave number the phase velocity of the waves is stronger than the group velocity of the waves, and as the strength of the counter current approaches zero, the wave number approaches ω^2. With increasing wave number the group velocity follows the counter current. As the strength of the counter current approaches zero, the wave number approaches infinity.

On a co–current there exist solutions with high wave numbers which increase when the strength of the co–current decrease. The group velocity is larger than the phase velocity. This situation cannot be provoked by the current, but if provoked it can exist on a current. When the wave number exceeds a certain threshold, the capillary waves are more dominant than the gravity waves, see Trulsen & Mei (1993)

4

2.1 Wave path equations

The wave paths are tangential with the group velocity, $\boldsymbol{c}_g$, while the rays are tangential with the wave number vector, $\boldsymbol{k}$. Since the dispersion relation (2) is not isotropic, the wave paths and the rays do not coincide. The wave path equations may be written by:

$$\frac{\mathrm{d}\omega}{\mathrm{d}t} = \frac{\partial \omega}{\partial t} = 0 \tag{3}$$

$$\frac{\mathrm{d}\mathbf{k}}{\mathrm{d}t} = -\frac{\partial \omega}{\partial \mathbf{x}} = -k_x \left(\frac{\partial U}{\partial x} \boldsymbol{i} + \frac{\partial U}{\partial y} \boldsymbol{j} \right) \tag{4}$$

$$\frac{\mathrm{d}\mathbf{x}}{\mathrm{d}t} = \frac{\partial \omega}{\partial \mathbf{k}} = \mathbf{U} \pm \frac{1}{2\sqrt{k}} \frac{\mathbf{k}}{k} \tag{5}$$

Here the x-axis is aligned along the current so that $\boldsymbol{U} = U(x, y)\boldsymbol{i}$.

According to (3) the angular frequency, ω, is constant for each wave path. Suppose that $U = U_0$ and $\boldsymbol{k} = (k_{x0}, k_{y0})$ at $x = x_0$. The conserved frequency will then be:

$$\omega = k_{x0}U_0 \pm \left(\sqrt{k_{x0}^2 + k_{y0}^2} \right)^{1/2} \tag{6}$$

The wave paths are longitudinally reflected when $U \pm \frac{1}{2\sqrt{k}} \frac{k_x}{k} = 0$ and transversally reflected when $k_y = 0$ according to (5). Suppose that $U = U_{Rl}$ when the wave paths are longitudinally reflected, and $U = U_{Rt}$ when the wave paths are transversally reflected. If $k_{y0} = 0$, U_{Rl} and U_{Rt} are given by:

$$U_{Rl} = -\frac{1}{4\omega} \tag{7}$$

$$U_{Rt} = U_0 \tag{8}$$

The stopping velocity in (7) is in agreement with Peregrine (1976), White & Fornberg (1998), and others.

Following Mei (1989) it can be shown that B satisfies the following conservation law:

$$\frac{\partial}{\partial t} \left(\frac{B^2}{\sigma} \right) + \nabla_h \cdot \left(\mathbf{c_g} \frac{B^2}{\sigma} \right) = 0 \tag{9}$$

B is the amplitude of the waves. σ and $\mathbf{c}_g$ are given by:

$$\sigma = \omega - \mathbf{U} \cdot \mathbf{k}$$

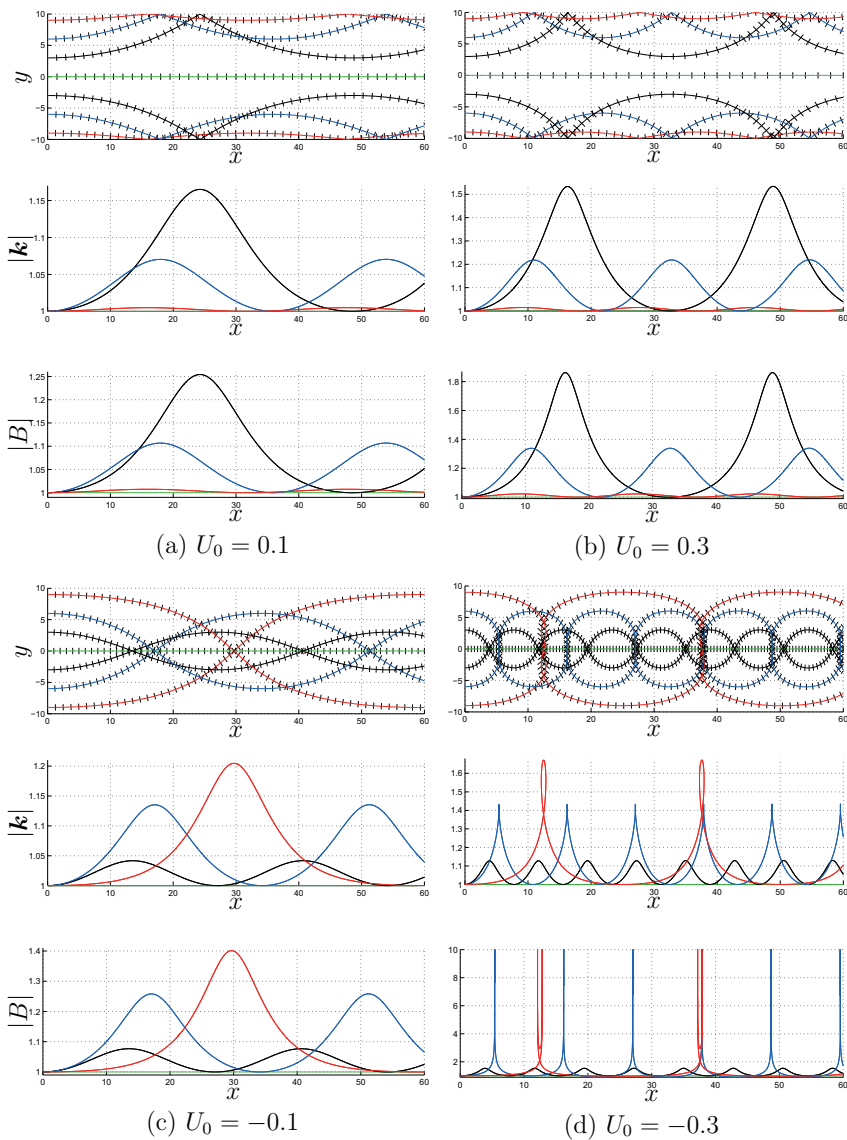$$\mathbf{c}_g = \mathbf{U} \pm \frac{1}{2\sqrt{k}} \frac{\mathbf{k}}{k}$$

5

Figure 3: *Wave paths with corresponding wave number, $|\boldsymbol{k}|$, and amplitude, $|B|$, as a function of x according to (3)–(5) and (9). The short lines across the wave paths are normal to the wave vector $\boldsymbol{k}$. Here $\omega = 1$.*

6

(9) may also be written on the same form as the wave path equations, in order to calculate the amplitude while tracing a path:

$$\frac{\mathrm{d}}{\mathrm{d}t}\left(\frac{B^2}{\sigma}\right) = \frac{\partial}{\partial t}\left(\frac{B^2}{\sigma}\right) + \mathbf{c}_g \cdot \nabla_h\left(\mathbf{c_g}\frac{B^2}{\sigma}\right) = -\left(\frac{B^2}{\sigma}\right)\nabla\cdot\mathbf{c}_g \quad (10)$$

2.1.1 An example

Suppose that the waves ride a collinear current jet where $\mathbf{U} = U(y)\mathbf{i}$:

$$U(y) = U_0\cos^2\left(\frac{\pi y}{Y}\right) \quad (11)$$

The rays diverge on co–currents (figure 3a–b) and converge on counter currents (figure 3c–d). The rays are transversally reflected at the same velocity as the initial velocity in agreement with (8). Since the dispersion relation (2) is not isotropic, the wave vector, $\boldsymbol{k}$, is not tangential with the wave paths except when the wave vector is parallel to the current, $\boldsymbol{U}$.

On co–current jets the amplitude and wave number increase towards the channel walls and decrease towards the centre of the jet. On counter current jets the amplitude and wave number increase towards the centre of the jet. When the counter current is stronger than the stopping velocity, (7), the rays are reflected longitudinally (figure 3d).

2.2 Exact dispersion for constant current

Suppose that only the positive root is applied in (2):

$$\omega = k_x U + k_y V + \left(k_x^2 + k_y^2\right)^{\frac{1}{4}} \quad (12)$$

Let $\omega = 1 + \triangle\omega$ and $\boldsymbol{k} = (k_x, k_y) = (1 + \triangle k_x, \triangle k_y)$ where $\triangle\omega$ is the modulation frequency and $(\triangle k_x, \triangle k_y)$ is the modulation wave vector:

$$1 + \triangle\omega = (1 + \triangle k_x)U + \triangle k_y V + \left(1 + 2\triangle k_x + (\triangle k_x)^2 + (\triangle k_y)^2\right)^{\frac{1}{4}} \quad (13)$$

Taylor expansion of the last term gives:

$$\triangle\omega - U - \triangle k_x U - \triangle k_y V - \frac{1}{2}\triangle k_x + \frac{1}{8}(\triangle k_x)^2 - \frac{1}{4}(\triangle k_y)^2$$
$$-\frac{1}{16}(\triangle k_x)^3 + \frac{3}{8}\triangle k_x(\triangle k_y)^2 = O\left((\triangle k)^4\right) \quad (14)$$

Following the method of Yuen & Lake (1982) and Trulsen *et al.* (2000), (14) may then be transformed using the following direct correspondences:

$$\triangle\omega \to i\frac{\partial}{\partial t}, \qquad \triangle k_x \to -i\frac{\partial}{\partial x}, \qquad \triangle k_y \to -i\frac{\partial}{\partial y} \tag{15}$$

For a linear, homogeneous wave system of uniform properties these correspondences can be made rigorous. When including inhomogeneous currents, the two last relationships in (15) are not accurate unless the $\nabla\boldsymbol{U}$–terms can be neglected (Stocker & Peregrine, 1999).

Suppose that the current is slowly varying so that the waves do not feel the changes locally. Then the relations in (15) used on (14) give:

$$i\frac{\partial}{\partial t} - U + iU\frac{\partial}{\partial x} + iV\frac{\partial}{\partial y} + \frac{i}{2}\frac{\partial}{\partial x} - \frac{1}{8}\frac{\partial^2}{\partial x^2} + \frac{1}{4}\frac{\partial^2}{\partial y^2}$$
$$-\frac{i}{16}\frac{\partial^3}{\partial x^3} + \frac{3i}{8}\frac{\partial^3}{\partial x\partial y^2} = O\left((\triangle k)^4\right) \tag{16}$$

If multiplied with $-iB$, the linear terms in a time evolution of a current modified Scrödinger equation appear:

$$\frac{\partial B}{\partial t} + \frac{1}{2}\frac{\partial B}{\partial x} + iUB + U\frac{\partial B}{\partial x} + V\frac{\partial B}{\partial y} + \frac{i}{8}\frac{\partial^2 B}{\partial x^2} - \frac{i}{4}\frac{\partial^2 B}{\partial y^2}$$
$$-\frac{1}{16}\frac{\partial^3 B}{\partial x^3} + \frac{3}{8}\frac{\partial^3 B}{\partial x\partial y^2} = O\left((\triangle k)^4\right) \tag{17}$$

In the next section, current modified nonlinear Schrödinger equations will be derived using multiple scales. These equations will allow inhomogeneous currents.

3 Evolution of current modified nonlinear Schrödinger equations

Assume that the total velocity field, $\boldsymbol{v}_{tot} = \boldsymbol{v} + \boldsymbol{V}$, is a superposition of the velocity of a wave field, $\boldsymbol{v} = (u, v, w)$, and a prescribed stationary current field, $\boldsymbol{V} = (U, V, W)$, in a Cartesian coordinate system, (x, y, z). The x–axis is aligned with the principal propagation direction of the waves. The z–axis is vertical with unit vector $\boldsymbol{k}$ pointing upwards. $z = 0$ corresponds to the undisturbed free water surface. The water is assumed inviscid, incompressible, and deep with respect to the characteristic wavelength. The current field is assumed unaffected by waves. η and ζ are the surface displacements associated with the wave field and the current field respectively.

	Potential current (sec. 3.1)	Vorticity allowed (sec. 3.2)	Stewartson (1977)	Stocker & Peregrine (1999)	Hjelmervik & Trulsen (2009)
ak_c	ϵ	ϵ	0	ϵ	ϵ
$(U,V)k_c/\omega_c$	ϵ	ϵ	1	ϵ^2	ϵ
Wk_c/ω_c	ϵ^5	ϵ^4	ϵ^2	ϵ^2	ϵ^2
Ak_c	ϵ^2	ϵ^2	0	ϵ^2	ϵ^2
$1/k_cX$	ϵ^2	ϵ	ϵ	ϵ	ϵ
$1/k_cY$	ϵ^2	1	ϵ	ϵ	ϵ
$1/\omega_cT$	0	0	ϵ^2	ϵ	0
Nonlinear	yes	yes	no	yes	yes
Horizontal dimensions	2	2	2	2	2
Potential theory	yes	no	yes	yes	no

Table 1: *Current modified Schrödinger equations. k_c and ω_c are the characteristic wave number and frequency for the undisturbed wave field, $\omega_c^2 = gk_c$. a and A are the amplitudes associated with the wave field and the surface current field respectively. (U, V, W) is the characteristic current with a characteristic length scale (X, Y, Z) and time scale T.*

The Euler equation for the combined wave and current field can be written as:

$$\frac{\partial \boldsymbol{v}}{\partial t} + \boldsymbol{v}_{tot} \cdot \boldsymbol{\nabla} \boldsymbol{v}_{tot} = -\frac{1}{\rho}\boldsymbol{\nabla} p_{tot} - g\boldsymbol{k} \tag{18}$$

The total pressure, $p_{tot} = p + P + p_s$, is a combination of the dynamic pressure due to the wave field, p, the dynamic pressure due to the current field, P, and the static pressure, $p_s = p_a - \rho gz$, where p_a is the atmospheric pressure, ρ is the density, and g is the acceleration of gravity.

The vorticity of the waves, $\boldsymbol{\gamma} = \boldsymbol{\nabla} \times \boldsymbol{v}$, obeys the equation:

$$\frac{\partial \boldsymbol{\gamma}}{\partial t} + \boldsymbol{v}_{tot} \cdot \boldsymbol{\nabla}\boldsymbol{\gamma} - \boldsymbol{\gamma} \cdot \boldsymbol{\nabla}\boldsymbol{v}_{tot} = -\boldsymbol{v} \cdot \boldsymbol{\nabla}\boldsymbol{\Gamma} + \boldsymbol{\Gamma} \cdot \boldsymbol{\nabla}\boldsymbol{v} \tag{19}$$

If the vorticity of the current, $\boldsymbol{\Gamma} = \boldsymbol{\nabla} \times \boldsymbol{V}$, equals zero, (19) is homogeneous with respect to $\boldsymbol{\gamma}$, and if the wave field starts out irrotational, it will remain irrotational. For waves riding a current field with vorticity, vorticity will develop in the wave field as well.

Traditional Schrödinger equations are built on potential theory (Davey & Stewartson, 1974; Stewartson, 1977; Dysthe, 1979; Dysthe & Das, 1981;

Gerber, 1987; Stocker & Peregrine, 1999; Trulsen *et al.*, 2000). Here we will derive two current modified nonlinear Schrödinger equations. The first is built on potential theory (sec. 3.1), and the second allows horizontal shear and includes all the terms from the first (sec. 3.2). In table 1 the characteristic sizes of these derivations are compared to some of the derivations found in literature.

Let a, k_c and ω_c be the characteristic amplitude, wavenumber and angular frequency of the surface waves. We employ the steepness of the waves as a small ordering parameter in the following, $\epsilon = ak_c \ll 1$, thus $k_c\eta = O(\epsilon)$ and $\boldsymbol{v}\frac{k_c}{\omega_c} = O(\epsilon)$. The horizontal current velocities are assumed just small enough to avoid collinear reflection of the waves, $(U,V)\frac{k_c}{\omega_c} = O(\epsilon)$. The vertical surface current velocity is assumed negligible, $W\frac{k_c}{\omega_c} = O(\epsilon^5)$ when potential theory is used, and $W\frac{k_c}{\omega_c} = O(\epsilon^4)$ when vorticity is allowed. It follows from the Bernoulli equation that the surface displacement induced by the current is small, $Ak_c = O(\epsilon^2)$.

3.1   Potential current field

If the current field is a potential field, $\boldsymbol{V} = \boldsymbol{\nabla}\Phi$, the velocity of the wave field can be represented by a potential, $\boldsymbol{v} = \boldsymbol{\nabla}\phi$, according to (19).

The continuity equation for the wave field, may be written as:

$$\boldsymbol{\nabla}^2\phi = 0 \tag{20}$$

The waves are assumed on deep water, that is $\nabla\phi \to 0$ as $z \to -\infty$. The surface equations for the combined field at the free surface $z = \eta + \zeta$, can be written as:

$$\frac{\partial\eta}{\partial t} + \boldsymbol{\nabla}(\phi+\Phi)\cdot\boldsymbol{\nabla}(\eta+\zeta) = \frac{\partial}{\partial z}(\phi+\Phi) \tag{21}$$

$$\frac{\partial\phi}{\partial t} + \frac{1}{2}\left(\boldsymbol{\nabla}(\phi+\Phi)\right)^2 + g(\eta+\zeta) = 0 \tag{22}$$

Taylor expansions around $z = 0$ gives (21–22) on the form:

$$\frac{\partial\eta}{\partial t} + \nabla\phi\cdot\nabla(\eta+\zeta) + \nabla\Phi\cdot\nabla\eta + \zeta\nabla\frac{\partial}{\partial z}(\phi+\Phi)\cdot\nabla\eta + \zeta\nabla\frac{\partial\phi}{\partial z}\cdot\nabla\zeta$$

$$+\eta\nabla\frac{\partial}{\partial z}(\phi+\Phi)\cdot\nabla(\eta+\zeta) + \frac{1}{2}\eta(\eta+2\zeta)\nabla\frac{\partial}{\partial z}(\phi+\Phi)\cdot\nabla(\eta+\zeta)$$

$$+\frac{1}{2}\zeta^2\nabla\frac{\partial}{\partial z}(\phi+\Phi)\cdot\nabla\eta + \frac{1}{2}\zeta^2\nabla\frac{\partial\phi}{\partial z}\cdot\nabla\zeta + \frac{1}{6}\eta^3\nabla\frac{\partial^2\phi}{\partial z}\cdot\nabla\eta$$

$$= \frac{\partial\phi}{\partial z} + \eta\frac{\partial^2}{\partial z^2}(\phi+\Phi) + \zeta\frac{\partial^2\phi}{\partial z^2} + \frac{1}{2}\eta(\eta+2\zeta)\frac{\partial^3}{\partial z^3}(\phi+\Phi) + \frac{1}{2}\zeta^2\frac{\partial^3\phi}{\partial z^3}$$

$$+\frac{1}{6}\eta^3\frac{\partial^4\phi}{\partial z^4}+\cdots \tag{23}$$

$$\frac{\partial\phi}{\partial t}+(\eta+\zeta)\frac{\partial^2\phi}{\partial t\partial z}+\frac{1}{2}(\eta+\zeta)^2\frac{\partial^3\phi}{\partial t\partial z^2}+\frac{1}{6}(\eta+\zeta)^3\frac{\partial^4\phi}{\partial t\partial z^3}$$

$$+\frac{1}{2}\nabla\phi\cdot\nabla(\phi+2\Phi)+\eta\nabla(\phi+\Phi)\cdot\nabla\frac{\partial}{\partial z}(\phi+\Phi)+\zeta\nabla(\phi+\Phi)\cdot\nabla\frac{\partial\phi}{\partial z}$$

$$+\zeta\nabla\phi\cdot\nabla\frac{\partial\Phi}{\partial z}+\frac{1}{2}\eta^2\left(\nabla\frac{\partial\phi}{\partial z}\right)^2+\frac{1}{2}\eta^2\nabla\phi\cdot\nabla\frac{\partial^2\phi}{\partial z^2}+g\eta+\cdots=0 \tag{24}$$

Let the horizontal length scales, L, of the current be longer than a characteristic wavelength so that $1/(k_cL)=O(\epsilon^2)$. In accordance with the scaling assumptions, all equations, variables, and sizes in the following are made dimensionless using the characteristic length and time scales of the wave field, so that $k_c\boldsymbol{x}\to\boldsymbol{x}$, $\epsilon k_c\boldsymbol{x}\to\bar{\boldsymbol{x}}$, $\omega_ct\to t$, $k_c\eta\to\epsilon\eta$, $k_c\zeta\to\epsilon^2\zeta$, $\frac{1}{\omega_c}\phi\to\epsilon\phi$, $\frac{k_c}{\omega_c}(U,V)\to\epsilon(U,V)$, and $\frac{k_c}{\omega_c}W\to\epsilon^5W$,

The wave field is represented by perturbation series for the surface displacement, η, and the velocity potential, ϕ:

$$\begin{aligned}\eta &= \epsilon\bar{\eta}+\tfrac{1}{2}\Big(B_1\mathrm{e}^{\mathrm{i}(x-t)}+\epsilon B_2\mathrm{e}^{2\mathrm{i}(x-t)}+\epsilon^2B_3\mathrm{e}^{3\mathrm{i}(x-t)}+\cdots+\mathrm{c.c.}\Big)\\ \phi &= \epsilon\bar{\phi}+\tfrac{1}{2}\Big(A_1'\mathrm{e}^{\mathrm{i}(x-t)}+\epsilon A_2'\mathrm{e}^{2\mathrm{i}(x-t)}+\epsilon^2A_3'\mathrm{e}^{3\mathrm{i}(x-t)}+\cdots+\mathrm{c.c.}\Big)\end{aligned} \tag{25}$$

$\bar{\eta}=\bar{\eta}(\bar{x},\bar{y},\bar{t})$ and $\bar{\phi}=\bar{\phi}(\bar{x},\bar{y},z,\bar{t})$ are the mean surface displacement and mean induced velocity potential respectively. $B_n=B_n(\bar{x},\bar{y},\bar{t})$ and $A_n'=A_n'(\bar{x},\bar{y},z,\bar{t})$ are the n'th harmonics of the surface displacement and the induced current potential respectively. The characteristic wavenumber is fixed appropriate for waves undisturbed by current, therefore the entire effect of refraction is represented by modulations of B_1.

Both the mean functions and the harmonics, are perturbed:

$$\begin{aligned}\bar{\eta} &= \bar{\eta}_1+\epsilon\bar{\eta}_2+\cdots, & B_n &= B_{n0}+\epsilon B_{n1}+\epsilon^2B_{n2}+\cdots\\ \bar{\phi} &= \bar{\phi}_1+\epsilon\bar{\phi}_2+\cdots, & A_n' &= A_{n0}'+\epsilon A_{n1}'+\epsilon^2A_{n2}'+\cdots\end{aligned} \tag{26}$$

3.1.1   Vertical dependence

The n'th harmonic terms of the scaled continuity equation, (20) is given by:

$$\frac{\partial^2A_n'}{\partial z^2}-n^2A_n'+2\epsilon\mathrm{i}n\frac{\partial^2A_n'}{\partial\bar{x}}+\epsilon^2\left(\frac{\partial^2A_n'}{\partial\bar{x}^2}+\frac{\partial^2A_n'}{\partial\bar{y}^2}\right)\;=\;0 \tag{27}$$

where $\frac{\partial A_n'}{\partial z}\to0$ as $z\to-\infty$.

First order To first order the continuity equation for A'_n (27) is:

$$\frac{\partial^2 A'_{n0}}{\partial z^2} - n^2 A'_{n0} = 0 \tag{28}$$

which has the solution:

$$A'_{n0} = A_{n0}(\bar{x}, \bar{y}, \bar{t})\mathrm{e}^{nz} \tag{29}$$

since $\frac{\partial A'_{n0}}{\partial z} \to 0$ as $z \to -\infty$.

Second order To second order the continuity equation for A'_n (27) is:

$$\frac{\partial^2 A'_{n1}}{\partial z^2} - n^2 A'_{n1} + 2\mathrm{i}n\frac{\partial A'_{n0}}{\partial \bar{x}} = 0 \tag{30}$$

where $\frac{\partial A'_{n1}}{\partial z} \to 0$ as $z \to -\infty$.

Using the result from first order (29), gives:

$$\frac{\partial^2 A'_{n1}}{\partial z^2} - n^2 A'_{n1} + 2\mathrm{i}n\frac{\partial A_{n0}}{\partial \bar{x}}\mathrm{e}^{nz} = 0 \tag{31}$$

which has the solution:

$$A'_{n1} = A_{n1}(\bar{x}, \bar{y}, \bar{t})\mathrm{e}^{nz} - \mathrm{i}\frac{\partial A_{n0}}{\partial \bar{x}}z\mathrm{e}^{nz} \tag{32}$$

Third order To third order the continuity equation for A'_n (27) is:

$$\frac{\partial^2 A'_{n2}}{\partial z^2} - n^2 A'_{n2} + 2\mathrm{i}n\frac{\partial A'_{n1}}{\partial \bar{x}} + \frac{\partial^2 A'_{n0}}{\partial \bar{x}^2} + \frac{\partial^2 A'_{n0}}{\partial \bar{y}^2} = 0 \tag{33}$$

where $\frac{\partial A'_{n2}}{\partial z} \to 0$ as $z \to -\infty$.

Using the results from first and second order (29, 32) gives:

$$\frac{\partial^2 A'_{n2}}{\partial z^2} - n^2 A'_{n2} + 2\mathrm{i}n\frac{\partial A_{n1}}{\partial \bar{x}} + \frac{\partial^2 A_{n0}}{\partial \bar{x}^2}(1 + 2nz)\mathrm{e}^{nz} + \frac{\partial^2 A_{n0}}{\partial \bar{y}^2}\mathrm{e}^{nz} = 0 \tag{34}$$

which has the solution:

$$A'_{n2} = A_{n2}(\bar{x}, \bar{y}, \bar{t})\mathrm{e}^{nz} - \mathrm{i}\frac{\partial A_{n1}}{\partial \bar{x}}z\mathrm{e}^{nz} - \frac{1}{2n}\frac{\partial^2 A_{n0}}{\partial \bar{y}^2}z\mathrm{e}^{nz} - \frac{1}{2}\frac{\partial^2 A_{n0}}{\partial \bar{x}^2}z^2\mathrm{e}^{nz} \tag{35}$$

Fourth order To fourth order the continuity equation for A'_n (27) is:

$$\frac{\partial^2 A'_{n3}}{\partial z^2} - n^2 A'_{n3} + 2\mathrm{i}n\frac{\partial A'_{n2}}{\partial \bar{x}} + \frac{\partial^2 A'_{n1}}{\partial \bar{x}^2} + \frac{\partial^2 A'_{n1}}{\partial \bar{y}^2} = 0 \qquad (36)$$

where $\frac{\partial A'_{n3}}{\partial z} \to 0$ as $z \to -\infty$.

Using the result from first, second, and third order (29, 32, 35) gives:

$$\frac{\partial^2 A'_{n3}}{\partial z^2} - n^2 A'_{n3} + 2\mathrm{i}n\frac{\partial A_{n2}}{\partial \bar{x}} + \frac{\partial^2 A_{n1}}{\partial \bar{x}^2}(1 + 2nz)\mathrm{e}^{nz} + \frac{\partial^2 A_{n1}}{\partial \bar{y}^2}\mathrm{e}^{nz}$$

$$-2\mathrm{i}\frac{\partial^3 A_{n0}}{\partial \bar{x}\partial \bar{y}^2}z\mathrm{e}^{nz} - \mathrm{i}\frac{\partial^3 A_{n1}}{\partial \bar{x}^3}z(1 + nz)\mathrm{e}^{nz} = 0 \,(37)$$

which has the solution:

$$A'_{n3} = A_{n3}(\bar{x}, \bar{y}, \bar{t})\mathrm{e}^{nz} - \mathrm{i}\frac{\partial A_{n2}}{\partial \bar{x}}z\mathrm{e}^{nz} - \frac{1}{2n}\frac{\partial^2 A_{n1}}{\partial \bar{y}^2}z\mathrm{e}^{nz} - \frac{1}{2}\frac{\partial^2 A_{n1}}{\partial \bar{x}^2}z^2\mathrm{e}^{nz}$$

$$-\frac{\mathrm{i}}{2n^2}\frac{\partial^3 A_{n0}}{\partial \bar{x}\partial \bar{y}^2}z(1 - nz)\mathrm{e}^{nz} + \frac{\mathrm{i}}{6}\frac{\partial^3 A_{n0}}{\partial \bar{x}^3}z^3\mathrm{e}^{nz} \qquad (38)$$

Defines $A_n = A_{n0} + \epsilon A_{n1} + \epsilon^2 A_{n2} + \cdots$ which gives:

$$A'_n = A_n\mathrm{e}^{nz} - \mathrm{i}\epsilon\frac{\partial A_n}{\partial \bar{x}}z\mathrm{e}^{nz} - \epsilon^2\left(\frac{1}{2n}\frac{\partial^2 A_n}{\partial \bar{y}^2}z + \frac{1}{2}\frac{\partial^2 A_n}{\partial \bar{x}^2}z^2\right)\mathrm{e}^{nz}$$

$$+\epsilon^3\left(\frac{\mathrm{i}}{2n^2}\frac{\partial^3 A_n}{\partial \bar{x}\partial \bar{y}^2}z(nz - 1) + \frac{\mathrm{i}}{6}\frac{\partial^3 A_n}{\partial \bar{x}^3}z^3\right)\mathrm{e}^{nz} + O(\epsilon^4) \qquad (39)$$

3.1.2 Surface equations

The scaled surface equations (23–24) to the fourth order of ϵ are given by:

$$\frac{\partial \eta}{\partial t} + \epsilon\frac{\partial \phi}{\partial x}\frac{\partial \eta}{\partial x} + \epsilon U\frac{\partial \eta}{\partial x} + \epsilon^2\eta\frac{\partial^2 \phi}{\partial x\partial z}\frac{\partial \eta}{\partial x} + \frac{1}{2}\epsilon^3\eta^2\frac{\partial^3 \phi}{\partial x\partial z^2}\frac{\partial \eta}{\partial x} + \epsilon^3\eta\frac{\partial U}{\partial z}\frac{\partial \eta}{\partial x}$$

$$+\epsilon^3\zeta\frac{\partial^2 \phi}{\partial x\partial z}\frac{\partial \eta}{\partial x} + \epsilon\frac{\partial \phi}{\partial y}\frac{\partial \eta}{\partial y} + \epsilon V\frac{\partial \eta}{\partial y} + \epsilon^2\eta\frac{\partial^2 \phi}{\partial y\partial z}\frac{\partial \eta}{\partial y} + \frac{1}{2}\epsilon^3\eta^2\frac{\partial^3 \phi}{\partial y\partial z^2}\frac{\partial \eta}{\partial y}$$

$$+\epsilon^3\eta\frac{\partial V}{\partial z}\frac{\partial \eta}{\partial y} + \epsilon^3\zeta\frac{\partial^2 \phi}{\partial y\partial z}\frac{\partial \eta}{\partial y}$$

$$= \frac{\partial \phi}{\partial z} + \epsilon\eta\frac{\partial^2 \phi}{\partial z^2} + \epsilon^2\zeta\frac{\partial^2 \phi}{\partial z^2} + \frac{1}{2}\epsilon^2\eta^2\frac{\partial^3 \phi}{\partial z^3} + \epsilon^3\eta\zeta\frac{\partial^3 \phi}{\partial z^3} + \frac{1}{6}\epsilon^3\eta^3\frac{\partial^4 \phi}{\partial z^4}$$

$$+O(\epsilon^4) \qquad (40)$$

$$\frac{\partial \phi}{\partial t} + \epsilon\eta\frac{\partial^2 \phi}{\partial t\partial z} + \epsilon^2\zeta\frac{\partial^2 \phi}{\partial t\partial z} + \frac{1}{2}\epsilon^2\eta^2\frac{\partial^3 \phi}{\partial t\partial z^2} + \epsilon^3\eta\zeta\frac{\partial^3 \phi}{\partial t\partial z^2} + \frac{1}{6}\epsilon^3\eta^3\frac{\partial^4 \phi}{\partial t\partial z^3}$$

13

$$+\frac{1}{2}\epsilon\left(\frac{\partial\phi}{\partial x}\right)^2 + \epsilon U\frac{\partial\phi}{\partial x} + \epsilon^2\eta\frac{\partial\phi}{\partial x}\frac{\partial^2\phi}{\partial x\partial z} + \epsilon^2\eta U\frac{\partial^2\phi}{\partial x\partial z} + \frac{1}{2}\epsilon^3\eta^2\left(\frac{\partial^2\phi}{\partial x\partial z}\right)^2$$

$$+\frac{1}{2}\epsilon^3\eta^2\frac{\partial\phi}{\partial x}\frac{\partial^3\phi}{\partial x\partial z^2} + \frac{1}{2}\epsilon^3\eta^2 U\frac{\partial^3\phi}{\partial x\partial z^2} + \epsilon^3\eta\frac{\partial\phi}{\partial x}\frac{\partial U}{\partial z} + \epsilon^3\zeta\frac{\partial\phi}{\partial x}\frac{\partial^2\phi}{\partial x\partial z}$$

$$+\epsilon^3\zeta U\frac{\partial^2\phi}{\partial x\partial z} + \epsilon^3\eta U\frac{\partial U}{\partial z} + \frac{1}{2}\epsilon\left(\frac{\partial\phi}{\partial y}\right)^2 + \epsilon V\frac{\partial\phi}{\partial y} + \epsilon^2\eta\frac{\partial\phi}{\partial y}\frac{\partial^2\phi}{\partial y\partial z}$$

$$+\epsilon^2\eta V\frac{\partial^2\phi}{\partial y\partial z} + \frac{1}{2}\epsilon^3\eta^2\left(\frac{\partial^2\phi}{\partial y\partial z}\right)^2 + \frac{1}{2}\epsilon^3\eta^2\frac{\partial\phi}{\partial y}\frac{\partial^3\phi}{\partial y\partial z^2} + \frac{1}{2}\epsilon^3\eta^2 V\frac{\partial^3\phi}{\partial y\partial z^2}$$

$$+\epsilon^3\eta\frac{\partial\phi}{\partial y}\frac{\partial V}{\partial z} + \epsilon^3\zeta\frac{\partial\phi}{\partial y}\frac{\partial^2\phi}{\partial y\partial z} + \epsilon^3\zeta V\frac{\partial^2\phi}{\partial y\partial z} + \epsilon^3\eta V\frac{\partial V}{\partial z} + \frac{1}{2}\epsilon\left(\frac{\partial\phi}{\partial z}\right)^2$$

$$+\epsilon^2\eta\frac{\partial\phi}{\partial z}\frac{\partial^2\phi}{\partial z^2} + \epsilon^3\zeta\frac{\partial\phi}{\partial z}\frac{\partial^2\phi}{\partial z^2} + \frac{1}{2}\epsilon^3\eta^2\left(\frac{\partial^2\phi}{\partial z^2}\right)^2 + \frac{1}{2}\epsilon^3\eta^2\frac{\partial\phi}{\partial z}\frac{\partial^3\phi}{\partial z^3} + \eta$$

$$= O(\epsilon^4) \tag{41}$$

First order   To first order of ϵ the surface equations (40–41) give:

$$B_{10} = \mathrm{i}A_{10} \tag{42}$$

Second order   The zeroth harmonic terms of second order of ϵ in the dynamic surface equation (41) are:

$$\frac{\mathrm{i}}{4}B_{10}A_{10}^* - \frac{\mathrm{i}}{4}A_{10}B_{10}^* + \frac{1}{2}|A_{10}|^2 + \bar{\eta}_1 = 0 \tag{43}$$

Using the results from first order (42) gives:

$$\bar{\eta}_1 = 0 \tag{44}$$

The first harmonic terms of second order of ϵ in the surface equations (40–41) are:

$$-\frac{\mathrm{i}}{2}B_{11} + \frac{1}{2}\frac{\partial B_{10}}{\partial\bar{t}} + \frac{\mathrm{i}}{2}B_{10}U = \frac{1}{2}A_{11} - \frac{\mathrm{i}}{2}\frac{\partial A_{10}}{\partial\bar{x}} \tag{45}$$

$$-\frac{\mathrm{i}}{2}A_{11} + \frac{1}{2}\frac{\partial A_{10}}{\partial\bar{t}} + \frac{\mathrm{i}}{2}A_{10}U + \frac{1}{2}B_{11} = 0 \tag{46}$$

Using the result from first order (42) gives the Schrödinger equation to linear order:

$$\frac{\partial A_{10}}{\partial\bar{x}} + 2\frac{\partial A_{10}}{\partial\bar{t}} + 2\mathrm{i}UA_{10} = 0 \tag{47}$$

14

and

$$B_{11} = iA_{11} - \frac{\partial A_{10}}{\partial \bar{t}} - iUA_{10} \tag{48}$$

The second harmonic terms to second order of ϵ of the surface equations (40–41) are:

$$-iB_{20} - \frac{1}{2}A_{10}B_{10} = A_{20} \tag{49}$$

$$-iA_{20} - \frac{i}{4}A_{10}B_{10} + \frac{1}{2}B_{20} = 0 \tag{50}$$

Using the result from first order (42) gives:

$$A_{20} = 0 \tag{51}$$

$$B_{20} = -\frac{1}{2}A_{10}^2 \tag{52}$$

Third order The zeroth harmonic terms to third order of ϵ in the surface equations (40–41) are:

$$\frac{\partial \bar{\eta}_1}{\partial \bar{t}} + \frac{i}{4}A_{10}\frac{\partial B_{10}^*}{\partial \bar{x}} - \frac{i}{4}B_{10}\frac{\partial A_{10}^*}{\partial \bar{x}} + \frac{i}{4}\frac{\partial A_{10}}{\partial \bar{x}}B_{10}^* - \frac{i}{4}\frac{\partial B_{10}}{\partial \bar{x}}A_{10}^* = \frac{\partial \bar{\phi}_1}{\partial z} \tag{53}$$

$$\frac{\partial \bar{\phi}_1}{\partial \bar{t}} + \frac{1}{4}B_{10}\frac{\partial A_{10}^*}{\partial \bar{t}} + \frac{i}{4}B_{10}A_{11}^* - \frac{1}{4}B_{10}\frac{\partial A_{10}^*}{\partial \bar{x}} + \frac{1}{4}\frac{\partial A_{10}}{\partial \bar{t}}B_{10}^* - \frac{i}{4}A_{11}B_{10}^*$$

$$-\frac{1}{4}\frac{\partial A_{10}}{\partial \bar{x}}B_{10}^* + \frac{i}{4}B_{11}A_{10}^* - \frac{i}{4}A_{10}B_{11}^* + \frac{1}{2}A_{11}A_{10}^* - \frac{i}{2}\frac{\partial A_{10}}{\partial \bar{x}}A_{10}^*$$

$$+\frac{1}{2}A_{10}A_{11}^* + \frac{i}{2}A_{10}\frac{\partial A_{10}^*}{\partial \bar{x}} - \frac{i}{4}UB_{10}A_{10}^* + \frac{i}{4}UA_{10}B_{10}^* + \bar{\eta}_2 = 0 \tag{54}$$

Using the results from first and second order (42, 44, 48) gives:

$$\frac{\partial \bar{\phi}_1}{\partial z} = -\frac{\partial |A_{10}|^2}{\partial \bar{t}} \tag{55}$$

$$\bar{\eta}_2 = -\frac{\partial \bar{\phi}_1}{\partial \bar{t}} \tag{56}$$

The first harmonic terms of third order of ϵ in the surface equations (40–41) are:

$$-\frac{i}{2}B_{12} + \frac{1}{2}\frac{\partial B_{11}}{\partial \bar{t}} - \frac{1}{2}A_{20}B_{10}^* + \frac{1}{4}B_{20}A_{10}^* + \frac{i}{2}UB_{11}$$

$$+\frac{1}{2}U\frac{\partial B_{10}}{\partial \bar{x}} + \frac{1}{2}V\frac{\partial B_{10}}{\partial \bar{y}} - \frac{1}{8}|B_{10}|^2A_{10} + \frac{1}{16}B_{10}^2A_{10}^*$$

15

$$= \frac{1}{2}A_{12} - \frac{i}{2}\frac{\partial A_{11}}{\partial \bar{x}} - \frac{1}{4}\frac{\partial^2 A_{10}}{\partial \bar{y}^2} + \frac{1}{2}\bar{\eta}_1 A_{10} + \frac{1}{2}\zeta A_{10} \tag{57}$$

$$-\frac{i}{2}A_{12} + \frac{1}{2}\frac{\partial A_{11}}{\partial \bar{t}} - \frac{i}{2}\bar{\eta}_1 A_{10} + \frac{i}{4}B_{20}A_{10}^* - iA_{20}B_{10}^* - \frac{i}{2}\zeta A_{10}$$

$$+\frac{i}{16}B_{10}^2 A_{10}^* - \frac{i}{8}|B_{10}|^2 A_{10} + A_{20}A_{10}^* + \frac{i}{2}U A_{11}$$

$$+\frac{1}{2}U\frac{\partial A_{10}}{\partial \bar{x}} + \frac{1}{2}V\frac{\partial A_{10}}{\partial \bar{y}} + \frac{1}{2}|A_{10}|^2 B_{10} + \frac{1}{2}B_{12} = 0 \tag{58}$$

Using the results from first and second order (42, 44, 47–48, 51–52) gives the current modified cubic nonlinear Schrödinger equation:

$$\frac{\partial A_{11}}{\partial \bar{x}} + 2\frac{\partial A_{11}}{\partial \bar{t}} + 2iU A_{11} + i\frac{\partial^2 A_{10}}{\partial \bar{t}^2} - 6U\frac{\partial A_{10}}{\partial \bar{t}}$$

$$+i|A_{10}|^2 A_{10} - 5iU^2 A_{10} + 2V\frac{\partial A_{10}}{\partial \bar{y}} - \frac{i}{2}\frac{\partial^2 A_{10}}{\partial \bar{y}^2} = 0 \tag{59}$$

and

$$B_{12} = iA_{12} - \frac{\partial A_{11}}{\partial \bar{t}} + i\zeta A_{10} - \frac{3i}{8}|A_{10}|^2 A_{10} - iU A_{11}$$

$$+2U\frac{\partial A_{10}}{\partial \bar{t}} + 2iU^2 A_{10} - V\frac{\partial A_{10}}{\partial \bar{y}} \tag{60}$$

The second harmonic terms of third order of ϵ in the surface equations (40–41) are:

$$-iB_{21} + \frac{1}{2}\frac{\partial B_{20}}{\partial \bar{t}} - \frac{1}{2}A_{10}B_{11} + \frac{i}{4}A_{10}\frac{\partial B_{10}}{\partial \bar{x}} - \frac{1}{2}B_{10}A_{11} + \frac{3i}{4}\frac{\partial A_{10}}{\partial \bar{x}}B_{10}$$

$$+iUB_{20} = A_{21} - \frac{i}{2}\frac{\partial A_{20}}{\partial \bar{x}} \tag{61}$$

$$-iA_{21} + \frac{1}{2}\frac{\partial A_{20}}{\partial \bar{t}} - \frac{i}{4}B_{10}A_{11} - \frac{1}{4}B_{10}\frac{\partial A_{10}}{\partial \bar{x}} + \frac{1}{4}B_{10}\frac{\partial A_{10}}{\partial \bar{t}} - \frac{i}{4}A_{10}B_{11}$$

$$+iUA_{20} + \frac{i}{4}U A_{10}B_{10} + \frac{1}{2}B_{21} = 0 \tag{62}$$

Using the results from first and second order (42, 47–48, 51–52) gives:

$$A_{21} = 0 \tag{63}$$

$$B_{21} = -2iA_{10}\frac{\partial A_{10}}{\partial \bar{t}} - A_{10}A_{11} + 2U A_{10}^2 \tag{64}$$

The third harmonic terms of third order of ϵ in the surface equations (40–41) are:

$$-\frac{3i}{2}B_{30} - \frac{3}{4}A_{10}B_{20} - \frac{3}{2}A_{20}B_{10} - \frac{3}{16}B_{10}^2 A_{10} = \frac{3}{2}A_{30} \tag{65}$$

$$-\frac{3i}{2}A_{30} - iB_{10}A_{20} - \frac{i}{4}B_{20}A_{10} - \frac{i}{16}B_{10}^2 A_{10} + \frac{1}{2}B_{30} = 0 \tag{66}$$

Using the results from first and second order (42, 51–52) gives:

$$A_{30} = 0 \tag{67}$$

$$B_{30} = -\frac{3i}{8}A_{10}^3 \tag{68}$$

Fourth order   The first harmonic terms of fourth order of ϵ in the surface equations (40–41) are:

$$
\begin{aligned}
&-\frac{i}{2}B_{13} + \frac{1}{2}\frac{\partial B_{12}}{\partial \bar{t}} + \frac{i}{2}\frac{\partial \bar{\phi}_1}{\partial \bar{x}}B_{10} + \frac{i}{2}\frac{\partial \bar{\eta}_1}{\partial \bar{x}}A_{10} + i\bar{\eta}_1\frac{\partial A_{10}}{\partial \bar{x}} - \frac{1}{2}\bar{\eta}_1 A_{11} - \frac{1}{2}\bar{\eta}_2 A_{10} \\
&\quad -\frac{1}{2}A_{20}B_{11}^* - \frac{1}{2}A_{21}B_{10}^* + \frac{1}{4}B_{20}A_{11}^* + \frac{1}{4}B_{21}A_{10}^* - \frac{1}{8}A_{10}B_{11}B_{10}^* \\
&\quad -\frac{1}{8}A_{10}B_{10}B_{11}^* + \frac{1}{8}B_{10}B_{11}A_{10}^* + \frac{1}{16}B_{10}^2 A_{11}^* - \frac{1}{8}|B_{10}|^2 A_{11} \\
&\quad +\frac{i}{2}A_{20}\frac{\partial B_{10}^*}{\partial \bar{x}} + \frac{i}{8}A_{10}B_{10}\frac{\partial B_{10}^*}{\partial \bar{x}} + \frac{i}{16}B_{10}^2\frac{\partial A_{10}^*}{\partial \bar{x}} + \frac{3i}{8}|B_{10}|^2\frac{\partial A_{10}}{\partial \bar{x}} \\
&\quad +\frac{3i}{4}\frac{\partial A_{20}}{\partial \bar{x}}B_{10}^* - \frac{i}{4}\frac{\partial B_{20}}{\partial \bar{x}}A_{10}^* + \frac{i}{8}A_{10}\frac{\partial B_{10}}{\partial \bar{x}}B_{10}^* - \frac{i}{8}B_{10}\frac{\partial B_{10}}{\partial \bar{x}}A_{10}^* \\
&\quad +\frac{i}{2}UB_{12} + \frac{1}{2}U\frac{\partial B_{11}}{\partial \bar{x}} + \frac{1}{2}V\frac{\partial B_{11}}{\partial \bar{y}} - \frac{1}{2}\zeta A_{11} + i\zeta\frac{\partial A_{10}}{\partial \bar{x}} \\
&= \frac{1}{2}A_{13} - \frac{i}{2}\frac{\partial A_{12}}{\partial \bar{x}} - \frac{1}{4}\frac{\partial^2 A_{11}}{\partial \bar{y}^2} - \frac{i}{4}\frac{\partial^3 A_{10}}{\partial \bar{x}\partial \bar{y}^2}
\end{aligned}
\tag{69}
$$

$$
\begin{aligned}
&-\frac{i}{2}A_{13} + \frac{1}{2}B_{13} + \frac{1}{2}\frac{\partial A_{12}}{\partial \bar{t}} + \frac{i}{2}\frac{\partial \bar{\phi}_1}{\partial \bar{x}}A_{10} + \frac{1}{2}\frac{\partial \bar{\phi}_1}{\partial z}A_{10} - \frac{i}{2}\bar{\eta}_1 A_{11} - \frac{1}{2}\bar{\eta}_1\frac{\partial A_{10}}{\partial \bar{x}} \\
&\quad +\frac{1}{2}\bar{\eta}_1\frac{\partial A_{10}}{\partial \bar{t}} - \frac{i}{2}\bar{\eta}_2 A_{10} - iA_{20}B_{11}^* + 2A_{20}A_{11}^* + 2A_{21}A_{10}^* - iA_{21}B_{10}^* \\
&\quad +\frac{i}{4}B_{20}A_{11}^* + \frac{i}{4}B_{21}A_{10}^* + \frac{1}{2}A_{10}B_{11}A_{10}^* - \frac{i}{8}A_{10}B_{11}B_{10}^* \\
&\quad +\frac{1}{2}A_{10}B_{10}A_{11}^* - \frac{i}{8}A_{10}B_{10}B_{11}^* + \frac{1}{2}A_{11}B_{10}A_{10}^* - \frac{i}{8}B_{10}A_{11}B_{10}^* \\
&\quad +\frac{i}{8}B_{10}B_{11}A_{10}^* + \frac{i}{16}B_{10}^2 A_{11}^* + 2iA_{20}\frac{\partial A_{10}^*}{\partial \bar{x}} - \frac{1}{4}B_{20}\frac{\partial A_{10}^*}{\partial \bar{x}} + \frac{1}{4}B_{20}\frac{\partial A_{10}^*}{\partial \bar{t}} \\
&\quad +\frac{3i}{4}A_{10}B_{10}\frac{\partial A_{10}^*}{\partial \bar{x}} - \frac{1}{8}B_{10}^2\frac{\partial A_{10}^*}{\partial \bar{x}} + \frac{1}{16}B_{10}^2\frac{\partial A_{10}^*}{\partial \bar{t}} - i\frac{\partial A_{20}}{\partial \bar{x}}A_{10}^* \\
&\quad -\frac{1}{2}\frac{\partial A_{20}}{\partial \bar{x}}B_{10}^* + \frac{1}{2}\frac{\partial A_{20}}{\partial \bar{t}}B_{10}^* - \frac{3i}{4}B_{10}\frac{\partial A_{10}}{\partial \bar{x}}A_{10}^* - \frac{1}{4}B_{10}\frac{\partial A_{10}}{\partial \bar{x}}B_{10}^* \\
&\quad +\frac{1}{8}B_{10}\frac{\partial A_{10}}{\partial \bar{t}}B_{10}^* + \frac{i}{2}UA_{12} + iUA_{20}B_{10}^* - \frac{i}{4}UB_{20}A_{10}^* - \frac{i}{16}UB_{10}^2 A_{10}^* \\
&\quad +\frac{i}{8}U|B_{10}|^2 A_{10} + \frac{1}{2}U\frac{\partial A_{11}}{\partial \bar{x}} + \frac{1}{2}V\frac{\partial A_{11}}{\partial \bar{y}} + \frac{1}{2}U\frac{\partial U}{\partial z}B_{10} + \frac{1}{2}V\frac{\partial V}{\partial z}B_{10}
\end{aligned}
$$

17

$$-\frac{\mathrm{i}}{2}\zeta A_{11} - \frac{1}{2}\zeta\frac{\partial A_{10}}{\partial\overline{x}} + \frac{1}{2}\zeta\frac{\partial A_{10}}{\partial\overline{t}} + \frac{\mathrm{i}}{2}\zeta U A_{10}$$
$$= 0 \tag{70}$$

Using the results from first, second and third order (42, 44, 47–48, 51–52, 55–56, 59–60, 63–64, 67–68) gives the current modified nonlinear Schrödinger equation built on potential theory to Dysthe level, MNLSC:

$$\frac{\partial A_{12}}{\partial\overline{x}} + 2\frac{\partial A_{12}}{\partial\overline{t}} + \mathrm{i}\frac{\partial^2 A_{11}}{\partial\overline{t}^2} + 2\mathrm{i}\frac{\partial\overline{\phi}_1}{\partial\overline{x}}A_{10} - \frac{\mathrm{i}}{2}\frac{\partial^2 A_{11}}{\partial\overline{y}^2} - \frac{\partial^3 A_{10}}{\partial\overline{t}\partial\overline{y}^2}$$
$$-8A_{10}\frac{\partial A_{10}}{\partial\overline{t}}A_{10}^* + \mathrm{i}A_{10}^2 A_{11}^* + 2\mathrm{i}A_{10}A_{11}A_{10}^* + 2\mathrm{i}U A_{12} - 6U\frac{\partial A_{11}}{\partial\overline{t}}$$
$$-6\mathrm{i}U\frac{\partial^2 A_{10}}{\partial\overline{t}^2} - 10\mathrm{i}U A_{10}^2 A_{10}^* + 2V\frac{\partial A_{11}}{\partial\overline{y}} + 2\mathrm{i}V\frac{\partial^2 A_{10}}{\partial\overline{t}\partial\overline{y}} - 5\mathrm{i}U^2 A_{11}$$
$$+20U^2\frac{\partial A_{10}}{\partial\overline{t}} + \mathrm{i}U\frac{\partial U}{\partial z}A_{10} - 6UV\frac{\partial A_{10}}{\partial\overline{y}} + \mathrm{i}V\frac{\partial V}{\partial z}A_{10} + 14\mathrm{i}U^3 A_{10}$$
$$= 0 \tag{71}$$

3.1.3   Summary

In the following $A = A_1$, $B = B_1$, and $(\overline{x},\overline{y},\overline{t}) = (x,y,t)$ to simplify the notation.

Space evolution of A   The space evolution of the MNLSC equation (71) expressed by modulation of A is:

$$\frac{\partial A}{\partial x} + 2\frac{\partial A}{\partial t} + 2iUA$$
$$+\mathrm{i}\frac{\partial^2 A}{\partial t^2} - \frac{\mathrm{i}}{2}\frac{\partial^2 A}{\partial y^2} + \mathrm{i}A|A|^2 - 6U\frac{\partial A}{\partial t} - 5\mathrm{i}U^2 A + 2V\frac{\partial A}{\partial y}$$
$$+2\mathrm{i}\frac{\partial\overline{\phi}}{\partial x}A - \frac{\partial^3 A}{\partial t\partial y^2} - 8|A|^2\frac{\partial A}{\partial t} - 6\mathrm{i}U\frac{\partial^2 A}{\partial t^2} - 10\mathrm{i}U A|A|^2 + 2\mathrm{i}V\frac{\partial^2 A}{\partial t\partial y}$$
$$+20U^2\frac{\partial A}{\partial t} + \mathrm{i}U\frac{\partial U}{\partial z}A - 6UV\frac{\partial A}{\partial y} + \mathrm{i}V\frac{\partial V}{\partial z}A + 14\mathrm{i}U^3 A = 0 \tag{72}$$

and

$$\frac{\partial\overline{\phi}}{\partial z} = -\frac{\partial|A|^2}{\partial t} \qquad \text{when } z = 0 \tag{73}$$

$$4\frac{\partial^2\overline{\phi}}{\partial t^2} + \frac{\partial^2\overline{\phi}}{\partial y^2} + \frac{\partial^2\overline{\phi}}{\partial z^2} = 0 \qquad \text{when } z < 0 \tag{74}$$

$$\frac{\partial\overline{\phi}}{\partial z} = 0 \qquad \text{when } z \to -\infty \tag{75}$$

18

with the following reconstruction formulas:

$$
\begin{aligned}
\overline{\eta} &= -\frac{\partial \overline{\phi}}{\partial t} \\
A_2, A_3 &= 0 \\
B &= iA - \frac{\partial A}{\partial t} - iUA + i\zeta A - \frac{3i}{8}A|A|^2 + 2U\frac{\partial A}{\partial t} + 2iU^2A - V\frac{\partial A}{\partial y} \\
B_2 &= -\frac{1}{2}A^2 - 2iA\frac{\partial A}{\partial t} + 2UA^2 \\
B_3 &= -\frac{3i}{8}A^3
\end{aligned}
$$

Space evolution of B The space evolution of the MNLSC equation (71) expressed by modulation of B is:

$$
\frac{\partial B}{\partial x} + 2\frac{\partial B}{\partial t} + 2iUB
$$
$$
+i\frac{\partial^2 B}{\partial t^2} - \frac{i}{2}\frac{\partial^2 B}{\partial y^2} + iB|B|^2 - 6U\frac{\partial B}{\partial t} - 5iU^2 B + 2V\frac{\partial B}{\partial y} - 4i\frac{\partial \overline{\phi_1}}{\partial t}B
$$
$$
-\frac{\partial^3 B}{\partial t \partial y^2} - 8|B|^2\frac{\partial B}{\partial t} - 2B^2\frac{\partial B^*}{\partial t} - 6iU\frac{\partial^2 B}{\partial t^2} - 8iU|B|^2 B + 2iV\frac{\partial^2 B}{\partial t \partial y}
$$
$$
+20U^2\frac{\partial B}{\partial t} + iU\frac{\partial U}{\partial z}B - 6UV\frac{\partial B}{\partial y} + iV\frac{\partial V}{\partial z}B + 14iU^3 B = 0 \qquad (76)
$$

and

$$
\frac{\partial \overline{\phi}}{\partial z} = -\frac{\partial |B|^2}{\partial t} \qquad \text{when } z = 0 \qquad (77)
$$
$$
\frac{\partial^2 \overline{\phi}}{\partial x^2} + \frac{\partial^2 \overline{\phi}}{\partial y^2} + \frac{\partial^2 \overline{\phi}}{\partial z^2} = 0 \qquad \text{when } z < 0 \qquad (78)
$$
$$
\frac{\partial \overline{\phi}}{\partial z} = 0 \qquad \text{when } z \to -\infty \qquad (79)
$$

with the following reconstruction formulas:

$$
\begin{aligned}
\overline{\eta} &= -\frac{\partial \overline{\phi}}{\partial t} \\
A &= -iB - \frac{\partial B}{\partial t} - iUB + i\frac{\partial^2 B}{\partial t^2} + i\zeta B - \frac{3i}{8}|B|^2 B + iU^2 B - V\frac{\partial B}{\partial y} \\
A_2, A_3 &= 0 \\
B_2 &= \frac{1}{2}B^2 + iB\frac{\partial B}{\partial t} - UB^2 \\
B_3 &= \frac{3}{8}B^3
\end{aligned}
$$

Time evolution of A   The time evolution of the MNLSC equation (71) expressed by modulation of A is:

$$\frac{\partial A}{\partial t} + \frac{1}{2}\frac{\partial A}{\partial x} + iUA$$
$$+ \frac{i}{8}\frac{\partial^2 A}{\partial x^2} - \frac{i}{4}\frac{\partial^2 A}{\partial y^2} + \frac{i}{2}A|A|^2 + U\frac{\partial A}{\partial x} + V\frac{\partial A}{\partial y}$$
$$+ i\frac{\partial\overline{\phi}}{\partial x}A - \frac{1}{16}\frac{\partial^3 A}{\partial x^3} + \frac{3}{8}\frac{\partial^3 A}{\partial x\partial y^2} + \frac{3}{2}|A|^2\frac{\partial A}{\partial x} - \frac{1}{4}A^2\frac{\partial A^*}{\partial x}$$
$$+ \frac{i}{2}U\frac{\partial U}{\partial z}A + \frac{i}{2}V\frac{\partial V}{\partial z}A = 0 \qquad\qquad (80)$$

and

$$\frac{\partial\overline{\phi}}{\partial z} = \frac{1}{2}\frac{\partial|A|^2}{\partial x} \qquad \text{when } z = 0 \qquad (81)$$

$$\frac{\partial^2\overline{\phi}}{\partial x^2} + \frac{\partial^2\overline{\phi}}{\partial y^2} + \frac{\partial^2\overline{\phi}}{\partial z^2} = 0 \qquad \text{when } z < 0 \qquad (82)$$

$$\frac{\partial\overline{\phi}}{\partial z} = 0 \qquad \text{when } z \to -\infty \qquad (83)$$

with the following reconstruction formulas:

$$\overline{\eta} = \frac{1}{2}\frac{\partial\overline{\phi}}{\partial x}$$
$$A_2, A_3 = 0$$
$$B = iA + \frac{1}{2}\frac{\partial A}{\partial x} + i\zeta A + \frac{i}{8}A|A|^2 + \frac{i}{8}\frac{\partial^2 A}{\partial x^2} - \frac{i}{4}\frac{\partial^2 A}{\partial y^2}$$
$$B_2 = -\frac{1}{2}A^2 + iA\frac{\partial A}{\partial x}$$
$$B_3 = -\frac{3i}{8}A^3$$

Time evolution of B   The time evolution of the MNLSC equation (71) expressed by modulation of B is:

$$\frac{\partial B}{\partial t} + \frac{1}{2}\frac{\partial B}{\partial x} + iUB$$
$$+ \frac{i}{8}\frac{\partial^2 B}{\partial x^2} - \frac{i}{4}\frac{\partial^2 B}{\partial y^2} + \frac{i}{2}|B|^2 B + U\frac{\partial B}{\partial x} + V\frac{\partial B}{\partial y}$$
$$- \frac{1}{16}\frac{\partial^3 B}{\partial x^3} + \frac{3}{8}\frac{\partial^3 B}{\partial x\partial y^2} + \frac{3}{2}B\frac{\partial B}{\partial x}B^* + \frac{1}{4}B^2\frac{\partial B^*}{\partial x} + i\frac{\partial\overline{\phi}_1}{\partial x}B$$
$$+ \frac{i}{2}U\frac{\partial U}{\partial z}B + \frac{i}{2}V\frac{\partial V}{\partial z}B - \frac{i}{2}U|B|^2 B = 0 \qquad\qquad (84)$$

and

$$\frac{\partial \overline{\phi}}{\partial z} = \frac{1}{2}\frac{\partial |B|^2}{\partial x} \qquad \text{when } z = 0 \qquad (85)$$

$$\frac{\partial^2 \overline{\phi}}{\partial x^2} + \frac{\partial^2 \overline{\phi}}{\partial y^2} + \frac{\partial^2 \overline{\phi}}{\partial z^2} = 0 \qquad \text{when } z < 0 \qquad (86)$$

$$\frac{\partial \overline{\phi}}{\partial z} = 0 \qquad \text{when } z \to -\infty \qquad (87)$$

with the following reconstruction formulas:

$$\overline{\eta} = \frac{1}{2}\frac{\partial \overline{\phi}}{\partial x}$$

$$A = -\mathrm{i}B + \frac{1}{2}\frac{\partial B}{\partial x} + \frac{3\mathrm{i}}{8}\frac{\partial^2 B}{\partial x^2} - \frac{\mathrm{i}}{4}\frac{\partial^2 B}{\partial y^2} + \frac{\mathrm{i}}{8}|B|^2 B + \mathrm{i}\zeta B$$

$$A_2, A_3 = 0$$

$$B_2 = \frac{1}{2}B^2 - \frac{\mathrm{i}}{2}B\frac{\partial B}{\partial x}$$

$$B_3 = \frac{3}{8}B^3$$

The CNLS[4] equation by Stocker & Peregrine (1999) may be derived from (84) by rescaling.

3.2 Current field with horizontal shear

If the current field is rotational, vorticity develops in the wave field according to (19).

The divergence of the Euler equation for the waves (18) is:

$$\nabla \cdot (\boldsymbol{v} \cdot \nabla \boldsymbol{v} + \boldsymbol{v} \cdot \nabla \boldsymbol{V} + \boldsymbol{V} \cdot \nabla \boldsymbol{v}) = -\frac{1}{\rho}\nabla^2 p \qquad (88)$$

The surface equations for the combined field at $z = \eta + \zeta$ can be written as:

$$\frac{\partial \eta}{\partial t} + \boldsymbol{v}_{tot} \cdot \boldsymbol{\nabla}(\eta + \zeta) = w + W \qquad (89)$$

$$p_{tot} = p \qquad (90)$$

Taylor expansions around $z = 0$ gives (89–90) on the form:

$$\frac{\partial \eta}{\partial t} + \boldsymbol{v}_{tot} \cdot \boldsymbol{\nabla}(\eta + \zeta) + (\eta + \zeta)\frac{\partial \boldsymbol{v}_{tot}}{\partial z} \cdot \boldsymbol{\nabla}(\eta + \zeta) + \frac{1}{2}(\eta + \zeta)^2\frac{\partial^2 \boldsymbol{v}_{tot}}{\partial z^2} \cdot \boldsymbol{\nabla}(\eta + \zeta)$$

$$= w + W + (\eta + \zeta)\frac{\partial}{\partial z}(w + W) + \frac{1}{2}(\eta + \zeta)\frac{\partial^2}{\partial z^2}(w + W) + \cdots \tag{91}$$

$$p_{tot} + (\eta + \zeta)\frac{\partial p_{tot}}{\partial z} + \frac{1}{2}(\eta + \zeta)^2\frac{\partial^2 p_{tot}}{\partial z^2} + \cdots = p_a \tag{92}$$

The waves are assumed on deep water, thus $\boldsymbol{v}, p \to 0$ as $z \to -\infty$.

Let the current vary more slowly on a length scale along the x–axis, X, than along the y–axis, Y, so that $1/(k_c X) = O(\epsilon)$ and $1/(k_c Y) = O(1)$. In accordance with the scaling assumptions, all equations, variables, and sizes in the following are made dimensionless using the characteristic length and time scales of the wave field, so that $k_c\boldsymbol{x} \to \boldsymbol{x}$, $\epsilon k_c\boldsymbol{x} \to \bar{\boldsymbol{x}}$, $\omega_c t \to t$, $k_c\eta \to \epsilon\eta$, $k_c\zeta \to \epsilon^2\zeta$, $\frac{k_c}{\omega_c}\boldsymbol{v} \to \epsilon\boldsymbol{v}$, $\frac{k_c}{\omega_c}(U, V) \to \epsilon(U, V)$, $\frac{k_c}{\omega_c}W \to \epsilon^4 W$, $\frac{k_c}{\rho g}p \to \epsilon p$, and $\frac{k_c}{\rho g}P \to \epsilon^3 P$.

Note that in Hjelmervik & Trulsen (2009) the scaling is slightly changed. Since the waves are modulated on a length scale of order ϵ, the transversal length scale of the current is also assumed of order ϵ. And the vertical surface velocity of the current is assumed of one order lower.

The scaled equation for the divergence of the Euler equation for the waves (88) to the fourth order of ϵ is:

$$\epsilon\left(\left(\frac{\partial u}{\partial x}\right)^2 + \left(\frac{\partial v}{\partial u}\right)^2 + \left(\frac{\partial w}{\partial z}\right)^2 + 2\frac{\partial u}{\partial y}\frac{\partial v}{\partial x} + 2\frac{\partial u}{\partial z}\frac{\partial w}{\partial x} + 2\frac{\partial v}{\partial z}\frac{\partial w}{\partial y} + 2\frac{\partial v}{\partial x}\frac{\partial U}{\partial y} + 2\frac{\partial v}{\partial y}\frac{\partial V}{\partial y}\right)$$

$$+ \epsilon^2\left(2\frac{\partial u}{\partial x}\frac{\partial U}{\partial x} + 2\frac{\partial u}{\partial y}\frac{\partial V}{\partial x}\right) = -\frac{\partial^2 p}{\partial x^2} - \frac{\partial^2 p}{\partial y^2} - \frac{\partial^2 p}{\partial z^2} \tag{93}$$

The scaled Euler equation for the waves (18) to the fourth order of ϵ is:

$$\frac{\partial u}{\partial t} + \epsilon\left(U\frac{\partial u}{\partial x} + V\frac{\partial u}{\partial y} + v\frac{\partial U}{\partial y} + \boldsymbol{v}\cdot\boldsymbol{\nabla}u\right) + \epsilon^2 u\frac{\partial U}{\partial x} = -\frac{\partial p}{\partial x} \tag{94}$$

$$\frac{\partial v}{\partial t} + \epsilon\left(U\frac{\partial v}{\partial x} + V\frac{\partial v}{\partial y} + v\frac{\partial V}{\partial y} + \boldsymbol{v}\cdot\boldsymbol{\nabla}v\right) + \epsilon^2 u\frac{\partial V}{\partial x} = -\frac{\partial p}{\partial y} \tag{95}$$

$$\frac{\partial w}{\partial t} + \epsilon\left(U\frac{\partial w}{\partial x} + V\frac{\partial w}{\partial y} + \boldsymbol{v}\cdot\boldsymbol{\nabla}w\right) = -\frac{\partial p}{\partial z} \tag{96}$$

The scaled surface equations for the waves (91–92) to the fourth order of ϵ is:

$$\frac{\partial\eta}{\partial t} + \epsilon(\boldsymbol{v} + \boldsymbol{V})\cdot\boldsymbol{\nabla}\eta + \epsilon^2\left(v\frac{\partial\zeta}{\partial y} + \eta\frac{\partial\boldsymbol{v}}{\partial z}\cdot\boldsymbol{\nabla}\eta\right)$$

$$+ \epsilon^3\left(u\frac{\partial\zeta}{\partial x} + \eta\frac{\partial v}{\partial z}\frac{\partial\zeta}{\partial y} + \zeta\frac{\partial\boldsymbol{v}}{\partial z}\cdot\boldsymbol{\nabla}\eta + \frac{1}{2}\eta^2\frac{\partial^2\boldsymbol{v}}{\partial z^2}\cdot\boldsymbol{\nabla}\eta\right)$$

22

$$= w + \epsilon\eta\frac{\partial w}{\partial z} + \epsilon^2\left(\zeta\frac{\partial w}{\partial z} + \frac{1}{2}\eta^2\frac{\partial^2 w}{\partial z^2}\right) + \epsilon^3\left(\eta\zeta\frac{\partial^2 w}{\partial z^2} + \frac{1}{6}\eta^3\frac{\partial^3 w}{\partial z^3}\right) + O(\epsilon^4) \quad (97)$$

$$p - \eta + \epsilon\eta\frac{\partial p}{\partial z} + \epsilon^2\left(\zeta\frac{\partial p}{\partial z} + \frac{1}{2}\eta^2\frac{\partial^2 p}{\partial z^2}\right) + \epsilon^3\left(\eta\zeta\frac{\partial^2 p}{\partial z^2} + \frac{1}{6}\eta^3\frac{\partial^3 p}{\partial z^3}\right) = O(\epsilon^4) \quad (98)$$

The wave field is represented by perturbation series for the surface displacement, η, the velocity, $\boldsymbol{v}$, and the dynamic pressure, p:

$$
\begin{aligned}
\eta &= \epsilon\bar{\eta} + \tfrac{1}{2}\Big(B_1 e^{i(x-t)} + \epsilon B_2 e^{2i(x-t)} + \epsilon^2 B_3 e^{3i(x-t)} + \cdots + \text{c.c.}\Big) \\
\boldsymbol{v} &= \epsilon\bar{\boldsymbol{v}} + \tfrac{1}{2}\Big(\boldsymbol{v}_1 e^{i(x-t)} + \epsilon \boldsymbol{v}_2 e^{2i(x-t)} + \epsilon^2 \boldsymbol{v}_3 e^{3i(x-t)} + \cdots + \text{c.c.}\Big) \\
p &= \epsilon\bar{p} + \tfrac{1}{2}\Big(p_1 e^{i(x-t)} + \epsilon p_2 e^{2i(x-t)} + \epsilon^2 p_3 e^{3i(x-t)} + \cdots + \text{c.c.}\Big)
\end{aligned}
\quad (99)
$$

We shall assume that the waves are modulated on the slow spatial scales $\bar{x}$ and $\bar{y}$, and a correspondingly slow time scale $\epsilon t = \bar{t}$. Thus $\bar{\eta} = \bar{\eta}(\bar{x}, \bar{y}, \bar{t})$, $\boldsymbol{v} = \bar{\boldsymbol{v}}(\bar{x}, \bar{y}, z, \bar{t})$, and $\boldsymbol{p} = \bar{p}(\bar{x}, \bar{y}, z, \bar{t})$ are the mean surface displacement, mean induced velocity, and mean dynamic pressure respectively, while $B_n = B_n(\bar{x}, \bar{y}, \bar{t})$, $\boldsymbol{v}_n = \boldsymbol{v}_n(\bar{x}, \bar{y}, z, \bar{t})$, and $p_n = p_n(\bar{x}, \bar{y}, z, \bar{t})$ are the n'th harmonics of the surface displacement, induced current, and dynamic pressure respectively. The characteristic wavenumber is fixed appropriate for waves undisturbed by current, therefore the entire effect of refraction is represented by the modulation of B_1.

Both the mean functions and the harmonics, are perturbed:

$$
\begin{aligned}
\bar{\eta} &= \bar{\eta}_1 + \epsilon\bar{\eta}_2 + \cdots, & B_n &= B_{n0} + \epsilon B_{n1} + \epsilon^2 B_{n2} + \cdots \\
\bar{\boldsymbol{v}} &= \bar{\boldsymbol{v}}_1 + \epsilon\bar{\boldsymbol{v}}_2 + \cdots, & \boldsymbol{v}_n &= \boldsymbol{v}_{n0} + \epsilon \boldsymbol{v}_{n1} + \epsilon^2 \boldsymbol{v}_{n2} + \cdots \\
\bar{p} &= \bar{p}_1 + \epsilon\bar{p}_2 + \cdots, & p_n &= p_{n0} + \epsilon p_{n1} + \epsilon^2 p_{n2} + \cdots
\end{aligned}
\quad (100)
$$

3.2.1   First order terms

First harmonic   The first harmonic terms of first order of ϵ for the divergence of the Euler equation (93) are:

$$p_{10} - \frac{\partial^2 p_{10}}{\partial z^2} = 0 \quad (101)$$

which has the general solution:

$$p_{10} = A_{10}(\bar{x}, \bar{y}, \bar{t})e^z \quad (102)$$

The first harmonic terms of first order of ϵ in the surface equations (97–98) give:

$$A_{10} = B_{10} \quad (103)$$

23

The first harmonic terms of first order of ϵ in the Euler equation (94–96) then give respectively:

$$
\begin{align}
u_{10} &= B_{10}\mathrm{e}^z \tag{104}\\
v_{10} &= 0 \tag{105}\\
w_{10} &= -\mathrm{i}B_{10}\mathrm{e}^z \tag{106}
\end{align}
$$

3.2.2 Second order terms

Zeroth harmonic The zeroth harmonic terms of second order of ϵ for the z–component of the Euler equation (96) are:

$$
\frac{\mathrm{i}}{4}u_{10}w_{10}^* + \frac{\mathrm{i}}{4}u_{10}^*w_{10} + \frac{1}{4}w_{10}\frac{\partial w_{10}^*}{\partial z} + \frac{1}{4}w_{10}^*\frac{\partial w_{10}}{\partial z} = -\frac{\partial \bar{p}_1}{\partial z} \tag{107}
$$

Using the results from first order (104, 106) gives:

$$
|B_{10}|^2\mathrm{e}^{2z} = -\frac{\partial \bar{p}_1}{\partial z} \tag{108}
$$

which has the solution:

$$
\bar{p}_1 = \bar{A}_1(\bar{x}, \bar{y}, \bar{t})\mathrm{e}^z - \frac{1}{2}|B_{10}|^2\mathrm{e}^{2z} \tag{109}
$$

The zeroth harmonic terms of second order of ϵ in the dynamic surface equation (98) are:

$$
\bar{p}_1\big|_{z=0} - \bar{\eta}_1 + \frac{1}{4}B_{10}\frac{\partial p_{10}^*}{\partial z}\Big|_{z=0} + \frac{1}{4}B_{10}^*\frac{\partial p_{10}}{\partial z}\Big|_{z=0} = 0 \tag{110}
$$

Using the results from first order (102–103) and the solution for $\bar{p}_1$ (109) gives $\bar{A}_1 = \bar{\eta}_1$.

The zeroth harmonic terms of second order of ϵ in the kinematic surface equation (97) are:

$$
\begin{aligned}
-\frac{\mathrm{i}}{4}u_{10}\big|_{z=0}B_{10}^* &+ \frac{\mathrm{i}}{4}u_{10}^*\big|_{z=0}B_{10}\\
&= \bar{w}_1\big|_{z=0} + \frac{1}{4}B_{10}\frac{\partial w_{10}^*}{\partial z}\Big|_{z=0} + \frac{1}{4}B_{10}^*\frac{\partial w_{10}}{\partial z}\Big|_{z=0}
\end{aligned} \tag{111}
$$

Using the results from first order (104, 106) gives:

$$
\bar{w}_1\big|_{z=0} = 0 \tag{112}
$$

Since no surface elevation or induced current is provoked to first order of ϵ, $\bar{\eta}_1 = \bar{u}_1 = \bar{v}_1 = \bar{w}_1 = 0$ without lack of information.

First harmonic The first harmonic terms of second order of ϵ for the divergence of the Euler equation (93) are:

$$2\mathrm{i}v_{10}\frac{\partial U}{\partial y} + 2\mathrm{i}\frac{\partial p_{10}}{\partial \bar{x}} \;\; = \;\; p_{11} - \frac{\partial^2 p_{11}}{\partial z^2} \tag{113}$$

Using the results from first order (102–103, 105) gives:

$$2\mathrm{i}\frac{\partial B_{10}}{\partial \bar{x}}\mathrm{e}^z \;\; = \;\; p_{11} - \frac{\partial^2 p_{11}}{\partial z^2} \tag{114}$$

which has the solution:

$$p_{11} \;\; = \;\; A_{11}(\bar{x}, \bar{y}, \bar{t})\mathrm{e}^z - \mathrm{i}\frac{\partial B_{10}}{\partial \bar{x}}z\mathrm{e}^z \tag{115}$$

The first harmonic terms of second order of ϵ in the dynamic surface equation (98) give:

$$A_{11} \;\; = \;\; B_{11} \tag{116}$$

The first harmonic terms of second order of ϵ in the Euler equation and the kinematic surface equation (94–97) are respectively:

$$\frac{\partial u_{10}}{\partial \bar{t}} - \mathrm{i}u_{11} + \mathrm{i}u_{10}U + v_{10}\frac{\partial U}{\partial \bar{y}} \;\; = \;\; -\frac{\partial p_{10}}{\partial \bar{x}} - \mathrm{i}p_{11} \tag{117}$$

$$\frac{\partial v_{10}}{\partial \bar{t}} - \mathrm{i}v_{11} + \mathrm{i}v_{10}U + v_{10}\frac{\partial V}{\partial \bar{y}} \;\; = \;\; -\frac{\partial p_{10}}{\partial \bar{y}} \tag{118}$$

$$\frac{\partial w_{10}}{\partial \bar{t}} - \mathrm{i}w_{11} + \mathrm{i}w_{10}U \;\; = \;\; -\frac{\partial p_{11}}{\partial \bar{z}} \tag{119}$$

$$\frac{\partial B_{10}}{\partial \bar{t}} - \mathrm{i}B_{11} + \mathrm{i}UB_{10} \;\; = \;\; w_{11}\Big|_{z=0} \tag{120}$$

Using the results from first order (102–106) and the solution for p_{11} (115), leads to the current modified Schrödinger equation to linear order:

$$\frac{\partial B_{10}}{\partial \bar{x}} + 2\frac{\partial B_{10}}{\partial \bar{t}} + 2\mathrm{i}UB_{10} \;\; = \;\; 0 \tag{121}$$

and the following reconstruction formulas:

$$u_{11} \;\; = \;\; B_{11}\mathrm{e}^z + \mathrm{i}\left(\frac{\partial B_{10}}{\partial \bar{t}} + \mathrm{i}UB_{10}\right)(1 + 2z)\mathrm{e}^z \tag{122}$$

$$v_{11} \;\; = \;\; -\mathrm{i}\frac{\partial B_{10}}{\partial \bar{y}}\mathrm{e}^z \tag{123}$$

$$w_{11} \;\; = \;\; -\mathrm{i}B_{11}\mathrm{e}^z + \left(\frac{\partial B_{10}}{\partial \bar{t}} + \mathrm{i}UB_{10}\right)(1 + 2z)\mathrm{e}^z \tag{124}$$

Second harmonic The second harmonic terms of second order of ϵ for the divergence of the Euler equation (93) are:

$$-\frac{1}{2}u_{10}^2 + \frac{1}{2}\left(\frac{\partial w_{10}}{\partial z}\right)^2 + \mathrm{i}\frac{\partial u_{10}}{\partial z}w_{10} \;\;=\;\; 4p_{20} - \frac{\partial^2 p_{20}}{\partial z^2} \tag{125}$$

Using the results from first order (104, 106) gives:

$$0 \;\;=\;\; 4p_{20} - \frac{\partial^2 p_{20}}{\partial z^2} \tag{126}$$

which has the solution:

$$p_{20} \;\;=\;\; A_{20}\mathrm{e}^{2z} \tag{127}$$

The second harmonic terms of second order of ϵ in the dynamic surface equation (98) are:

$$p_{20}\big|_{z=0} - B_{20} + \frac{1}{2}B_{10}\frac{\partial p_{10}}{\partial z}\big|_{z=0} \;\;=\;\; 0 \tag{128}$$

Using the results from first order (102–103) and the solution for p_{20} (127) gives:

$$A_{20} \;\;=\;\; B_{20} - \frac{1}{2}B_{10}^2 \tag{129}$$

The second harmonic terms of second order of ϵ in the Euler equation and the kinematic surface equation (94–97) are respectively:

$$-\mathrm{i}u_{20} + \frac{\mathrm{i}}{4}u_{10}^2 + \frac{1}{4}w_{10}\frac{\partial u_{10}}{\partial z} \;\;=\;\; -ip_{20} \tag{130}$$

$$-\mathrm{i}v_{20} + \frac{\mathrm{i}}{4}u_{10}v_{10} + \frac{1}{4}w_{10}\frac{\partial v_{10}}{\partial z} \;\;=\;\; 0 \tag{131}$$

$$-\mathrm{i}w_{20} + \frac{\mathrm{i}}{4}u_{10}w_{10} + \frac{1}{4}w_{10}\frac{\partial w_{10}}{\partial z} \;\;=\;\; -\frac{1}{2}\frac{\partial p_{20}}{\partial z} \tag{132}$$

$$-\mathrm{i}B_{20} + \frac{\mathrm{i}}{4}u_{10}\big|_{z=0}B_{10} \;\;=\;\; \frac{1}{2}w_{20}\big|_{z=0} + \frac{1}{4}B_{10}\frac{\partial w_{10}}{\partial z}\big|_{z=0} \tag{133}$$

Using the results from first order (104–106) and the solution for p_{20} (127–129) gives:

$$u_{20} \;\;=\;\; v_{20} \;\;=\;\; w_{20} \;\;=\;\; p_{20} \;\;=\;\; 0 \tag{134}$$

$$B_{20} \;\;=\;\; \frac{1}{2}B_{10}^2 \tag{135}$$

3.2.3 Third order terms

First harmonic   The first harmonic terms of third order of ϵ for the divergence of the Euler equation (93) are:

$$u_{20}u_{10}^* + \frac{1}{2}\frac{\partial w_{20}}{\partial z}\frac{\partial w_{10}^*}{\partial z} - \frac{i}{2}\frac{\partial u_{20}}{\partial z}w_{10}^* + i\frac{\partial u_{10}^*}{\partial z}w_{20}$$

$$+iv_{11}\frac{\partial U}{\partial y} + \frac{\partial v_{10}}{\partial \bar{x}}\frac{\partial U}{\partial y} + \frac{\partial v_{10}}{\partial \bar{x}}\frac{\partial V}{\partial y} + iu_{10}\frac{\partial U}{\partial x}$$

$$= -\frac{1}{2}\frac{\partial^2 p_{10}}{\partial \bar{x}^2} - i\frac{\partial p_{11}}{\partial \bar{x}} + \frac{1}{2}p_{12} - \frac{1}{2}\frac{\partial^2 p_{10}}{\partial \bar{y}^2} - \frac{1}{2}\frac{\partial^2 p_{12}}{\partial z^2} \qquad (136)$$

Using the results from first and second order (102–106, 115–116, 123, 134) gives:

$$\begin{aligned}\frac{\partial^2 p_{12}}{\partial z^2} - p_{12} &= -2i\frac{\partial B_{11}}{\partial \bar{x}}e^z - \frac{\partial^2 B_{10}}{\partial \bar{x}^2}e^z - \frac{\partial^2 B_{10}}{\partial \bar{y}^2}e^z \\ &\quad -2\frac{\partial^2 B_{10}}{\partial \bar{x}^2}ze^z - 2iB_{10}\frac{\partial U}{\partial x}e^z - 2\frac{\partial B_{10}}{\partial \bar{y}}\frac{\partial U}{\partial y}e^z \qquad (137)\end{aligned}$$

which has the solution:

$$p_{12} = A_{12}(\bar{x}, \bar{y}, \bar{z}, \bar{t})e^z + \alpha(\bar{x}, \bar{y}, \bar{z}, \bar{t})ze^z + \beta(\bar{x}, \bar{y}, \bar{t})z^2 e^z \qquad (138)$$

where

$$\begin{aligned}\alpha &= -i\frac{\partial B_{11}}{\partial \bar{x}} - \frac{1}{2}\frac{\partial^2 B_{10}}{\partial \bar{y}^2} - iB_{10}\frac{\partial U}{\partial x} - \frac{\partial B_{10}}{\partial \bar{y}}\frac{\partial U}{\partial y} \\ \beta &= -\frac{1}{2}\frac{\partial^2 B_{10}}{\partial \bar{x}^2}\end{aligned}$$

The first harmonic terms of third order of ϵ in the dynamic surface equation (98) are:

$$\frac{1}{2}p_{12}\Big|_{z=0} - \frac{1}{2}B_{12} + \frac{1}{4}B_{20}\frac{\partial p_{10}^*}{\partial z}\Big|_{z=0} + \frac{1}{4}B_{10}^*\frac{\partial p_{20}}{\partial z}\Big|_{z=0} + \frac{1}{2}B_{10}\frac{\partial \bar{p}_1}{\partial z}\Big|_{z=0}$$

$$+\frac{1}{2}\zeta\frac{\partial p_{10}}{\partial z}\Big|_{z=0} + \frac{1}{16}B_{10}^2\frac{\partial^2 p_{10}^*}{\partial z^2}\Big|_{z=0} + \frac{1}{8}|B_{10}|^2\frac{\partial^2 p_{10}}{\partial z^2}\Big|_{z=0} = 0 \qquad (139)$$

Using the results from the first and second order (102–103, 109, 134–135) and the solution for p_{12} (138), gives:

$$A_{12} = B_{12} + \frac{3}{8}B_{10}^2 B_{10}^* - B_{10}\zeta \qquad\qquad \text{at } z = 0 \qquad (140)$$

27

The first harmonic terms of third order of ϵ in the Euler equation and the kinematic surface equation (94–97) are respectively:

$$\frac{1}{2}\frac{\partial u_{11}}{\partial \bar{t}} - \frac{\mathrm{i}}{2}u_{12} + \frac{1}{2}\frac{\partial u_{10}}{\partial \bar{x}}U + \frac{\mathrm{i}}{2}u_{11}U + \frac{1}{2}\frac{\partial u_{10}}{\partial \bar{y}}V + \frac{1}{2}v_{11}\frac{\partial U}{\partial y} - \frac{\mathrm{i}}{4}u_{20}u_{10}^*$$

$$+\frac{\mathrm{i}}{2}u_{10}^*u_{20} + \frac{1}{4}w_{20}\frac{\partial u_{10}^*}{\partial z} + \frac{1}{4}w_{10}^*\frac{\partial u_{20}}{\partial z} + \frac{1}{2}u_{10}\frac{\partial U}{\partial x}$$

$$= -\frac{1}{2}\frac{\partial p_{11}}{\partial \bar{x}} - \frac{\mathrm{i}}{2}p_{12} \tag{141}$$

$$\frac{1}{2}\frac{\partial v_{11}}{\partial \bar{t}} - \frac{\mathrm{i}}{2}v_{12} + \frac{1}{2}\frac{\partial v_{10}}{\partial \bar{x}}U + \frac{\mathrm{i}}{2}v_{11}U + \frac{1}{2}\frac{\partial v_{10}}{\partial \bar{y}}V + \frac{1}{2}v_{11}\frac{\partial V}{\partial y} + \frac{1}{2}u_{10}\frac{\partial V}{\partial x}$$

$$-\frac{\mathrm{i}}{4}u_{20}v_{10}^* + \frac{\mathrm{i}}{2}u_{10}^*v_{20} + \frac{1}{4}w_{20}\frac{\partial v_{10}^*}{\partial z} + \frac{1}{4}w_{10}^*\frac{\partial v_{20}}{\partial z} = -\frac{1}{2}\frac{\partial p_{11}}{\partial \bar{y}} \tag{142}$$

$$\frac{1}{2}\frac{\partial w_{11}}{\partial \bar{t}} - \frac{\mathrm{i}}{2}w_{12} + \frac{1}{2}\frac{\partial w_{10}}{\partial \bar{x}}U + \frac{\mathrm{i}}{2}w_{11}U + \frac{1}{2}\frac{\partial w_{10}}{\partial \bar{y}}V - \frac{\mathrm{i}}{4}u_{20}w_{10}^*$$

$$+\frac{\mathrm{i}}{2}u_{10}^*w_{20} + \frac{1}{4}w_{20}\frac{\partial w_{10}^*}{\partial z} + \frac{1}{4}w_{10}^*\frac{\partial w_{20}}{\partial z} = -\frac{1}{2}\frac{\partial p_{12}}{\partial z} \tag{143}$$

$$\frac{1}{2}\frac{\partial B_{11}}{\partial \bar{t}} - \frac{\mathrm{i}}{2}B_{12} - \frac{\mathrm{i}}{4}u_{20}\Big|_{z=0}B_{10}^* + \frac{\mathrm{i}}{2}u_{10}^*\Big|_{z=0}B_{20}$$

$$+\frac{1}{2}\frac{\partial B_{10}}{\partial \bar{x}}U + \frac{\mathrm{i}}{2}B_{11}U + \frac{1}{2}\frac{\partial B_{10}}{\partial \bar{y}}V + \frac{1}{2}v_{10}\Big|_{z=0}\frac{\partial \zeta}{\partial y}$$

$$-\frac{\mathrm{i}}{8}|B_{10}|^2\frac{\partial u_{10}}{\partial z}\Big|_{z=0} + \frac{\mathrm{i}}{8}B_{10}^2\frac{\partial u_{10}^*}{\partial z}\Big|_{z=0} + \frac{\mathrm{i}}{8}|B_{10}|^2\frac{\partial u_{10}}{\partial z}\Big|_{z=0}$$

$$= \frac{1}{2}w_{12}\Big|_{z=0} + \frac{1}{4}B_{20}\frac{\partial w_{10}^*}{\partial z}\Big|_{z=0} + \frac{1}{2}B_{10}^*\frac{\partial w_{20}}{\partial z}\Big|_{z=0} + \frac{1}{2}\zeta\frac{\partial w_{10}}{\partial z}\Big|_{z=0}$$

$$+\frac{1}{16}B_{10}^2\frac{\partial w_{10}^*}{\partial z}\Big|_{z=0} + \frac{1}{8}|B_{10}|^2\frac{\partial^2 w_{10}}{\partial z^2}\Big|_{z=0} \tag{144}$$

Combining these equations with the results from first and second order (104–106, 115–116, 122–124, 134–135) and the solution for p_{12} (138, 140) gives the space evolution of the current modified cubic Schrödinger equation, NLSC:

$$0 = \frac{\partial B_{11}}{\partial \bar{x}} + 2\frac{\partial B_{11}}{\partial \bar{t}} + \mathrm{i}\frac{\partial^2 B_{10}}{\partial \bar{t}^2} - \frac{\mathrm{i}}{2}\frac{\partial^2 B_{10}}{\partial \bar{y}^2} + \mathrm{i}B_{10}^2 B_{10}^* + 2\mathrm{i}B_{11}U$$

$$-6\frac{\partial B_{10}}{\partial \bar{t}}U - 5\mathrm{i}B_{10}U^2 + 2\frac{\partial B_{10}}{\partial \bar{y}}V + B_{10}\frac{\partial U}{\partial x} - \mathrm{i}\frac{\partial B_{10}}{\partial \bar{y}}\frac{\partial U}{\partial y} \tag{145}$$

And the time evolution:

$$0 = \frac{\partial B_{11}}{\partial \bar{t}} + \frac{1}{2}\frac{\partial B_{11}}{\partial \bar{x}} + \frac{\mathrm{i}}{8}\frac{\partial^2 B_{10}}{\partial \bar{x}^2} - \frac{\mathrm{i}}{4}\frac{\partial^2 B_{10}}{\partial \bar{y}^2} + \frac{\mathrm{i}}{2}B_{10}^2 B_{10}^*$$

$$+\mathrm{i}B_{11}U + \frac{\partial B_{10}}{\partial \bar{x}}U - \frac{\partial B_{10}}{\partial \bar{y}}V + \frac{1}{2}B_{10}\frac{\partial U}{\partial x} - \frac{i}{2}\frac{\partial B_{10}}{\partial \bar{y}}\frac{\partial U}{\partial y} \tag{146}$$

28

3.2.4 Summary

In the following $B = B_1$ to simplify the notation.

Space evolution   The space evolution of the current modified nonlinear Schrödinger equation which allows vorticity to the first order of ϵ, NLSC is:

$$\frac{\partial B}{\partial \bar{x}} = (\mathcal{L} + \mathcal{C} + \mathcal{N})B \qquad (147)$$

$\mathcal{L}$ contains the linear terms with constant coefficients. $\mathcal{C}$ contains the linear terms with variable coefficients. And $\mathcal{N}$ is the nonlinear term:

$$\mathcal{L} = -2\frac{\partial}{\partial \bar{t}} - i\frac{\partial^2}{\partial \bar{t}^2} + \frac{i}{2}\frac{\partial^2}{\partial \bar{y}^2}$$

$$\mathcal{C} = -2iU + 6U\frac{\partial}{\partial \bar{t}} + 5iU^2 - 2V\frac{\partial}{\partial \bar{y}} - \frac{\partial U}{\partial x} + i\frac{\partial U}{\partial y}\frac{\partial}{\partial \bar{y}}$$

$$\mathcal{N} = -i|B|^2$$

The vertical current component, W, the vertical derivatives of the current, $\frac{\partial \boldsymbol{V}}{\partial z}$, and the surface displacement, ζ, associated with the current, appear to the next order of the equation.

   The reconstruction formulas are:

$$\bar{\eta}, \bar{u}, \bar{v}, \bar{w} = 0$$

$$\bar{p} = -\frac{1}{2}|B|^2 e^{2z}$$

$$B_2 = \frac{1}{2}B^2$$

$$u_1 = Be^z + i\frac{\partial B}{\partial \bar{t}}e^z - BUe^z + 2i\frac{\partial B}{\partial \bar{t}}ze^z - 2BUze^z$$

$$v_1 = -i\frac{\partial B}{\partial \bar{y}}e^z$$

$$w_1 = -iBe^z + \frac{\partial B}{\partial \bar{t}}e^z + iBUe^z + 2\frac{\partial B}{\partial \bar{t}}ze^z + 2iBUze^z$$

$$p_1 = Be^z + 2i\frac{\partial B}{\partial \bar{t}}ze^z - 2BUze^z$$

$$u_2, v_2, w_2, p_2 = 0$$

Time evolution   The time evolution of the current modified nonlinear Schrödinger equation which allows vorticity to the first order of ϵ, NLSC is:

$$\frac{\partial B}{\partial \bar{t}} = (\mathcal{L} + \mathcal{C} + \mathcal{N})B \qquad (148)$$

where

$$\mathcal{L} = -\frac{1}{2}\frac{\partial}{\partial\bar{x}} - \frac{i}{8}\frac{\partial^2}{\partial\bar{x}^2} + \frac{i}{4}\frac{\partial^2}{\partial\bar{y}^2}$$

$$\mathcal{C} = -iU - U\frac{\partial}{\partial\bar{x}} + V\frac{\partial}{\partial\bar{y}} - \frac{1}{2}\frac{\partial U}{\partial x} + \frac{i}{2}\frac{\partial U}{\partial y}\frac{\partial}{\partial\bar{y}}$$

$$\mathcal{N} = -\frac{i}{2}|B|^2$$

The reconstruction formulas are:

$$\bar{\eta}, \bar{u}, \bar{v}, \bar{w} = 0$$

$$\bar{p} = -\frac{1}{2}|B|^2 e^{2z}$$

$$B_2 = \frac{1}{2}B^2$$

$$u_1 = Be^z - \frac{i}{2}\frac{\partial B}{\partial\bar{x}}e^z - i\frac{\partial B}{\partial\bar{x}}ze^z$$

$$v_1 = -i\frac{\partial B}{\partial\bar{y}}e^z$$

$$w_1 = -iBe^z - \frac{1}{2}\frac{\partial B}{\partial\bar{x}}e^z - \frac{\partial B}{\partial\bar{x}}ze^z$$

$$p_1 = Be^z - i\frac{\partial B}{\partial\bar{x}}ze^z$$

$$u_2, v_2, w_2, p_2 = 0$$

4 Numerical implementation

4.1 Numerical scheme

Space evolutions of current modified nonlinear Schrödinger equations, (76) and (147), may be written on the form:

$$\frac{\partial B}{\partial x} = (\mathcal{L} + \mathcal{V})B \qquad (149)$$

$\mathcal{L} = \mathcal{L}(\frac{\partial}{\partial t}, \frac{\partial}{\partial y})$ contains the linear terms with constant coefficients. $\mathcal{V} = \mathcal{N} + \mathcal{C}$ contains the nonlinear term, $\mathcal{N} = \mathcal{N}(|B|^2)$, and the linear terms with variable coefficients, $\mathcal{C} = \mathcal{C}(U, V, \frac{\partial}{\partial t}, \frac{\partial}{\partial y})$.

4.1.1 Splitting scheme

The formal solution of (149) is:

$$B = e^{F(x,y,t)}B_0 \qquad (150)$$

where $B_0 = B|_{x=0}$ and $\frac{\partial F(x,y,t)}{\partial x} = \mathcal{L}+\mathcal{V}$. If $F = F(x, y, t)$ is weakly depending on x, (150) may be approximated by:

$$B \approx \mathrm{e}^{(\mathcal{L}+\mathcal{V})x} B_0 \tag{151}$$

The exponential function may be expanded:

$$\mathrm{e}^{(\mathcal{L}+\mathcal{V})x} = 1 + (\mathcal{L} + \mathcal{V})x + \frac{1}{2}(\mathcal{L} + \mathcal{V})^2 x^2 + \frac{1}{6}(\mathcal{L} + \mathcal{V})^3 x^3 + \cdots \tag{152}$$

In numerical simulations $\mathcal{L}B$ and $\mathcal{V}B$ may be solved separately. The accuracy of the result depends on the splitting scheme. Note that it is not necessary with a more accurate splitting scheme than the accuracy of the separate solutions.

LV–split   With LV–split, $\mathrm{e}^{(\mathcal{L}+\mathcal{V})x} \approx \mathrm{e}^{\mathcal{L}x}\mathrm{e}^{\mathcal{V}x}$ which may be expanded to:

$$\mathrm{e}^{\mathcal{L}x}\mathrm{e}^{\mathcal{V}x} = 1 + (\mathcal{L} + \mathcal{V})\,x + \frac{1}{2}\left(\mathcal{L}^2 + 2\mathcal{L}\mathcal{V} + \mathcal{V}^2\right)x^2 + O(x^3) \tag{153}$$

The accuracy is of first order:

$$\mathrm{e}^{(\mathcal{L}+\mathcal{V})x} - \mathrm{e}^{\mathcal{L}x}\mathrm{e}^{\mathcal{V}x} = \frac{1}{2}(\mathcal{V}\mathcal{L} - \mathcal{L}\mathcal{V})x^2 + O(x^3) \tag{154}$$

Note that $\mathcal{V}\mathcal{L}$ do not equal $\mathcal{L}\mathcal{V}$ in all cases. An an appropriate commutator is defined by:

$$[\mathcal{V}, \mathcal{L}] \equiv \mathcal{V}\mathcal{L} - \mathcal{L}\mathcal{V} \tag{155}$$

so that (154) may be written on the form:

$$\mathrm{e}^{(\mathcal{L}+\mathcal{V})x} - \mathrm{e}^{\mathcal{L}x}\mathrm{e}^{\mathcal{V}x} = \frac{1}{2}[\mathcal{V}, \mathcal{L}]x^2 + O(x^3) \tag{156}$$

VLLV–split   With VLLV–split, $\mathrm{e}^{(\mathcal{L}+\mathcal{V})x} \approx \mathrm{e}^{\frac{1}{2}\mathcal{V}x}\mathrm{e}^{\mathcal{L}x}\mathrm{e}^{\frac{1}{2}\mathcal{V}x}$ which may be expanded to:

$$\mathrm{e}^{\frac{1}{2}\mathcal{V}x}\mathrm{e}^{\mathcal{L}x}\mathrm{e}^{\frac{1}{2}\mathcal{V}x} = 1 + (\mathcal{L} + \mathcal{V})x + \frac{1}{2}\left(\mathcal{L}^2 + \mathcal{L}\mathcal{V} + \mathcal{V}\mathcal{L} + \mathcal{V}^2\right)x^2$$
$$+ \left(\frac{1}{6}\mathcal{L}^3 + \frac{1}{4}\mathcal{L}^2\mathcal{V} + \frac{1}{8}\mathcal{L}\mathcal{V}^2 + \frac{1}{4}\mathcal{V}\mathcal{L}^2 + \frac{1}{4}\mathcal{V}\mathcal{L}\mathcal{V} + \frac{1}{8}\mathcal{V}^2\mathcal{L} + \frac{1}{6}\mathcal{V}^3\right)x^3$$
$$+ O(x^4) \tag{157}$$

This gives an accuracy of second order if $[\mathcal{V}, \mathcal{L}] \neq 0$:

$$\mathrm{e}^{(\mathcal{L}+\mathcal{V})x} - \mathrm{e}^{\frac{1}{2}\mathcal{V}x}\mathrm{e}^{\mathcal{L}x}\mathrm{e}^{\frac{1}{2}\mathcal{V}x} = \frac{1}{24}\left(2\big[\mathcal{L}, [\mathcal{V}, \mathcal{L}]\big] + \big[[\mathcal{V}, \mathcal{L}], \mathcal{V}\big]\right)x^3 + O(x^4) \tag{158}$$

(VLLV)³–split With (VLLV)³–splits, a fourth order scheme from Muslu & Erbay (2004) following McLachlan (1994) is used:

$$\mathrm{e}^{(\mathcal{L}+\mathcal{V})x} \approx \phi(\alpha x)\phi\big((1-2\alpha)x\big)\phi(\alpha x) \tag{159}$$

where $\phi(\chi) = \mathrm{e}^{\frac{1}{2}\mathcal{V}\chi}\mathrm{e}^{\mathcal{L}\chi}\mathrm{e}^{\frac{1}{2}\mathcal{V}\chi}$ and $\alpha = (2+2^{\frac{1}{3}}+2^{-\frac{1}{3}})/3$. This gives an accuracy of fourth order.

4.1.2 Fourier transform

Fourier transform is used to solved the linear part of (149) with constant coefficients:

$$\frac{\partial B}{\partial x} = \mathcal{L}B \tag{160}$$

The Fourier transform of (160) with respect to y and t is:

$$\frac{\partial \widehat{B}}{\partial x} = \widehat{\mathcal{L}}\widehat{B} \tag{161}$$

where $\widehat{L}$ is a complex polynomial of k_y and ω. Note that $\widehat{\frac{\partial B}{\partial y}} = ik_y\widehat{B}$ and $\widehat{\frac{\partial B}{\partial t}} = -i\omega\widehat{B}$. The exact solution of (160) is:

$$\widehat{B} = \mathrm{e}^{\widehat{\mathcal{L}}x}\widehat{B}_0 \tag{162}$$

where $\widehat{B}_0 = \widehat{B}|_{x=0}$.

The Fourier transform with respect to y and t is given by:

$$\hat{B}_{ij} = \frac{1}{MN}\sum_{m=0}^{M-1}\sum_{n=0}^{N-1} B_{mn}e^{\mathrm{i}(\Omega_j t_n - k_{yi}y_m)} \tag{163}$$

where $y_m = m\Delta y$, $t_n = n\Delta t$, $k_{yi} = i\Delta k_y$, and $\Omega_j = j\Delta\omega$.

4.1.3 Finite Difference

Runge–Kutta schemes are used to solve the nonlinear part and the linear part with variable coefficients in (149):

$$\frac{\partial B}{\partial x} = \mathcal{V}B \tag{164}$$

The Runge–Kutta scheme used ought to be of the same order as the splitting scheme.

Alternative:	a	b	α	β
A	0	1	1/2	1/2
B	1/2	1/2	1	1
C	2/3	1/3	3/2	3/2
D	1/3	2/3	3/4	3/4

Table 2: *The four alternative choices for the variables in the second order Runge–Kutta scheme.*

First order A first order Euler scheme is used for the first order splitting scheme:

$$B_{x+\triangle x} \;=\; B_x + \triangle x \mathcal{V}_x B_x \tag{165}$$

Second order A second order Runge–Kutta scheme is used for the second order splitting scheme:

$$B_{x+\triangle x} \;=\; B_x + \triangle x(ak_1 + bk_2) \tag{166}$$

where

$$
\begin{aligned}
k_1 &= \mathcal{V}_x B_x \\
k_2 &= \mathcal{V}_{x+\alpha x}(B_x + \beta \triangle x k_1)
\end{aligned}
$$

The four coefficients, a, b, α, and β, have to satisfy the following three equations:

$$a + b = 1, \qquad \alpha b = \frac{1}{2}, \qquad \beta b = \frac{1}{2} \tag{167}$$

The four alternatives in table 2 is studied. Lo & Mei (1985) used alternative A. Alternative B gives the modified Euler scheme.

Fourth order The most used set of variables on the fourth order Runge–Kutta (Gerald & Wheatley, 1994) is used with the fourth order splitting scheme:

$$B_{x+\triangle x} = B_x + \frac{1}{6}\triangle x \left(k_1 + 2k_2 + 2k_3 + k_4\right) \tag{168}$$

where

$$k_1 \;=\; \mathcal{V}_x B_x$$

$$k_2 = \mathcal{V}_{x+\frac{1}{2}\triangle x}\left(B_x + \frac{1}{2}\triangle x k_1\right)$$
$$k_3 = \mathcal{V}_{x+\frac{1}{2}\triangle x}\left(B_x + \frac{1}{2}\triangle x k_2\right)$$
$$k_4 = \mathcal{V}_{x+\triangle x}\left(B_x + \triangle x k_3\right)$$

4.2 Model setup

The space evolution of the current modified nonlinear cubic Schrödinger equation which allows vorticity, NLSC, (147), is simulated. Test simulations are performed in order to study the effect of the different terms (see section 5.3).

The length of the time series are $T = 2000$. Using $N = 1024$ nodes, the time step is $\Delta t = \frac{T}{N} \approx 1.95$ and $\triangle\omega = \frac{2\pi}{T} \approx 0.0031$. The width of the simulation area, $y = [-20, 20]$, with 16 nodes, gives $\triangle y = 2.5$ and $\triangle k_y \approx 0.079$. Test simulations are performed with different widths (see section 5.2).

4.2.1 Incoming waves

Unidirectional incoming waves with initial Gaussian spectrum have been studied. The Fourier amplitudes at $x = 0$ are given by:

$$\hat{B}_j = \epsilon\sqrt{\frac{\triangle\omega}{\sqrt{2\pi}\sigma_\omega}}\mathrm{e}^{-\frac{\Omega_j^2}{4\sigma_\omega^2}+\mathrm{i}\psi_j} \tag{169}$$

The frequency is given by $\omega_j = 1 + \Omega_j$. The phases, $\psi_{i,j}$, are statistically independent and uniformly distributed on the interval $[0, 2\pi)$. We have chosen $\epsilon = 0.1$. $\sigma_\omega = 0.1$ is the bandwidth in Fourier space.

Test simulations with an incoming Stokes wave are also performed (see sections 5.2 and 5.4).

4.2.2 Current field

The NLSC equation may be used for a large range of prescribed currents. Here we have chosen two types; a surface current jet given by:

$$U = \begin{cases} 0 & \text{when } x \leq X \text{ and/or } |y| \geq Y \\ U_0 \sin^2\left(\frac{\pi}{2\triangle X}(x-X)\right)\cos^2\left(\frac{\pi y}{2Y}\right) & \text{when } x > X \text{ and } x < X + \triangle X \\ U_0 \cos^2\left(\frac{\pi y}{2Y}\right) & \text{when } x \geq X + \triangle X \end{cases} \tag{170}$$

and a transversally uniform current given by:

$$U = \begin{cases} 0 & \text{when } x \leq X \\ U_0 \sin^2\left(\frac{\pi}{2\triangle X}(x-X)\right) & \text{when } x > X \text{ and } x < X + \triangle X \text{ (171)} \\ U_0 & \text{when } x \geq X + \triangle X \end{cases}$$

The wave field is allowed about 32 wavelengths, $x = [0, X)$ where $X = 200$, to develop before the waves encounter a current. $Y = 10$ is half the width of the jet. And $\triangle X = 100$ is the current build–up length. Test simulations with different build–up lengths and widths of the jet are performed (see sections 5.7 and 5.6).

We have studied three current cases: no current, co–current with $U_0 = 0.05$, and opposing current with $U_0 = -0.05$ which is not enough to reflect the waves, but sufficient to study the characteristic features of opposing currents. Test simulations are performed with other current strengths (see section 5.5).

Simulations and observations of tidal currents suggest that establishing current jets are more fanned in than terminating current jets are fanned out (Hjelmervik *et al.*, 2005, 2008). Test simulations show that the current across the jet, V, needed to satisfy the continuity equation, has negligible impact on the results and may thus be set to zero in the NLSC equation (see section 5.4). Alternatively, the continuity equation can be satisfied by a vertical current, W, which does not appear within the truncation level of the NLSC equation.

4.3 Numerical order

Here the order of different schemes with and without currents is studied.

4.3.1 Transversally uniform currents

The transversally uniform current is given by (171) with $U_0 = 0$, 0.05, and -0.05. The incoming waves are unidirectional and given by (169). The incoming phase is randomised in the same way in all simulations. The distributions of η and $|B|$ at $x = 0$ are shown in figure 4.

Time series of the envelope, B, at $x = 900$ from simulation j is used to calculate the error:

$$E_j = |B|_j - |B|_{ref} \qquad (172)$$

The results with the smallest step, $\triangle x = 0.001$, is used as the reference solution. Simulations which broke down earlier than $x = 900$, are not considered.
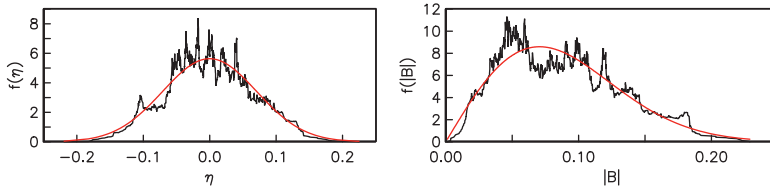
Figure 4: *The distributions of surface elevation, η, (left) and envelope, |B|, (right) at x = 0 compared to a Gaussian and a Rayleigh distribution (smooth line) respectively.*

The errors, L_1 and L_2, are calculated from the following formulas:

$$L_1 = ||E_j||_1 = \int_{-\infty}^{\infty} |E_j| \mathrm{d}t \tag{173}$$

$$L_2 = ||E_j||_2 = \sqrt[2]{\int_{-\infty}^{\infty} E_j^2 \mathrm{d}t} \tag{174}$$

The simulations are of the expected order both with and without currents (figure 5). The four alternatives in table 2 give slightly different convergence rate (figure 6a).

4.3.2 Current jets

The current jet is given by (170) with $U_0 = 0$, 0.05, and -0.05. The incoming waves are unidirectional and given by (169). The incoming phase is randomised in the same way in all simulations. The distributions of η and $|B|$ at $x = 0$ are shown in figure 4.

Time series of the envelope, B, for all values of y at $x = 400$ from simulation j is used to calculate the error:

$$E_j = |B|_j - |B|_{ref} \tag{175}$$

The results with the smallest step, $\triangle x = 0.001$, used as a reference solution. Simulations which broke down earlier than $x = 400$, are not considered.

L_1 and L_2 are calculated from the following formulas:

$$L_1 = ||E_j||_1 = \int_{-\infty}^{\infty} \int_{-\infty}^{\infty} |E_j| \mathrm{d}y \, \mathrm{d}t \tag{176}$$

$$L_2 = ||E_j||_2 = \sqrt[2]{\int_{-\infty}^{\infty} \int_{-\infty}^{\infty} E_j^2 \mathrm{d}y \, \mathrm{d}t} \tag{177}$$

The simulations are of the expected order both with and without current for first and second order schemes (figure 7a). The four alternatives in table 2 give slightly different convergence rate (figure 6b).

36

Without any current, the simulations are of fourth order when the fourth order scheme is used (figure 7b). The current depends on x and this is probably the reason why the simulations with current diverge from fourth order when the fourth order scheme is used. The function, $F = F(x, y, t)$ in (150) might therefore be better approximated by:

$$F(x, y, t) \;=\; (\mathcal{L} + \mathcal{V})_0 x + \frac{1}{2} \left(\frac{\partial \mathcal{V}}{\partial U} \frac{\partial U}{\partial x} + \frac{\partial \mathcal{V}}{\partial V} \frac{\partial V}{\partial x} \right)_0 x^2 + \cdots \qquad (178)$$

New splitting schemes have to be constructed in order to improve the fourth order scheme.

In the following, the second order scheme with alternative A and an integrating step of $\triangle x = 0.2$ is used.
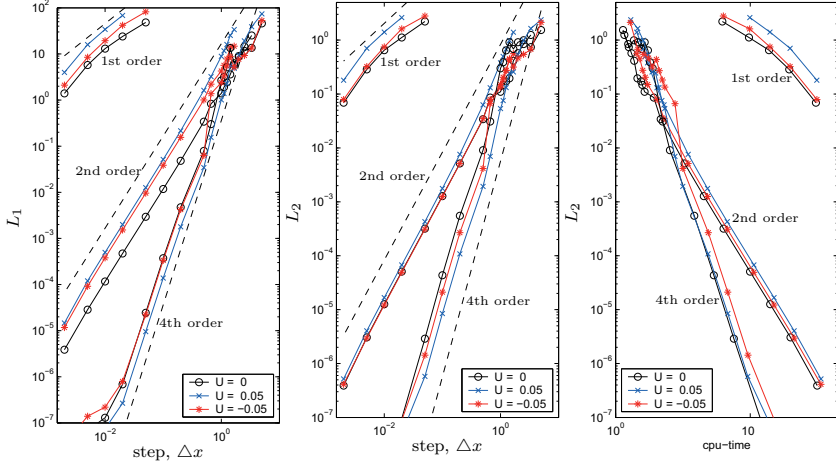
Figure 5: *The L_1 (left) and L_2 (middle) errors as a function of integrating step, $\triangle x$, and the L_2 errors as a function of cpu–time (right) for simulations with unidirectional incoming waves on transversally uniform currents. The dotted lines represent 1st, 2nd, and 4th order respectively.*
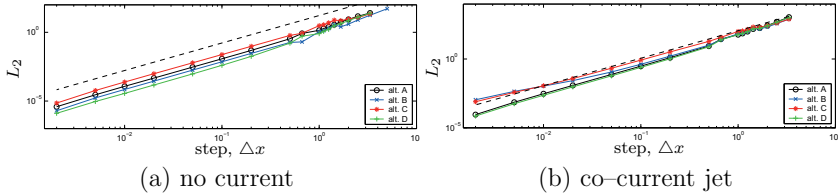
Figure 6: *The L_2 errors for the four alternative second order schemes. The dotted lines represent 2nd order.*
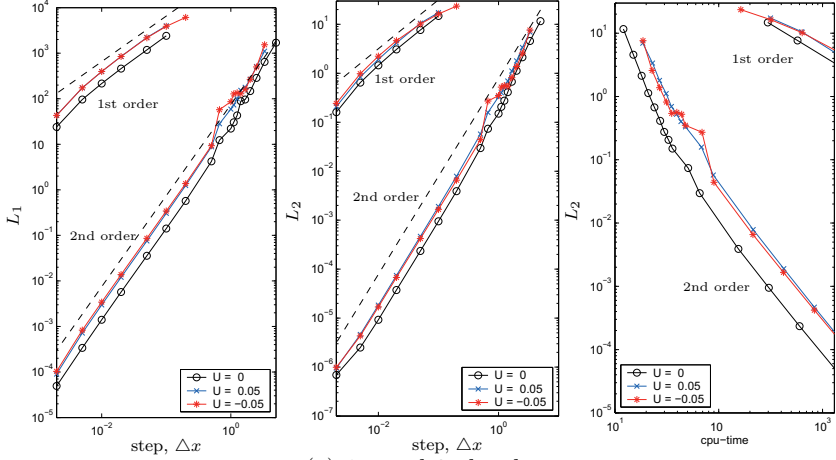
(a) 1st and 2nd order
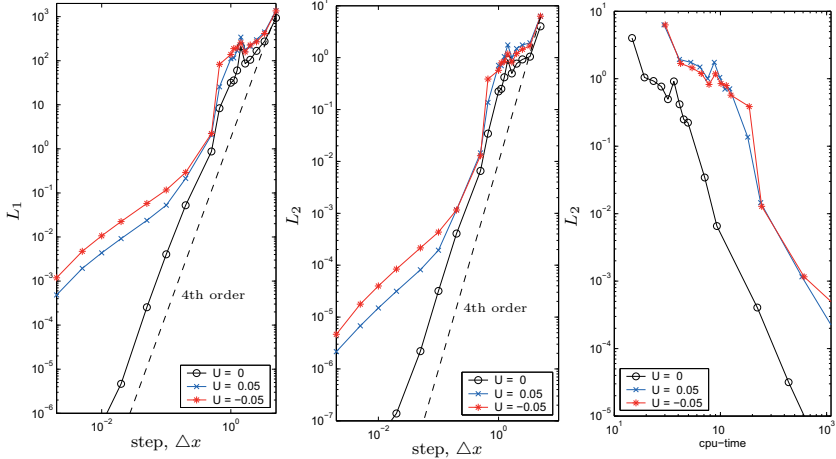
(b) 4th order

Figure 7: *The L_1 (left) and L_2 (middle) errors as a function of integrating step, $\triangle x$, and the L_2 errors as a function of cpu–time (right) for simulations with unidirectional incoming waves on current jets. The dotted lines represent 1st, 2nd, and 4th order respectively.*

39

5   Numerical results

A few results from simulations with the space evolution of the NLSC equation which allows vorticity, (147), will be presented. More results are published in Hjelmervik & Trulsen (2009).

The reconstruction of the surface elevation according to section 3.2, is given by:

$$\eta = \frac{1}{2}\left(Be^{i(x-t)} + \frac{1}{2}\epsilon B^2 e^{2i(x-t)} + c.c.\right) + O(\epsilon^2) \tag{179}$$

As pointed out by Tayfun (1980) and others the second harmonic terms introduce a vertical asymmetry to the profile caused by the first harmonic terms. The crest become narrower and sharper and throughs become longer and shallower as illustrated in figure 8. Since both the envelope of the crest and the envelope of the through are displaced upward by the second harmonic terms, the distribution of wave heights remain the same. The mean value of the highest third of the wave heights – traditionally used as the significant wave height – also remains the same. The more modern definition of the significant wave height – four times the standard deviation of the surface elevation – is affected, but the change is negligible.
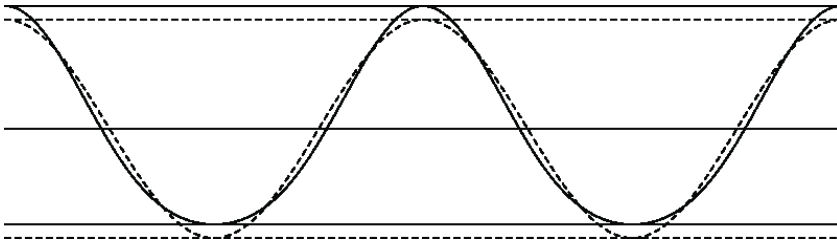
Figure 8: *An illustrative reconstruction of the surface elevation and the corresponding envelopes for fixed x or t. The dotted lines represent the first order reconstruction of (179) with $B = 0.5$. The solid lines represent the second order reconstruction which causes the crests to become narrower and sharper and the throughs to become longer and shallower. The wave heights remain unchanged.*

The first order reconstruction of the surface displacement is used to calculate both the significant wave height, H_s, and the kurtosis, κ, of the surface displacement:

$$H_s(x,y) = 4\sqrt{\overline{\eta^2}} = 4\sqrt{\frac{1}{2}\overline{|B|^2}} \tag{180}$$

40

$$\kappa(x,y) \quad = \quad \frac{\overline{\eta^4}}{\overline{\eta^2}^2} \quad = \quad \frac{3}{2} \frac{\overline{|B|^4}}{\overline{|B|^2}^2} \tag{181}$$

The bar represents combined time and ensemble averaging. The kurtosis equals three when the surface elevation is Gaussian distributed.

When the waves meet an opposing current, the wave height increases in the centre of the jet, and decreases at the sides of the jet. When the waves meet an co–current, the wave height decreases in the centre of the jet, and increases at the sides of the jet. The following sections show how these changes depend on the number of simulations in an ensemble (sec. 5.1), the width of the simulation area (sec. 5.2), the different terms in the NLSC equation (sec. 5.3), the transversal current (sec. 5.4), the current strength (sec. 5.5), the width of the jet (sec: 5.6), and the current build–up length (sec. 5.7).
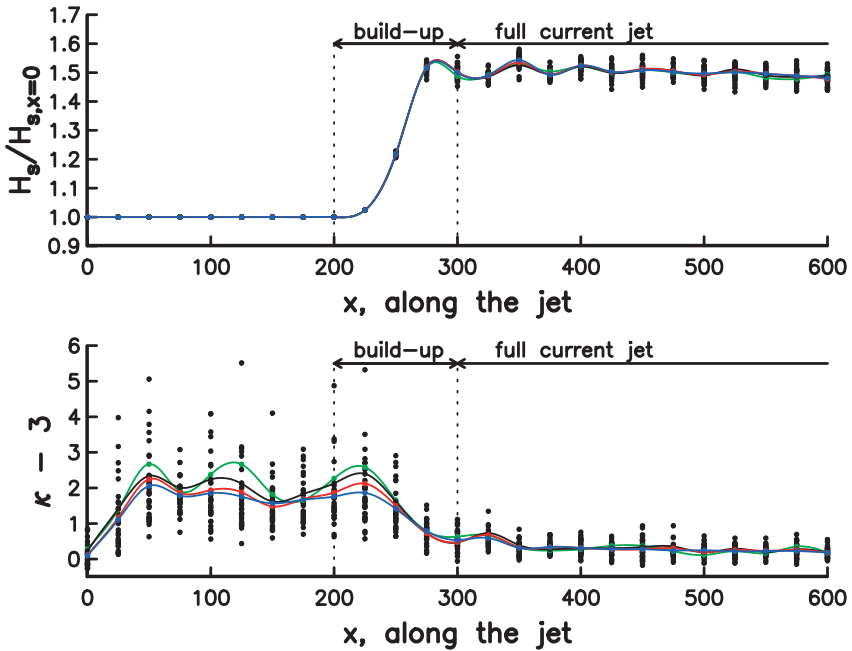
Figure 9: *The significant wave height (upper) and kurtosis (lower) from 30 single simulations (dots) and from ensembles consisting of 5 (green), 10 (black), 20 (red), and 30 (blue) simulations.*

5.1 Number of simulations in an ensemble

In order to assure statistical and numerical convergence a sufficient number of simulations should be included. Test simulations are performed with incoming unidirectional waves (169), and opposing current jet (170) with $U_0 = -0.05$.

More simulations are needed in order to calculate the kurtosis than the significant wave height (figure 9). If only the significant wave height and similar qualities are wanted, 10 simulations are sufficient. In the following we have used 30 simulations in each ensemble in order to get a more reliable result also for properties as the kurtosis.

5.2 Width of the simulation area

Test simulations are performed with different widths of the simulation area. The current jet is kept narrow ($|y| < 10$). The incoming wave is a Stokes wave. Simulations are performed with both a co–current with $U_0 = 0.05$ and an opposing current jet with $U_0 = -0.05$.

When the waves encounter a co–current jet, the amplitudes decrease in the centre of the jet and increase at the sides of the jet. The high amplitudes created at the sides of the jet, propagate away from the jet towards the simulation borders and seem to be reflected there (figure 10). When the width of the simulation area is $|y| < 40$, the high amplitudes are not reflected before $x = 375$. The amplitude in the centre of the jet seems to be periodic with a length that depends on the width of the simulation area.

When the waves encounter an opposing current jet, the amplitudes increase in the centre of the jet and decrease at the sides of the jet. The amplitude of the waves are affected only in a narrow area limited by the current jet (figure 11). The amplitude in the centre of the jet seems to be periodic with a length that does not depend on the width of the simulation area as long as the simulation area is wider than the width of the jet.

The fact that the waves converge and diverge when encountering currents, makes it possible to create very beautiful plots of the surface elevation. Heller (2005) published an art plot in an electronic art and animation catalog.
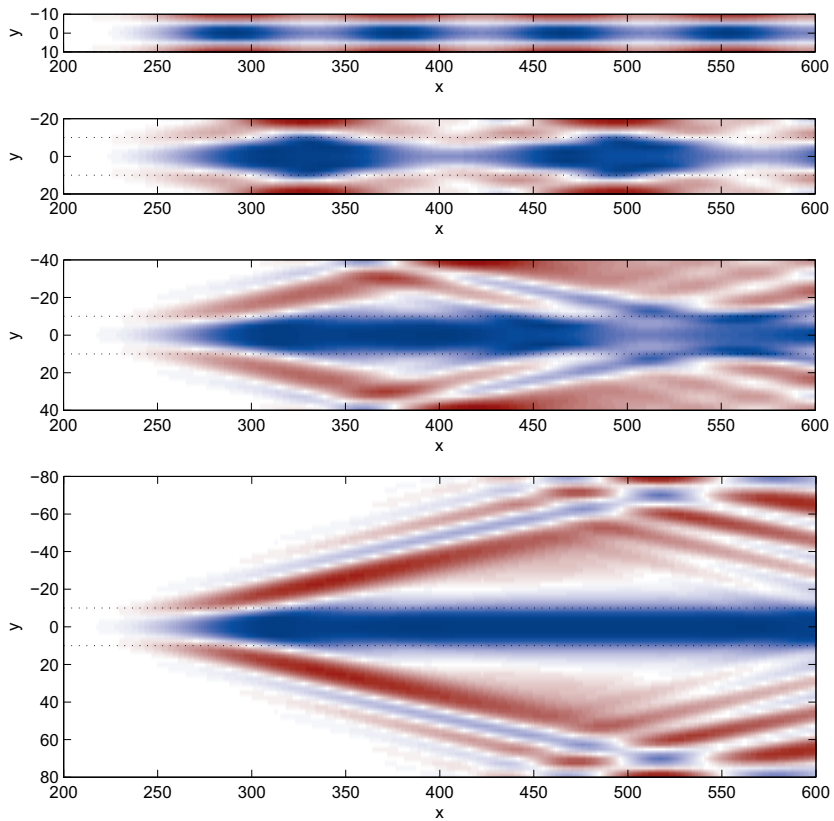
Figure 10: $|B|$ on a co–current when $y < 10$ (upper), $|y| < 20$, $|y| < 40$, and $|y| < 80$ (lower). Nonlinear. Red is high values, blue small. The dotted lines mark the region of the jet.
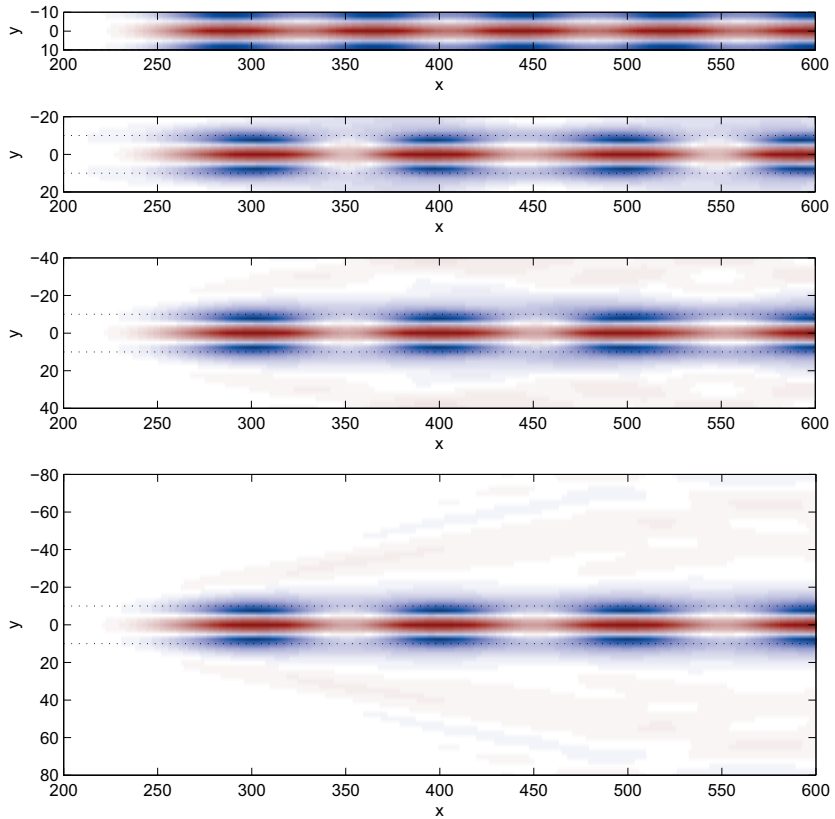
Figure 11: $|B|$ on a counter current when $y < 10$ (upper), $|y| < 20$, $|y| < 40$, and $|y| < 80$ (lower). Nonlinear. Red is high values, blue small. The dotted lines mark the region of the jet.

5.3 Current terms

To study the effect of the different current terms, the NLSC equation which allows vorticity (147) is simulated without one term at the time. For comparison, also the nonlinear term is left out. The simulations are performed both with a co–current and a counter current jet (170). The simulation area is given by $|y| < 20$. The incoming waves are unidirectional (169). The result for significant wave height and kurtosis is shown in figure 12 and 13.
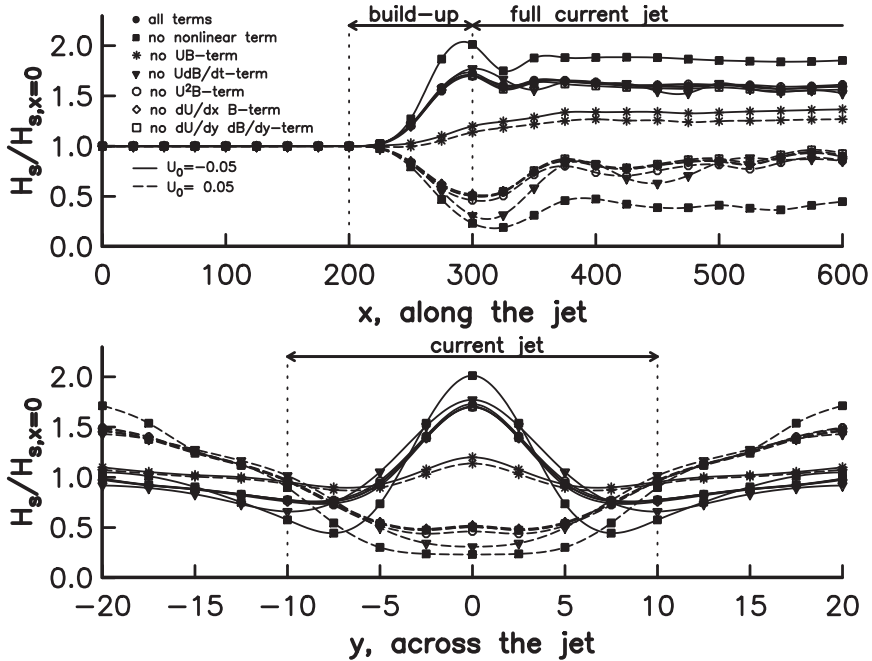
Figure 12: *The significant wave height in the centre of the jet (upper) and across the jet at x = 300 (lower) for unidirectional incoming waves when one term at the time is left out in the simulations.*

In linear simulations the variation in significant wave height is larger than in nonlinear simulations, and the kurtosis is close to three. Among the current terms, the UB–term has the largest impact on the results. This is not surprising since it is of lower order than the rest of the current terms. The UB–term is responsible for most of the refraction. The $U\frac{\partial B}{\partial t}$ has small impact on the significant wave height, but decreases the variation in kurtosis.
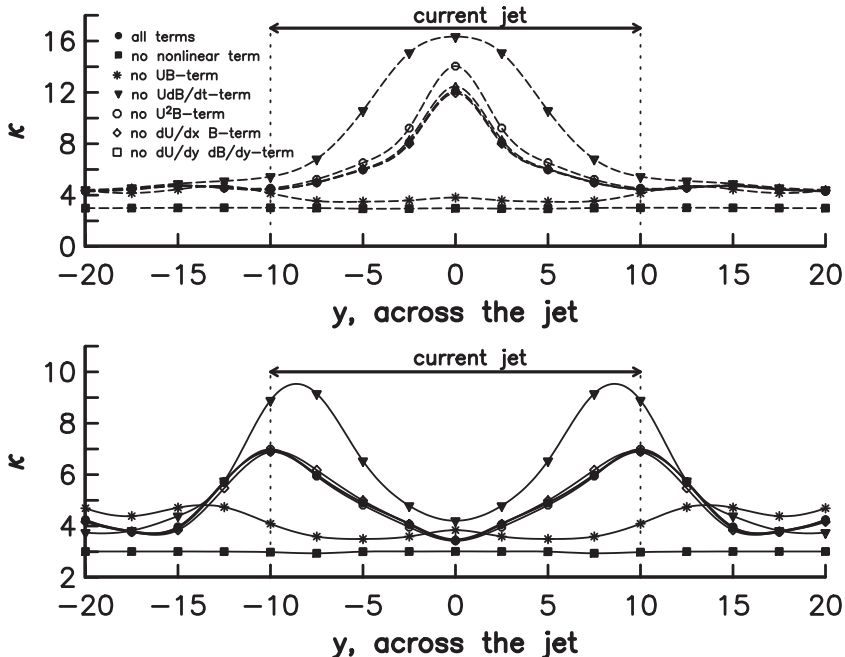
45

Figure 13: *The kurtosis across a co–current (upper) and counter current (lower) jet at x = 300 for unidirectional incoming waves when one term at the time is left out in the simulations.*

Note that the terms that do not appear in the current modified nonlinear Schrödinger equation built on potential theory, the $\frac{\partial U}{\partial y}\frac{\partial B}{\partial y}$–term and the $\frac{\partial U}{\partial x}B$–term, have small impact on the results. The U^2B–term also has minor impact. With a stronger current, these terms may have a stronger effect.

In this case, a good approximation for the NLSC equation is the simplified NLSC equation given by:

$$\frac{\partial B}{\partial x} + 2\frac{\partial B}{\partial t} + \mathrm{i}\frac{\partial^2 B}{\partial t^2} - \frac{\mathrm{i}}{2}\frac{\partial^2 B}{\partial y^2} + 2\mathrm{i}UB - 6U\frac{\partial B}{\partial t} + \mathrm{i}|B|^2 B = 0 \qquad (182)$$

Note that in Hjelmervik & Trulsen (2009) we used a different scaling of the modulation of the current normal to the principal propagation direction of the waves. This causes the $\frac{\partial U}{\partial y}\frac{\partial B}{\partial y}$–term to be left out to the truncation level of the NLSC equation.

5.4   Transversal current, V

The continuity equation for the current has to be satisfied:

$$\frac{\partial U}{\partial x} + \frac{\partial V}{\partial y} + \frac{\partial W}{\partial z} \;=\; 0 \tag{183}$$

During the build–up of the longitudinal current given by (170) or (171), the first term in (183) is not zero. If both the transversal current, V, and the vertical current, W, is set to zero, (183) is therefore not satisfied. Here two alternatives for the current jet is discussed. The transversally uniform current is not considered.

	$x{<}X$	$X < x < X + \triangle X$	$x > X + \triangle X$
$y{>}Y$	$U{=}0$ $W{=}0$	$U{=}0$ $W{=}0$	$U{=}0$ $W{=}0$
$|y|{<}Y$	$U{=}0$ $W{=}0$	$U{=}U_0 \sin^2\!\left(\frac{\pi}{2\triangle X}(x-X)\right)\cos^2\!\left(\frac{\pi y}{2Y}\right)\mathrm{e}^{-\alpha\pi z}$ $W{=}{-}U_0\frac{1}{2\alpha\triangle X}\sin\!\left(\frac{\pi}{\triangle X}(x-X)\right)\cos^2\!\left(\frac{\pi y}{2Y}\right)\mathrm{e}^{-\alpha\pi z}$	$U{=}U_0\cos^2\!\left(\frac{\pi y}{2Y}\right)$ $W{=}0$
$y{<}{-}Y$	$U{=}0$ $W{=}0$	$U{=}0$ $W{=}0$	$U{=}0$ $W{=}0$

Table 3: *A possible current jet when $V = 0$.*

	$x{<}X$	$X < x < X + \triangle X$	$x > X + \triangle X$
$y{>}Y$	$U{=}0$ $V{=}0$	$U{=}0$ $V{=}{-}U_0\frac{\pi Y}{4\triangle X}\sin\!\left(\frac{\pi}{\triangle X}(x-X)\right)$	$U{=}0$ $V{=}0$
$|y|{<}Y$	$U{=}0$ $V{=}0$	$U{=}U_0\sin^2\!\left(\frac{\pi}{2\triangle X}(x-X)\right)\cos^2\!\left(\frac{\pi y}{2Y}\right)$ $V{=}{-}U_0\frac{Y}{4\triangle X}\sin\!\left(\frac{\pi}{\triangle X}(x-X)\right)\left(\cos\!\left(\frac{\pi y}{Y}\right)+\frac{\pi y}{Y}\right)$	$U{=}U_0\cos^2\!\left(\frac{\pi y}{2Y}\right)$ $V{=}0$
$y{<}{-}Y$	$U{=}0$ $V{=}0$	$U{=}0$ $V{=}U_0\frac{\pi Y}{4\triangle X}\sin\!\left(\frac{\pi}{\triangle X}(x-X)\right)$	$U{=}0$ $V{=}0$

Table 4: *A possible current jet when $W = 0$.*

At one extreme, the transversal current is set to zero. A possible current jet is then given in table 3. The parameter α tells how quickly the current decrease towards the bottom. If the scaling in section 3.1 or 3.2 is applied, α has to be less than 0.05. The vertical current first appears in the current modified Schrödinger equation to Dysthe level, and is not implemented in numerical models for cubic Schrödinger equations.

At the other extreme, the vertical current is set to zero. A possible current jet is then given in table 4. A few simulations are performed with the current

jet given in table 4. The incoming wave is a Stokes wave. Both linear and nonlinear simulations are performed with both a co–current with $U_0 = 0.05$ and an opposing current with $U_0 = -0.05$. The results are compared with results from simulations with $V = 0$. The transversal current has little effect in all simulations. The effect on the envelope is shown in figures 14–15.

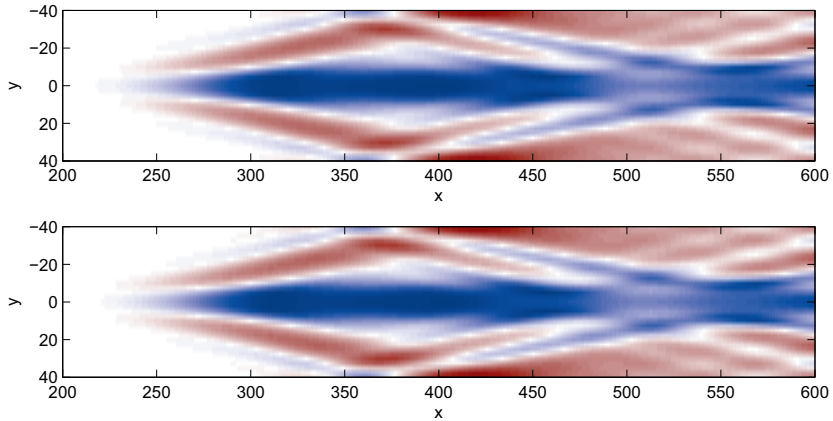To assume that both the vertical and the transversal currents equal zero, seems to be a good approximation in this case.

Figure 14: $|B|$ on a co–current with $V = 0$ (upper) and $V \neq 0$ (lower). High values are red, small values are blue.
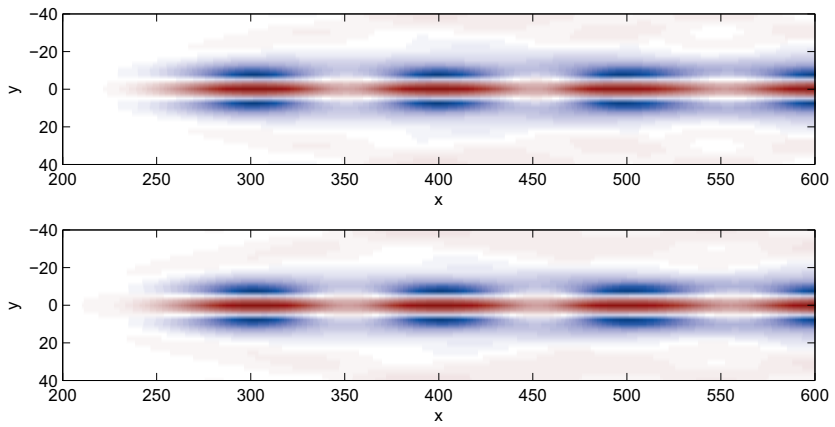
Figure 15: $|B|$ *on a counter current with* $V = 0$ *(upper) and* $V \neq 0$ *(lower). High values are red, small values are blue.*

49

5.5 Current strength

Test simulations are performed with different strengths of the current jet, (170). The simulation area is given by $|y| < 20$ The incoming waves are unidirectional (169).

The significant wave height in the centre of the jet increases with increasing strength of the opposing current jet, and decreases with increasing strength of the co-current (figure 16). The significant wave height seems to oscillate with a period depending on the strength of the current jet.

Note that in the derivation of the Schrödinger equations, U_0 is assumed of order ϵ. The spectrum is not narrow banded when $|U_0| = 0.25$, and the simulations seem to break down when $|U_0| > 0.25$. On counter currents this may be due to longitudinal refraction. When $\mathbf{U} = U(x)\mathbf{i}$ the dimensionless stopping velocity is $U = -\frac{1}{4}$ according to (7) and linear ray theory (Peregrine & Smith, 1979).
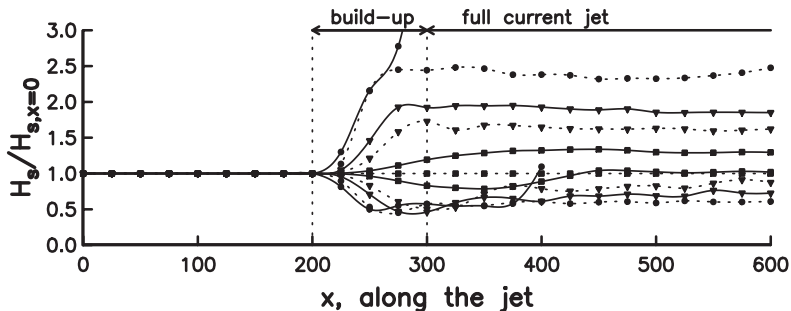

Figure 16: *The significant wave height of waves in the centre of current jets with different strengths: $|U_0| = 0$ (square, dotted), 0.01 (square, solid), 0.05 (triangle, dotted), 0.10 (triangle, solid), 0.25 (disk, dotted), and 0.50 (disk, solid).*

5.6 Width of the jet

Test simulations are performed with different widths, Y, of the current jet (170). The simulation area is given by $|y| < 40$ The incoming waves are unidirectional (169). Simulations are performed with both a co–current and an opposing current jet.

The significant wave height along the centre of the jet and across the jet changes more slowly the wider the jet is (figure 17). On an opposing current jet, the significant wave height does not depend on the width of the jet when

the waves are adjusted to the current jet. When the width of the jet equals the width of the simulation area, oscillations occur due to channel effects.
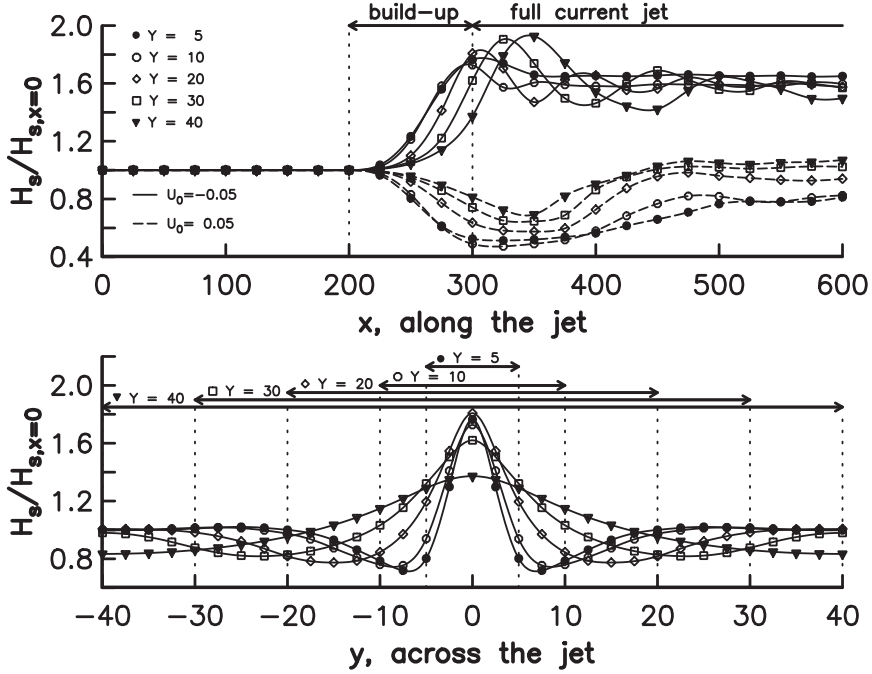

Figure 17: *The significant wave height in the centre of a co–current and a counter current jet (upper) and across a counter current jet at x=300 (lower) with different widths of the jet.*

5.7 Build–up length

Test simulations are performed with different build–up lengths, $\triangle X$, of the current jet, (170). The simulation area is given by $|y| < 40$ The incoming waves are unidirectional (169).

Both the significant wave height and the kurtosis in the centre of the jet change quicker with shorter build–up lengths (figure 18). On opposing current jets the significant wave height seems to oscillate more with shorter build–up lengths, but stabilises around the same value after the build–up independent of the build–up length. The kurtosis decreases more quickly with shorter build–up lengths of opposing jets. On co–current jets channel

effects are more pronounced for shorter build–up lengths due to a stronger divergence during the build–up. The kurtosis increases quicker and reaches a larger maximum with shorter build–up lengths of the co–current.
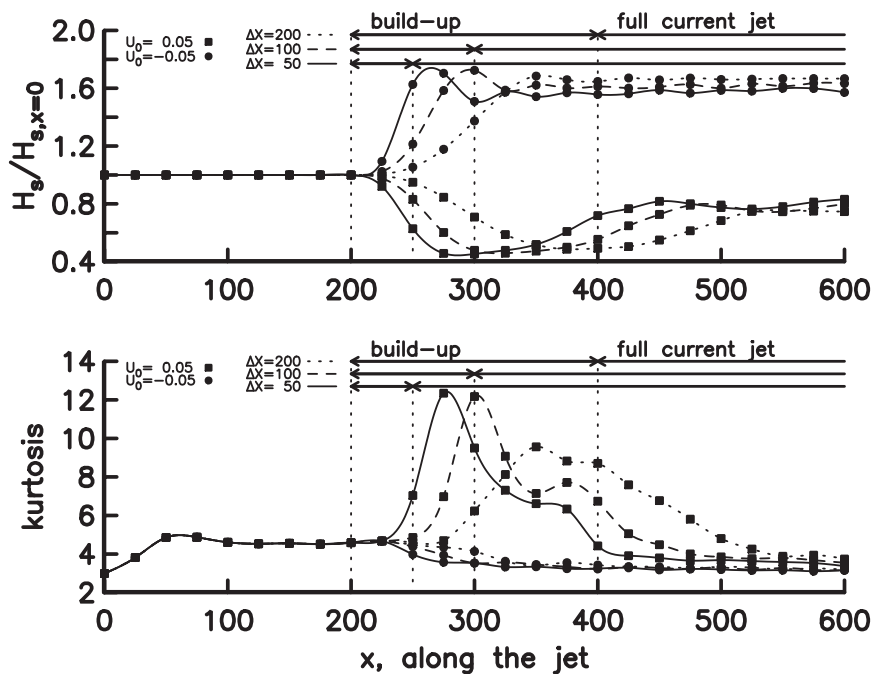

Figure 18: *The significant wave height (upper) and kurtosis (lower) of waves in the centre of current jets with different build–up lengths.*

6   Conclusion

Two new current modified Schrödinger equations have been derived; one using potential theory, and one allowing vorticity (NLSC). The splitting schemes are described and the corresponding numerical orders tested. Since the current is inhomogeneous, new fourth order splitting schemes should be constructed.

Monte–Carlo simulations are performed to estimate statistical wave properties. 30 simulations in each ensemble is found to be sufficient to assure statistical and numerical convergence for higher order properties as the kurtosis. Different model setups are studied. When waves encounter a counter current, the simulation area should be wider than twice the width of the jet.

To study the effect of each current term in the NLSC equation, simulations are performed without one term at the time. It is found that the current term to linear order contains most of the refraction. The nonlinear term has larger impact than the rest of the current terms. The contribution from the transversal current required to satisfy the continuity equation for the current, is shown to be negligible for waves on collinear jets.

The statistical wave properties are also used to illustrate different current jet configurations. If the strength of the counter current jet is increased, the wave height increases and seems to oscillate with a period depending on the strength of the jet. After the waves are adjusted to a counter current, the significant wave height does not seem to depend on neither the width nor the build–up length of the jet.

The current modified Schrödinger equation and model setup presented here are expected to have a large range of application possibilities. The occurrence of freak waves on collinear currents is discussed in Hjelmervik & Trulsen (2009).

Here only collinear currents are studied. The transversal current is assumed at the same strength as the longitudinal current in the derivation of the current modified nonlinear Schrödinger equation which allows vorticity. Thereby the equation may be used for oblique waves on current jets.

The current modified nonlinear Schrödinger equation for potential currents is derived to Dysthe level. It can easily be implemented in the numerical model. And the results are expected to be interesting. Schrödinger equations to Dysthe level are known to lower the kurtosis.

References

BOTTIN, R. R. JR. & THOMPSON, E. F. 2002 Comparisons of physical and numerical model wave predictions with prototype data at Morro Bay harbor entrance, California. *U. S. Army Engineer.*

DAVEY, A. & STEWARTSON, K. 1974 On three-dimensional packets of surface waves. *Proc. R. Soc. Lond.* A **338**, 101–110.

DYSTHE, K. B. 1979 Note on the modification to the nonlinear Schrödinger equation for application to deep water waves. *Proc. R. Soc. Lond. A* **369**, 105–114.

DYSTHE, K. B. & DAS, K. P. 1981 Coupling between a surface-wave spectrum and an internal wave: modulational interaction. *J. Fluid Mech.*, **104**, 483-503.

FORRISTALL, G. 1978 On the statistical distribution of wave heights in a storm. *J. Geophys. Res.* **83** 8C5), 2353–2358.

GERALD, C. F. & WHEATLEY, P. O. 1994 Applied Numercial Analysis - Fifth edition. *Addison-Wesley Publishing company, Inc.*

GERBER, M. 1987 The Benjamin-Feir instability of a deep water Stokes wavepacket in the presence of a non-uniform medium. *J. Fluid Mech.* **176**, 311–332.

GONZÁLEZ, F. I. 1984 A case study of wave-current-bathymetry interactions at the Columbia river entrance. *J. Phys. Oceanogr.* **14**, 1065–1078.

HASIMOTO, H. & ONO, H. 1972 Nonlinear modulation of gravity waves. *J. Phys. Soc. Japan.* **33**, 805–811.

HELLER, E. 2005 Eric Heller. In *ACM SIGGRAPH 2005 Electronic Art and Animation Catalog* (Los Angeles, California, August 01 - 04, 2005). SIGGRAPH '05. ACM, New York, NY, 78-79.

HJELMERVIK, K., OMMUNDSEN, A. & GJEVIK, B. 2005 Implementation of non-linear advection terms in a high resolution tidal model. *University of Oslo, preprint.*

HJELMERVIK, K., LYNGE, B. K., OMMUNDSEN, A. & GJEVIK, B. 2008 Interaction of tides and storm surges in the Tjeldsunet channel in northern Norway. *Ocean Dynamics* (submitted).

HJELMERVIK, K. & TRULSEN, K 2008 Freak wave statistics on collinear currents *J. Fluid Mech.* (submitted).

JONSSON, I. G. 1990 Wave-current interactions. In *The Sea, Ocean Eng. Sci.* (ed. by B. Le Méhauté & D. M. Hanes), pp. 65–120, Wiley-Interscience, Hoboken, N. J.

LAVRENOV, I. V. 1998 The wave energy concentration at the Agulhas current off South Africa. *Natural Hazards* **17**, 117–127.

LAVRENOV, I. V. & PORUBOV, A. V. 2006 Three reasons for freak wave generation in the non-uniform current. *Eur. J. Mech. B/Fluids* **25**, 574–585.

LO, E. Y. & MEI, C. C. 1985 A numerical study of water-wave modulation based on a higher-order nonlinear Schrödinger equation. *J. Fluid Mech.* **150**, 395–416.

LONGUET-HIGGINS, M. S. & STEWART, R. W. 1961 The changes in amplitude of short gravity waves on steady non-uniform currents. *J. Fluid Mech.* **10**, 529–549.

MACIVER R. D., SIMONS, R. R. & THOMAS, G. P. 2006 Gravity waves interacting with narrow jet-like current. *J. Geophys. Res.* **111**, C03009.

MACMAHAN, J. H., THORNTON, E. B. & RENIERS, A. J. H. M. 2006 Rip current review. *Coastal Engineering* **53**, 191–208.

MCLACHLAN, R. 1994 Sympletic integration of Hamiltonian wave equation. *Numer. Math.* **66** 465.

MEI, C. C. 1989 The applied Dynamics of ocean surface waves. *World Scientific Publishing Co., Singapore.*, ISBN 9971-50-789-7

MORI, N., LIU, P. C. & YASUDA, T. 2002 Analysis of freak wave measurements in the sea of Japan. *Ocean Engineering* **29**, 1399–1414.

MUSLU, G. M. & ERBAY, H. A. 2004 Higher-order split-step Fourier Schemes for the generalized nonlinear Schrödinger equation. *Mathematics and Computers in Simulation* **67**, 581–595.

PEREGRINE, D. H. 1976 Interaction of water waves and currents. *Adv. Appl. Mech.* **16**, 9–117.

Peregrine, D. H. & Smith, R. 1979 Nonlinear effects upon waves near caustics. *Phil. Trans. R. Soc. Land. A* **292**, 341–370.

Stewartson, K. 1977 On the resonant interaction between a surface wave and a weak surface current. *Mathematika* **24**, 37–49.

Stocker, J. D. & Peregrine, D. H. 1999 The current-modified nonlinear Schrödinger equation. *J. Fluid Mech.* **399**, 335–353.

Tayfun, M. A. 1980 Narrow-band nonlinear sea waves. *J. Geophys. Res.* **85**, 1548–1552.

Trulsen, K., Kliakhandler, I., Dysthe, K. B., & Velarde, M. G. 2000 On weakly nonlinear modulation of waves on deep water. *Phys. Fluids* **12**, 2432–2437.

Trulsen, K. & Mei, C. C. 1993 Double reflection of capillary/gravity wavs by a non-uniform current: a boundary–layer theory. *J. Fluid Mech.* **251**, 239–271.

Turpin, F-M., Benmoussa, C. & Mei, C. C. 1983 Efects of slowly varying depth and current on the evolution of a Stokes wavepacket. *J. Fluid Mech.* **132**, 1–23.

Weidman, J. A. C. & Herbst, B. M. 1986 Split-step methods for the solution of the nonlinear Schrödinger equation. *SIAM J. Numer. Analy.* **23**, 485–507.

White, B. S. 1999 Wave action on currents with vorticity. *J. Fluid Mech.* **386**, 329–344.

White, B. S. & Fornberg, B. 1998 On the chance of freak waves at sea. *J. Fluid Mech.* **335**, 113–138.

Yuen, H. C. & Lake, B. M. 1982 Nonlinear dynamics of deep-water gravity waves. *Adv. Appl. Mech.* **22**, 67–229.

Zakharov, V. E. 1968 Stability of periodic waves of finite amplitude on the surface of a deep fluid. *J. Appl. Mech. Tech. Phys.* **9**, 86–94.

Paper 4

Freak wave statistics on collinear currents

Freak wave statistics on collinear currents

KARINA B. HJELMERVIK
AND KARSTEN TRULSEN

Mechanics Division, Department of Mathematics, University of Oslo, Norway

Linear refraction of waves on inhomogeneous current is known to provoke extreme waves. We investigate the effect of nonlinearity on this phenomenon, with respect to the variation of significant wave height, kurtosis and occurrence of freak waves. Monte–Carlo simulations are performed employing a modified nonlinear Schrödinger equation that includes the effects of a prescribed non–potential current. We recommend that freak waves should be defined by a local criterion according to the wave distribution at each location of constant current, not by a global criterion that is either averaged over, or insensitive to, inhomogeneities of the current. Nonlinearity can reduce the modulation of significant wave height. Depending on the configuration of current and waves, the kurtosis and probability of freak waves can either grow or decrease when the wave height increases due to linear refraction. At the centre of an opposing current jet where waves are known to become large, we find that freak waves should be more rare than in the open ocean away from currents. The largest amount of freak waves on an opposing current jet is found at the jet sides where the significant wave height is small.

1. Introduction

It is well known that linear refraction due to currents can provoke large waves. When waves encounter an opposing current, the wave length can be reduced and both the wave height and steepness can be enhanced. When waves encounter an opposing current jet, focusing can further enhance the wave intensity near the centre of the jet. Linear refraction of waves by currents is known to cause navigational problems, e.g. in the Agulhas current, river estuaries, rip currents, entrances in fjords during outgoing tides, and in tidal flows in the coastal zone, (Longuet–Higgins & Stewart 1961; Peregrine 1976; González 1984; Jonsson 1990; Lavrenov 1998; Mori, Liu & Yasuda 2002; Bottin & Thompson 2002; MacIver, Simons & Thomas 2006; MacMahan, Thornton & Reniers 2006). When the steepness thus increases, enhanced nonlinear modulations should be anticipated (Stocker & Peregrine 1999; Lavrenov & Porubov 2006). However, it is not well known how the enhanced effect of nonlinearity will modify the wave height.

Our goal is to investigate how nonlinearity modifies both the significant wave height and the occurrence of freak waves, for waves propagating on inhomogeneous stationary currents. Two important reviews of freak waves, (Kharif & Pelinovsky 2003; Dysthe, Krogstad & Müller 2008), argue that there is no unique definition of freak waves, but it is generally agreed that they belong to the extreme tail of the probability distribution. The most common definition is that a wave is freak when the wave height exceeds a threshold related to the significant wave height. However, due to the inhomogeneity of the current, it becomes necessary to distinguish two different types of statistical distributions for the surface waves. In the first case, the distribution is given as a function of location, each location being associated with a constant current, such that the threshold for freak waves

will depend on the location. In the second case, a common threshold is defined for the entire domain, either based on an averaging over the entire inhomogeneous domain or based on a reference sea state unaffected by currents and bottom topography.

We argue that, at least when the current is known and stationary, the optimal choice is to use distributions specific to each location, and a freak wave criterion that depends on location. The reason is that freak waves should be surprising, also after the knowledge of the current has been taken into account. Some authors have made the other choice (Lavrenov 1998, and references therein), thus identifying numerous freak waves where large waves should be anticipated in any case.

Laboratory measurements of longcrested waves on a transversally uniform current, show that strong opposing currents induce partial wave blocking significantly elevating the limiting steepness and asymmetry of freak waves (Wu & Yao 2004). MacIver, Simons & Thomas (2006) studied waves propagating across a shore-parallel current jet at oblique incidence. They found that a following wave is refracted to a more current-parallel direction with reduced wave height, while an opposing wave becomes more current normal with increased wave height.

Our need to resolve wave phases on non–potential currents restricts us from employing several obvious candidates. White (1999) allowed a prescribed current with vorticity, and derived a wave action equation. Ray theory (White & Fornberg 1998) is used for tracking wave packets. Peregrine & Smith (1979) derived a nonlinear Schrödinger equation useful for caustics where ray theory breaks down. The Zakharov equation (Zakharov 1968) is limited to potential flows.

We shall derive a nonlinear Schrödinger equation that includes an inhomogeneous current with horizontal shear. Some related models have already been published. Stewartson (1977) derived a linear current modified Schrödinger equation to Dysthe level limiting to potential theory. Turpin, Benmoussa & Mei (1983) considered the effects of slowly varying depth and current, and derived a cubic Schrödinger equation limiting to one horizontal dimension. Gerber (1987) used the variational principle to derive a cubic Schrödinger equation for a non–uniform medium, limiting to potential theory in one horizontal dimension. Mei (1989) allowed horizontal shear, and derived the Schrödinger equation to linear order. Stocker & Peregrine (1999) extended the modified nonlinear Schrödinger equation of Dysthe (1979) to include a prescribed potential current induced by for example an internal wave. Our equation will be taken up to cubic nonlinearity, and will include waves and currents in two horizontal dimensions allowing weak horizontal shear.

2. The current modified nonlinear Schrödinger equation

Assume that the total velocity field, $\boldsymbol{v}_{tot} = \boldsymbol{v} + \boldsymbol{V}$, is a superposition of the velocity of a wave field, $\boldsymbol{v} = (u, v, w)$, and a prescribed stationary current field, $\boldsymbol{V} = (U, V, W)$, in a Cartesian coordinate system, (x, y, z). The x–axis is aligned with the principal propagation direction of the waves. The z–axis is vertical with unit vector $\boldsymbol{k}$ pointing upwards. $z = 0$ corresponds to the undisturbed free water surface. The water is assumed inviscid, incompressible and deep with respect to the characteristic wavelength.

The Euler equation for the combined wave and current field can be written as:

$$\frac{\partial \boldsymbol{v}}{\partial t} + \boldsymbol{v}_{tot} \cdot \boldsymbol{\nabla} \boldsymbol{v}_{tot} = -\frac{1}{\rho} \boldsymbol{\nabla} p_{tot} - g\boldsymbol{k} \tag{2.1}$$

The total pressure, $p_{tot} = p_s + p + P$, is a combination of the dynamic pressure due to the wave field, p, the dynamic pressure due to the current field, P, and the static pressure,

$p_s = -\rho g z + p_a$, where ρ is the density, g is the acceleration of gravity, and p_a is the atmospheric pressure.

The surface boundary equations for the combined field at $z = \eta + \zeta$ can then be written as:

$$\frac{\partial \eta}{\partial t} + \boldsymbol{v}_{tot} \cdot \boldsymbol{\nabla}(\eta + \zeta) = w + W \qquad (2.2a)$$

$$p_{tot} = p_a \qquad (2.2b)$$

η and ζ are the surface displacements associated with the wave field and the current field respectively.

The vorticity of the waves, $\boldsymbol{\gamma} = \boldsymbol{\nabla} \times \boldsymbol{v}$, obeys the equation:

$$\frac{\partial \boldsymbol{\gamma}}{\partial t} + \boldsymbol{v}_{tot} \cdot \boldsymbol{\nabla}\boldsymbol{\gamma} - \boldsymbol{\gamma} \cdot \boldsymbol{\nabla}\boldsymbol{v}_{tot} = -\boldsymbol{v} \cdot \boldsymbol{\nabla}\boldsymbol{\Gamma} + \boldsymbol{\Gamma} \cdot \boldsymbol{\nabla}\boldsymbol{v} \qquad (2.3)$$

If the vorticity of the current, $\boldsymbol{\Gamma} = (\Gamma_x, \Gamma_y, \Gamma_z) = \boldsymbol{\nabla} \times \boldsymbol{V}$, equals zero, (2.3) is homogeneous with respect to $\boldsymbol{\gamma}$, and if the wave field starts out irrotational, it will remain irrotational. For waves riding a current field with vorticity, vorticity will develop in the wave field as well. We therefore derive a current modified nonlinear Schrödinger equation that allows a small amount of vorticity.

Let a, k_c and ω_c be the characteristic amplitude, wavenumber and angular frequency of the surface waves. We employ the steepness of the waves as a small ordering parameter in the following, $\epsilon = k_c a \ll 1$, thus $k_c \eta = O(\epsilon)$ and $\boldsymbol{v}\frac{k_c}{\omega_c} = O(\epsilon)$. The horizontal current velocities are assumed just small enough to avoid collinear reflection of the waves, $(U, V)\frac{k_c}{\omega_c} = O(\epsilon)$. The vertical current velocity is assumed negligible $W\frac{k_c}{\omega_c} = O(\epsilon^2)$. It follows from the Bernoulli equation that the surface displacement induced by the current is small, $k_c \zeta = O(\epsilon^2)$. Let the horizontal and vertical length scales, L, of the current be longer than a characteristic wavelength so that $1/(k_c L) = O(\epsilon)$. The horizontal vorticities, $(\Gamma_x, \Gamma_y)/\omega_c = O(\epsilon^3)$, and the vertical vorticity, $\Gamma_z/\omega_c = O(\epsilon^2)$, are one order smaller than the vorticities assumed by Mei (1989). In the following all equations, variables and sizes are scaled according to the above assumptions, and made dimensionless using the characteristic length and time scales of the wave field.

The wave field is represented by perturbation series for the surface displacement, η, the velocity, $\boldsymbol{v}$, and the pressure, p, (see appendix). The perturbation series for the surface displacement is given by:

$$\eta = \epsilon^2 \bar{\eta} + \frac{1}{2}\left(B\mathrm{e}^{\mathrm{i}(x-t)} + \epsilon B_2 \mathrm{e}^{2\mathrm{i}(x-t)} + \epsilon^2 B_3 \mathrm{e}^{3\mathrm{i}(x-t)} + \cdots + \mathrm{c.c.}\right) \qquad (2.4)$$

$\bar{\eta}$ is the mean surface displacement. x is the principal propagation direction. B, B_2 and B_3 are the first, second and third harmonics of the surface displacement. We have fixed the characteristic wavenumber appropriate for waves undisturbed by current, therefore the entire effect of refraction is represented by the modulation of B. The perturbation series for the velocity and the pressure are similar.

Through Taylor expansion around $z = 0$ and perturbation expansion (see appendix) we get the following dimensionless Schrödinger equation with current terms, NLSC, for the first harmonic of the surface elevation of the waves:

$$\frac{\partial B}{\partial x} = (\mathrm{L+C+N})B \qquad (2.5)$$

L contains the linear terms with constant coefficients, C contains the linear terms with

variable coefficients, and N is the nonlinear term:

$$L = -2\frac{\partial}{\partial t} - i\frac{\partial^2}{\partial t^2} + \frac{i}{2}\frac{\partial^2}{\partial y^2}$$

$$C = -2iU + 6U\frac{\partial}{\partial t} + 5iU^2 - 2V\frac{\partial}{\partial y} - \frac{\partial U}{\partial x}$$

$$N = -i|B|^2$$

Equation (2.5) should be valid for evolution over a distance $x = O(\epsilon^{-2})$ and for modulations of spectral width $O(\epsilon)$ in y and t.

All the terms in (2.5) may be derived from Stocker & Peregrine (1999) by rescaling their current even though they used potential theory. Our horizontal current is one order stronger, but their equation is of Dysthe order. When vorticity is allowed, new terms will appear if (2.5) is taken to the next order. To obtain (2.5) from (20) in Stocker & Peregrine (1999) one has to recall that the first is written in terms of the free-surface envelope, where as the latter is written in terms of the envelope of the potential.

3. Model setup

Simulations are performed with a second order split–step scheme based on Lo & Mei (1985) and Muslu & Erbay (2004). A Fourier method is used on the linear terms with constant coefficients, LB. And a second order Runge–Kutta scheme is used on the nonlinear term and the linear terms with variable coefficients, $(C+N)B$. The wave field is assumed periodic with respect to y and t. The integrating step used is $\Delta x = 0.2$. Each ensemble consists of 30 simulations.

The Fourier transform with respect to y and t is given by:

$$\hat{B}_{ij} = \frac{1}{MN}\sum_{m=0}^{M-1}\sum_{n=0}^{N-1} B_{mn}e^{i(\Omega_j t_n - k_{yi}y_m)} \tag{3.1}$$

where $y_m = m\Delta y$, $t_n = n\Delta t$, $k_{yi} = i\Delta k_y$, and $\Omega_j = j\Delta\omega$. The length of each time series is $T = 2000$. Using $N = 1024$ times, the time step is $\Delta t = \frac{T}{N} \approx 1.95$ and $\Delta\omega = \frac{2\pi}{T} \approx 0.0031$. The width of the simulation area, $y = [-40, 40]$, with $M = 32$ points, gives $\Delta y = 2.5$ and $\Delta k_y \approx 0.079$.

Both unidirectional and shortcrested incoming waves with Gaussian spectrum have been studied. The Fourier amplitudes at $x = 0$ are given respectively by:

$$\hat{B}_j = \epsilon\sqrt{\frac{\Delta\omega}{\sqrt{2\pi}\sigma_\omega}}e^{-\frac{\Omega_j^2}{4\sigma_\omega^2}+i\psi_j} \tag{3.2}$$

$$\hat{B}_{ij} = \epsilon\sqrt{\frac{\Delta k_y\Delta\omega}{2\pi\sigma_y\sigma_\omega}}e^{-\frac{\Omega_j^2}{4\sigma_\omega^2}-\frac{k_{yi}^2}{4\sigma_y^2}+i\psi_{ij}} \tag{3.3}$$

The frequency is given by $\omega_j = 1 + \Omega_j$. The phases, ψ_{ij}, are statistically independent and uniformly distributed on the interval $[0, 2\pi)$. We have chosen $\epsilon = 0.1$. σ_ω and σ_y are bandwidths in Fourier room. We have studied $\sigma_\omega = 0.05, 0.1$ and 0.2. For the shortcrested cases we have chosen $\sigma_y = 0.05$ and 0.2 to study different crest lengths.

The NLSC equation, (2.5), may be used for a large range of prescribed currents. Here

we have chosen two types; a narrow surface current jet (sec. 4.1) given by:

$$U = \begin{cases} 0 & \text{when } x \leqslant X, \text{ and/or } |y| \geqslant Y \\ U_0 \sin^2\left(\frac{\pi}{2\Delta X}(x-X)\right)\cos^2\left(\frac{\pi y}{2Y}\right) & \text{when } x > X, \text{ and } x < X + \Delta X \\ U_0 \cos^2\left(\frac{\pi y}{2Y}\right) & \text{when } x \geqslant X + \Delta X \end{cases} \quad (3.4)$$

and a transversally uniform current (sec. 4.3) given by:

$$U = \begin{cases} 0 & \text{when } x \leqslant X \\ U_0 \sin^2\left(\frac{\pi}{2\Delta X}(x-X)\right) & \text{when } x > X, \text{ and } x < X + \Delta X \\ U_0 & \text{when } x \geqslant X + \Delta X \end{cases} \quad (3.5)$$

The wave field is allowed about 32 wavelengths, $x = [0, X)$ where $X = 200$, to develop before it encounters a current. $Y = 10$ is half the width of the jet. And $\Delta X = 100$ is the current build–up length. In this paper we compare three cases for the current: no current, co–current with $U_0 = 0.05$, and opposing current with $U_0 = -0.05$ which is not enough to reflect the waves, but sufficient to study the characteristic features of opposing currents. More current cases are studied in Hjelmervik & Trulsen (2009).

Simulations and observations of tidal currents suggest that establishing current jets are more fanned in than terminating current jets are fanned out (Hjelmervik, Ommundsen & Gjevik 2005; Hjelmervik *et al.* 2008). Test simulations show that the current across the jet, V, needed to satisfy the continuity equation, has negligible impact on the results and may thus be set to zero in the NLSC equation. Alternatively, the continuity equation can be satisfied by a vertical current, W, which does not appear within the truncation level of the NLSC equation at the surface.

4. Results

For each of the simulated ensembles we compute the significant wave height, H_s, the kurtosis, κ, of the surface displacement, and the amount of freak waves from time series at fixed locations. Statistical features are calculated using the envelope to first order. The free surface may be reconstructed to second order by (2.4), using the first harmonic term proportional to B and the second harmonic term proportional to B_2. Since the second harmonic complex envelope, B_2, is not an explicit function of the current field according to (A 28b), the contribution from bound waves are not expected to modify wave statistics of the free waves differently from the case of no current within the truncation level of (2.5). Second order harmonic bound contributions without currents are well known from the litterature (Longuet–Higgins & Stewart 1961; Tayfun 1980; Socquet–Juglard *et al.* 2005, and others). We shall limit our consideration of wave statistics to contributions from free waves only.

$$H_s(x,y) = 4\sqrt{\overline{\eta^2}} = 4\sqrt{\frac{1}{2}\overline{|B|^2}} \quad (4.1)$$

$$\kappa(x,y) = \frac{\overline{\eta^4}}{\overline{\eta^2}^2} = \frac{3}{2}\frac{\overline{|B|^4}}{\overline{|B|^2}^2} \quad (4.2)$$

The overbar represents combined time and ensemble averaging. The significant wave height equals four times the standard deviation of the surface elevation. The kurtosis equals three when the surface displacement is Gaussian distributed. We define a wave as freak when its wave height exceeds 2.2 times the significant wave height, H_s:
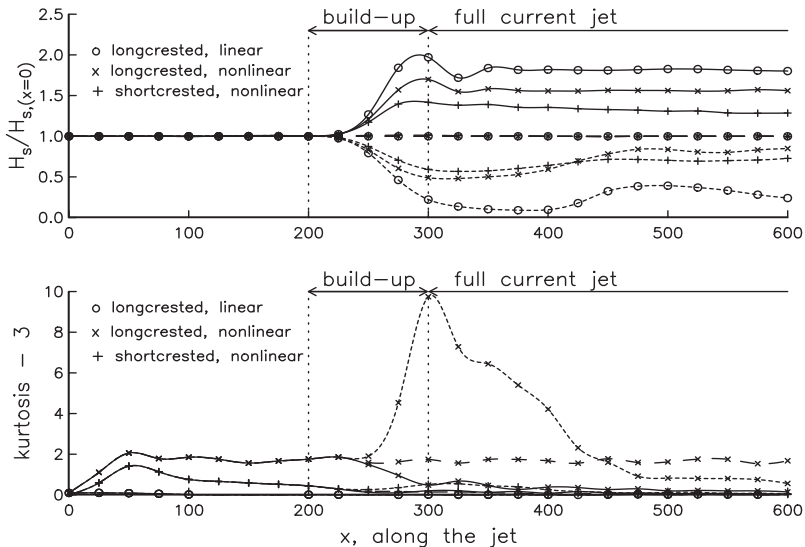
$$H = 2|B| > 2.2 H_s \quad (4.3)$$

FIGURE 1. The significant wave height (upper) and kurtosis (lower) with no current (— —), and in the centre of current jets with $U_0 = -0.05$ (——) and 0.05 (- - -) for unidirectional and shortcrested ($\sigma_y = 0.05$) incoming waves with $\sigma_\omega = 0.1$. For the case of no current, there are three curves on top of each other in the upper panel.

According to the Rayleigh distribution for wave height, 0.006% of the waves should be freak.

4.1. *Current jet*

Suppose that the waves meet a collinear surface current jet given by (3.4).

The significant wave height increases for waves encountering an opposing current and decreases for waves encountering a co–current (figure 1, upper panel). The significant wave height oscillates before stabilising. Test simulations with wider simulation areas, show that the oscillations appearing on the opposing current jet do not depend on the width of the simulation area, but on the width and form of the current jet, while the oscillations after 64 wavelengths ($x \approx 400$) on the co–current may be due to restrictions on the simulation area.

The significant wave height is larger in the centre and smaller at the sides of an opposing current jet, while it is smaller in the centre and larger at the sides of a co–current jet (figure 2). These results are very similar for different values of σ_ω, and qualitatively equal for any cross section after the current jet is introduced. When waves encounter an opposing current jet, energy is transferred from the sides of the jet into the centre of the jet resulting in larger significant wave height in the centre of the jet and smaller at the jet sides. More energy is transferred in linear than in nonlinear simulations, and the longer the incoming crest lengths are. When waves encounter a co–current jet, the energy is transfered in the opposite direction, resulting in larger significant wave height at the jet sides and smaller in the centre of the jet. Again more energy is transfered in linear than in nonlinear simulations, and the longer the incoming crest lengths are.
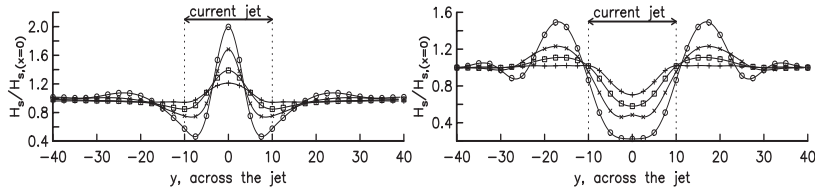
FIGURE 2. The significant wave height at x=300 across current jets with $U_0 = -0.05$ (left) and 0.05 (right). Unidirectional incoming waves with linear simulations (circle) and nonlinear simulations (cross). Shortcrested incoming waves with $\sigma_y = 0.05$ (square) and $\sigma_y = 0.2$ (plus) with nonlinear simulations. Incoming $\sigma_\omega = 0.1$.

The kurtosis deviates little from three in linear simulations and in nonlinear simulations with shortcrested incoming waves (figure 1, lower panel). In nonlinear simulations with unidirectional incoming waves, the kurtosis increases to a maximum before decreasing to a stable level. The stable level is reached before the current jet is introduced, and increases with decreasing incoming bandwidth in frequency (figure 3, left panels). Simulations with different incoming crest lengths show that larger crest lengths result in larger deviations in the kurtosis both before and shortly after the build–up of the current jet.

When unidirectional waves meet an opposing current jet, the kurtosis decreases in the centre of the jet where the significant wave height grows. The largest kurtosis across the jet is at the sides of the jet where the significant wave height is smallest. When unidirectional waves meet a co–current jet, the kurtosis decreases at the sides of the jet where the significant wave height grows. In this case the largest kurtosis is in the centre of the jet where the significant wave height is smallest. Test simulations with different build–up lengths, $\Delta X = 50, 100, 200$, and 300, show that smaller current gradients along the waves, $\partial U/\partial x$, results in smaller changes in the kurtosis along the jet, $|\partial \kappa/\partial x|$, and smaller maximums of the kurtosis across the jet.

Since the current jet is narrower than ten wavelengths, the unidirectional incoming waves behave as shortcrested waves (Gramstad & Trulsen 2007) and the kurtosis decreases as the wave field is adjusted to the current jet (figure 1, lower panel). After the wave field is adjusted to the current jet, the kurtosis is close to three. The significant wave height in the centre of the jet is still large in the opposing current jet and small in the co–current jet. The adjustment length of waves without current is well known (Onorato *et al.* 2002; Socquet–Juglard *et al.* 2005; Gramstad & Trulsen 2007). Our numerical results suggest that the adjustment length for waves on collinear current jets can be considerably longer than for waves without currents.

The amount of freak waves is represented well by the kurtosis in our study (figure 3). The largest amount of freak waves is at the sides of the opposing current jet, and in the centre of the co–current jet (figure 3, right panels). Small incoming bandwidths in frequency results in larger maximum of the kurtosis and amount of freak waves, while the significant wave height seems nearly independent of initial bandwidth (Hjelmervik & Trulsen 2009). The waves are large in the centre of an opposing current jet, but the proportion that is freak, is smaller than away from the current. In linear simulations the amount of freak waves is less than 0.04% at all locations both along and across the jet, but our data material seems to be insufficient to calculate a more exact percentage. In nonlinear simulations with shortcrested incoming waves ($\sigma_y = 0.05$) the amount of freak waves is less than 0.15% (figure 4, right panels). The longer the incoming crest lengths the larger kurtosis and amount of freak waves. Gramstad & Trulsen (2007) performed a
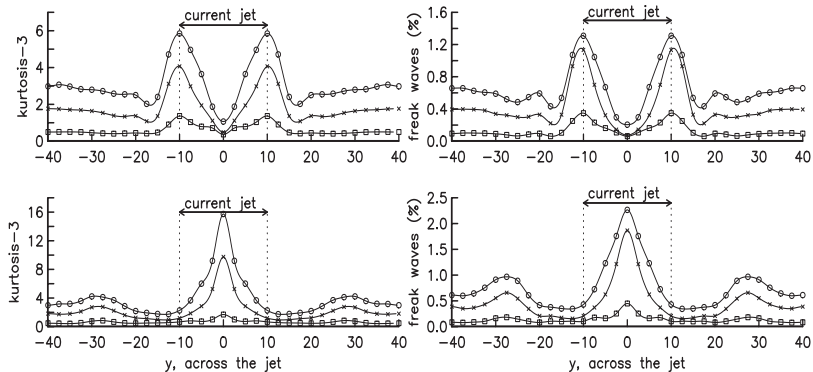
FIGURE 3. The kurtosis (left) and amount of local freak waves (right) for unidirectional incoming waves at x=300 across current jets with $U_0 = -0.05$ (upper) and 0.05 (lower). Incoming $\sigma_\omega = 0.05$ (circle), 0.1 (cross) and 0.2 (square). Nonlinear simulations.
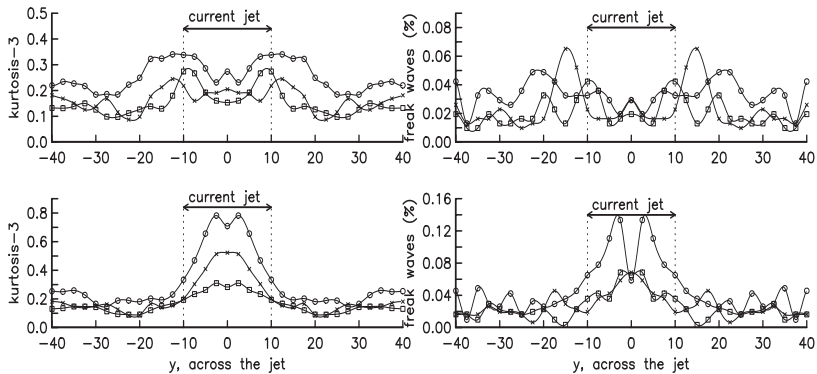

FIGURE 4. The kurtosis (left) and amount of local freak waves (right) for incoming shortcrested waves ($\sigma_y = 0.05$) at x=300 across current jets with $U_0 = -0.05$ (upper) and 0.05 (lower). Incoming $\sigma_\omega = 0.05$ (circle), 0.1 (cross) and 0.2 (square). Nonlinear simulations.

large number of simulations with a modified nonlinear Schrödinger equation in order to reveal how the occurrence of freak waves on deep water depends on crest lengths. They found a clear difference between shortcrested and longcrested waves, distinguished by a limiting crest length of approximately ten wavelengths ($\sigma_y \approx 0.1$). Our results indicate that a similar qualitative difference exists when a current jet is introduced. The longer the crest lengths, the stronger the variations in significant wave height, kurtosis and amount of freak waves across the jet.

4.2. *Space or time averaged significant wave height*

Our definition of freak waves by (4.3) requires knowledge of the significant wave height H_s. Since the waves propagate in an inhomogeneous medium, there are at least three
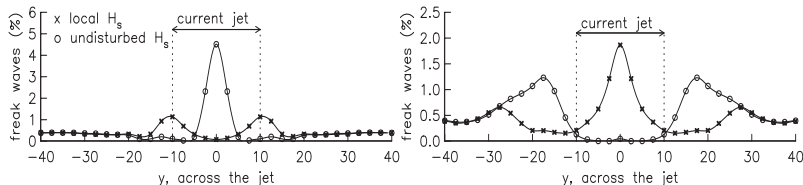
FIGURE 5. The amount of freak waves at x=300 for unidirectional incoming waves across current jets with $U_0 = -0.05$ (left) and 0.05 (right). Incoming $\sigma_\omega = 0.1$. Nonlinear simulations.
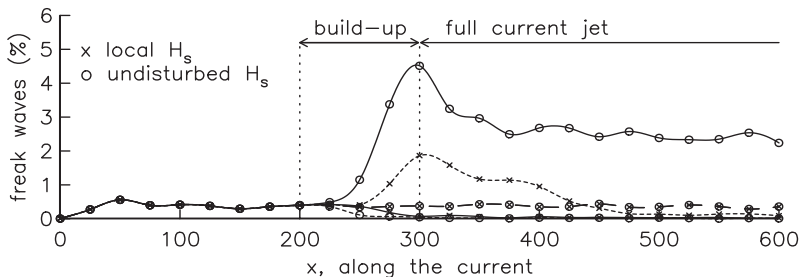

FIGURE 6. The amount of freak waves for unidirectional incoming waves with no current (——), and in the centre of current jets with $U_0 = -0.05$ (——) and 0.05 (- - -). Incoming $\sigma_\omega = 0.1$. Nonlinear simulations.

different strategies for determining H_s. The strategy which we recommend and have adopted here, is to determine H_s at fixed locations of constant current, i.e. a *local* significant wave height. This method corresponds to classical field measurements taken at fixed locations. A second strategy would be to determine a *global* significant wave height by spatial averaging over the inhomogeneous medium. This method likely corresponds to analysis based on satellite imaging of the ocean surface. A third strategy would be to define an *undisturbed* significant wave height for a wave field unaffected by the inhomogeneities. This method corresponds to the work done by e.g. Lavrenov (1998).

Lavrenov (1998) considered the propagation of swell from the southern latitudes into the opposing Agulhas current. He found that the mean wave height is larger in the centre of the jet than at the jet sides. Our simulations show that this applies for both linear and nonlinear simulations, and both unidirectional and shortcrested incoming waves. He suggested that the amount of freak waves is large in the centre of the jet since the mean wave height is large there.

Figures 5 and 6 show that the amount of "freak" waves strongly depends on the strategy used to define them. The kurtosis is a good indicator for freak waves only if the local significant wave height is used to define them. Then the freak wave amount is large at locations with a large amount of unexpectedly high waves compared to what is expected at the same locations, and when the waves are adjusted to the current jet, the freak wave amount is small. If the undisturbed significant wave height is used to define the freak waves, the local significant wave height is a good indicator for the freak wave amount. Then the freak wave amount is large at locations with large waves compared to wave heights elsewhere, and when the waves are adjusted to the current jet, the freak wave amount is still large. We believe it is preferable to reserve the term "freak" waves only to those waves that are surprising even after knowledge of inhomogeneities are taken
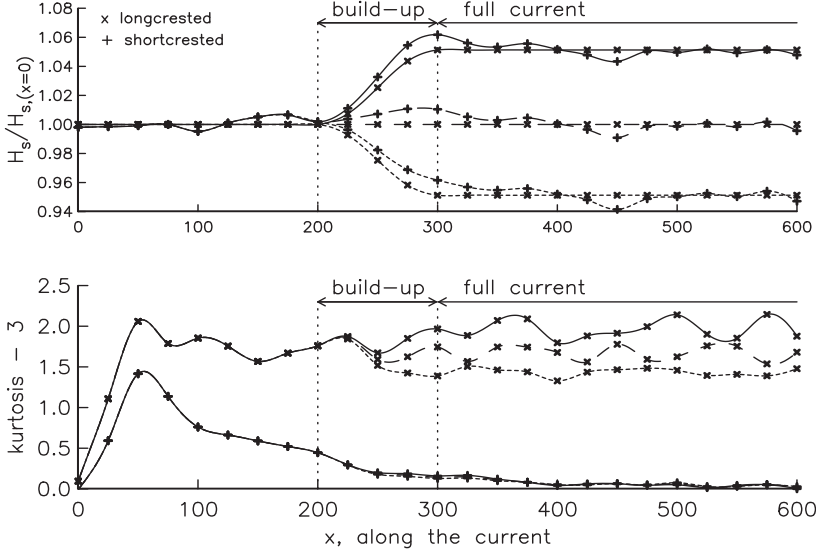
FIGURE 7. The significant wave height (upper) and kurtosis (lower) for unidirectional and short-crested ($\sigma_y = 0.05$) incoming waves with no current (— —), and on transversally uniform currents with $U_0 = -0.05$ (——) and 0.05 (- - -). Incoming $\sigma_\omega = 0.1$. Nonlinear simulations.
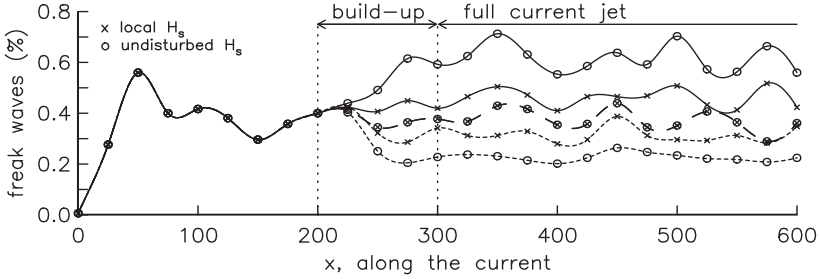

FIGURE 8. The amount of freak waves for unidirectional incoming waves with no current (— —), and on transversally uniform currents with $U_0 = -0.05$ (——) and 0.05 (- - -). Incoming $\sigma_\omega = 0.1$. Nonlinear simulations.

into account. To ensure that a freak wave belongs to the upper tail of the probability distribution, we thus recommend the local significant wave height for application to the criterion (4.3).

4.3. *Transversally uniform current*

Suppose that the waves meet a transversally uniform current given by (3.5).

The significant wave height (figure 7, upper panel) increases when the waves meet an increasing opposing current and decreases when the waves meet an increasing co–current. Since the current does not cause any energy transfer transversally, the changes

are smaller than when the waves meet a current jet (figure 1, upper panel). The significant wave height is near constant after the build–up of the current.

The kurtosis (figure 7, lower panel) for longcrested waves increases slightly when the significant wave height increases, and decreases slightly when the significant wave height decreases. This effect can hardly be seen for short crested waves. After the current build–up the unidirectional incoming waves are still unidirectional and the kurtosis stays at the same level. This is in contradiction to the case where unidirectional incoming waves meet a current jet (figure 1, lower panel). Then the kurtosis decreases with increasing significant wave height, increases with decreasing significant wave height, and decreases after the build–up. The kurtosis for unidirectional incoming waves with no current (figures 1 and 7, lower panels) stays at a high level, indicating that the cubic nonlinear Schrödinger equation produces larger kurtosis than the modified Schrödinger equation by Trulsen & Dysthe (1996) derived to next order (see Gramstad & Trulsen 2007, figure 2).

On a transversally uniform current the amount of freak waves (figure 8) is well indicated by the kurtosis also when the undisturbed significant wave height is used to calculate the amount of freak waves. If the undisturbed significant wave height is used, there are slightly more freak waves in an opposing current and less in a co–current, than if the local significant wave height is used. Since the current does not introduce transversal energy transfer, the freak wave amounts are smaller than if the waves meet a current jet (figure 5).

5. Conclusion

We have derived a nonlinear Schrödinger equation suitable for spatial wave propagation on inhomogeneous currents. We have used this equation for Monte–Carlo simulations to investigate wave statistics on inhomogeneous currents, in particular on narrow current jets. Several surprising features of nonlinear wave evolution on nonuniform current were revealed. Wave statistics has been derived based on the envelope to the first order, which was used to estimate the wave height correct to second order.

The evolution and statistics of both short– and longcrested waves on transversally uniform currents is found to be qualitatively different from waves on current jets.

Considering waves that approach an opposing current jet, we find that the amount of freak waves is minimum in the centre of the jet where the wave heights are largest, while the amount of freak waves is maximum at the sides of the jet where the wave heights are smallest.

The definition of both significant wave height and of freak waves can be ambiguous in inhomogeneous media. We recommend that *local* definitions are used to ensure that freak waves remain surprising even after classical knowledge of the inhomogeneous medium has been taken into account.

We see evidence that the distances over which a wave field has to propagate in order to be adjusted to the medium can become much longer in the presence of inhomogeneous currents than in the absence of currents. This may be an important consideration for the appropriate choice of wave models in coastal waters.

Appendix. Derivation of the NLSC equation

Taylor expansions around $z = 0$ gives the surface boundary equations, $(2.2a\text{--}b)$, on the form:

$$\frac{\partial \eta}{\partial t} + \boldsymbol{v}_{tot} \cdot \boldsymbol{\nabla}(\eta + \zeta) + (\eta + \zeta)\frac{\partial \boldsymbol{v}_{tot}}{\partial z} \cdot \boldsymbol{\nabla}(\eta + \zeta) + \frac{1}{2}(\eta + \zeta)^2 \frac{\partial^2 \boldsymbol{v}_{tot}}{\partial z^2} \cdot \boldsymbol{\nabla}(\eta + \zeta)$$

$$= w + W + (\eta + \zeta)\frac{\partial}{\partial z}(w + W) + \frac{1}{2}(\eta + \zeta)^2 \frac{\partial^2}{\partial z^2}(w + W) + \cdots \qquad (A\,1a)$$

$$p_{tot} + (\eta + \zeta)\frac{\partial p_{tot}}{\partial z} + \frac{1}{2}(\eta + \zeta)^2 \frac{\partial^2 p_{tot}}{\partial z^2} + \cdots = p_a \qquad (A\,1b)$$

The waves are assumed on deep water, that is $\boldsymbol{v}, p \to 0$ as $z \to -\infty$.

In accordance with the scaling assumptions from section 2, all equations, variables and sizes in the following are made dimensionless using the characteristic length and time scales of the wave field, so that $k_c \boldsymbol{x} \to \boldsymbol{x}$, $\epsilon k_c \boldsymbol{x} \to \bar{\boldsymbol{x}}$, $\omega_c t \to t$, $k_c \eta \to \epsilon \eta$, $k_c \zeta \to \epsilon^2 \zeta$, $\frac{k_c}{\omega_c}\boldsymbol{u} \to \epsilon \boldsymbol{u}$, $\frac{k_c}{\omega_c}(U, V) \to \epsilon(U, V)$, $\frac{k_c}{\omega_c}W \to \epsilon^2 W$, $\frac{k_c}{\rho g}p \to \epsilon p$, and $\frac{k_c}{\rho g}P \to \epsilon^2 P$.

The scaled Euler equation for the waves (2.1) to the third order of ϵ is:

$$\frac{\partial u}{\partial t} + \epsilon\left(U\frac{\partial u}{\partial x} + V\frac{\partial u}{\partial y} + \boldsymbol{v}\cdot\boldsymbol{\nabla}u\right) + \epsilon^2\left(u\frac{\partial U}{\partial \bar{x}} + v\frac{\partial U}{\partial \bar{y}} + W\frac{\partial u}{\partial z}\right) = -\frac{\partial p}{\partial x} \quad (A\,2a)$$

$$\frac{\partial v}{\partial t} + \epsilon\left(U\frac{\partial v}{\partial x} + V\frac{\partial v}{\partial y} + \boldsymbol{v}\cdot\boldsymbol{\nabla}v\right) + \epsilon^2\left(u\frac{\partial V}{\partial \bar{x}} + v\frac{\partial V}{\partial \bar{y}} + W\frac{\partial v}{\partial z}\right) = -\frac{\partial p}{\partial y} \quad (A\,2b)$$

$$\frac{\partial w}{\partial t} + \epsilon\left(U\frac{\partial w}{\partial x} + V\frac{\partial w}{\partial y} + \boldsymbol{v}\cdot\boldsymbol{\nabla}w\right) + \epsilon^2 W\frac{\partial w}{\partial z} = -\frac{\partial p}{\partial z} \quad (A\,2c)$$

The scaled equation for the divergence of the Euler equation for the waves (2.1) to the third order of ϵ is:

$$\epsilon\left(\left(\frac{\partial u}{\partial x}\right)^2 + \left(\frac{\partial v}{\partial u}\right)^2 + \left(\frac{\partial w}{\partial z}\right)^2 + 2\frac{\partial u}{\partial y}\frac{\partial v}{\partial x} + 2\frac{\partial u}{\partial z}\frac{\partial w}{\partial x} + 2\frac{\partial v}{\partial z}\frac{\partial w}{\partial y}\right)$$

$$+2\epsilon^2\left(\frac{\partial u}{\partial x}\frac{\partial U}{\partial \bar{x}} + \frac{\partial u}{\partial y}\frac{\partial V}{\partial \bar{x}} + \frac{\partial v}{\partial x}\frac{\partial U}{\partial \bar{y}} + \frac{\partial v}{\partial y}\frac{\partial V}{\partial \bar{y}}\right) = -\frac{\partial^2 p}{\partial x^2} - \frac{\partial^2 p}{\partial y^2} - \frac{\partial^2 p}{\partial z^2} \qquad (A\,3)$$

The scaled surface equations for the waves $(A\,1a\text{--}b)$ to the third order of ϵ are:

$$\frac{\partial \eta}{\partial t} + \epsilon(\boldsymbol{v} + \boldsymbol{V})\cdot\boldsymbol{\nabla}\eta + \epsilon^2\eta\frac{\partial \boldsymbol{v}}{\partial z}\cdot\boldsymbol{\nabla}\eta = w + \epsilon\eta\frac{\partial w}{\partial z} + \epsilon^2\left(\zeta\frac{\partial w}{\partial z} + \frac{1}{2}\eta^2\frac{\partial^2 w}{\partial z^2}\right) \; (A\,4a)$$

$$p - \eta + \epsilon\eta\frac{\partial p}{\partial z} + \epsilon^2\left(\zeta\frac{\partial p}{\partial z} + \frac{1}{2}\eta^2\frac{\partial^2 p}{\partial z^2}\right) = 0 \qquad (A\,4b)$$

The wave field is represented by perturbation series for the surface displacement, η, the velocity, $\boldsymbol{v}$, and the dynamic pressure, p:

$$\begin{aligned}
\eta &= \epsilon^2\bar{\eta} + \frac{1}{2}\left(B_1 e^{i(x-t)} + \epsilon B_2 e^{2i(x-t)} + \cdots + \text{c.c.}\right) \\
\boldsymbol{v} &= \epsilon^2\bar{\boldsymbol{v}} + \frac{1}{2}\left(\boldsymbol{v}_1 e^{i(x-t)} + \epsilon\boldsymbol{v}_2 e^{2i(x-t)} + \cdots + \text{c.c.}\right) \\
p &= \epsilon\bar{p} + \frac{1}{2}\left(p_1 e^{i(x-t)} + \epsilon p_2 e^{2i(x-t)} + \cdots + \text{c.c.}\right)
\end{aligned} \qquad (A\,5)$$

We shall assume that the waves are modulated on the slow spatial scales $\bar{x}$ and $\bar{y}$ and a correspondingly slow time scale $\epsilon t = \bar{t}$. Thus $\bar{\eta} = \bar{\eta}(\bar{x}, \bar{y}, \bar{t})$, $\bar{\boldsymbol{v}} = \bar{\boldsymbol{v}}(\bar{x}, \bar{y}, z, \bar{t})$, and $\bar{p} = \bar{p}(\bar{x}, \bar{y}, z, \bar{t})$ are the mean surface displacement, mean induced velocity, and mean dynamic pressure respectively, while $B_n = B_n(\bar{x}, \bar{y}, \bar{t})$, $\boldsymbol{v}_n = \boldsymbol{v}_n(\bar{x}, \bar{y}, z, \bar{t})$, and $p_n =$

$p_n(\bar{x}, \bar{y}, z, \bar{t})$ are the n'th harmonics of the surface displacement, induced current, and dynamic pressure respectively. The characteristic wavenumber is fixed appropriate for waves undisturbed by current, therefore the entire effect of refraction is represented by the modulation of B_1.

The horizontal vorticities and the vertical vorticity are all one order higher than the vorticities used by Mei (1989), that is $(\Gamma_x, \Gamma_y) = O(\epsilon^3)$ and $\Gamma_z = O(\epsilon^2)$. Since the vorticity is assumed to be small, the chosen order of the mean functions are supported by Dysthe (1979). Both the mean functions and the harmonics, are perturbed:

$$
\begin{aligned}
\bar{\eta} &= \bar{\eta}_2 + \cdots, & B_n &= B_{n0} + \epsilon B_{n1} + \epsilon^2 B_{n2} + \cdots \\
\bar{\boldsymbol{v}} &= \bar{\boldsymbol{v}}_2 + \cdots, & \boldsymbol{v}_n &= \boldsymbol{v}_{n0} + \epsilon \boldsymbol{v}_{n1} + \epsilon^2 \boldsymbol{v}_{n2} + \cdots \\
\bar{p} &= \bar{p}_1 + \epsilon \bar{p}_2 + \cdots, & p_n &= p_{n0} + \epsilon p_{n1} + \epsilon^2 p_{n2} + \cdots
\end{aligned}
\tag{A 6}
$$

A.1. First order terms

The first harmonic terms of first order of ϵ for the divergence of the Euler equation (A 3) are:

$$
p_{10} - \frac{\partial^2 p_{10}}{\partial z^2} = 0
\tag{A 7}
$$

which has the general solution:

$$
p_{10} = A_{10}(\bar{x}, \bar{y}, \bar{t})\mathrm{e}^z
\tag{A 8}
$$

The first harmonic terms of first order of ϵ in the surface equations (A 4a–b) give:

$$
A_{10} = B_{10}
\tag{A 9}
$$

The first harmonic terms of first order of ϵ in the Euler equation (A 2a–c) then give respectively:

$$
u_{10} = B_{10}\mathrm{e}^z
\tag{A 10a}
$$

$$
v_{10} = 0
\tag{A 10b}
$$

$$
w_{10} = -\mathrm{i}B_{10}\mathrm{e}^z
\tag{A 10c}
$$

A.2. Second order terms

A.2.1. Zeroth harmonic

The zeroth harmonic terms of second order of ϵ for the z–component of the Euler equation (A 2c) are:

$$
\frac{\mathrm{i}}{4}u_{10}w_{10}^* + \frac{\mathrm{i}}{4}u_{10}^* w_{10} + \frac{1}{4}w_{10}\frac{\partial w_{10}^*}{\partial z} + \frac{1}{4}w_{10}^*\frac{\partial w_{10}}{\partial z} = -\frac{\partial \bar{p}_1}{\partial z}
\tag{A 11}
$$

Using the results (A 10) from first order, gives:

$$
|B_{10}|^2 \mathrm{e}^{2z} = -\frac{\partial \bar{p}_1}{\partial z}
\tag{A 12}
$$

which has the solution:

$$
\bar{p}_1 = \bar{A}_1(\bar{x}, \bar{y}, \bar{t}) - \frac{1}{2}|B_{10}|^2 \mathrm{e}^{2z}
\tag{A 13}
$$

The zeroth harmonic terms of second order of ϵ in the dynamic surface equation (A 4b) are:

$$
\bar{p}_1 + \frac{1}{4}B_{10}\frac{\partial p_{10}^*}{\partial z} + \frac{1}{4}B_{10}^*\frac{\partial p_{10}}{\partial z} = 0 \qquad \text{at } z = 0
\tag{A 14}
$$

Using the results (A 8–A 9) from first order and the solution for $\bar{p}_1$ (A 13), gives $\bar{A}_1 = 0$.

A.2.2. *First harmonic*

The first harmonic terms of second order of ϵ for the divergence of the Euler equation (A 3) are:

$$2\mathrm{i}\frac{\partial p_{10}}{\partial \bar{x}} = p_{11} - \frac{\partial^2 p_{11}}{\partial z^2} \tag{A 15}$$

Using the results (A 8–A 9) from leading order, gives:

$$2\mathrm{i}\frac{\partial B_{10}}{\partial \bar{x}}\mathrm{e}^z = p_{11} - \frac{\partial^2 p_{11}}{\partial z^2} \tag{A 16}$$

which has the solution:

$$p_{11} = A_{11}(\bar{x}, \bar{y}, \bar{t})\mathrm{e}^z - \mathrm{i}\frac{\partial B_{10}}{\partial \bar{x}}z\mathrm{e}^z \tag{A 17}$$

The first harmonic terms of second order of ϵ in the dynamic surface equation (A 4b) give:

$$A_{11} = B_{11} \tag{A 18}$$

The first harmonic terms of second order of ϵ in the Euler equation and the kinematic surface equation (A 2a–c, A 4a) are respectively:

$$\frac{\partial u_{10}}{\partial \bar{t}} - \mathrm{i}u_{11} + \mathrm{i}u_{10}U = -\frac{\partial p_{10}}{\partial \bar{x}} - \mathrm{i}p_{11} \tag{A 19a}$$

$$\frac{\partial v_{10}}{\partial \bar{t}} - \mathrm{i}v_{11} + \mathrm{i}v_{10}U = -\frac{\partial p_{10}}{\partial \bar{y}} \tag{A 19b}$$

$$\frac{\partial w_{10}}{\partial \bar{t}} - \mathrm{i}w_{11} + \mathrm{i}w_{10}U = -\frac{\partial p_{11}}{\partial z} \tag{A 19c}$$

$$\frac{\partial B_{10}}{\partial \bar{t}} - \mathrm{i}B_{11} + \mathrm{i}UB_{10} = w_{11} \qquad \text{at } z = 0 \tag{A 19d}$$

Using the results (A 8–A 10) from first order and the solution for p_{11} (A 17–A 18), leads to the current modified Schrödinger equation to second order:

$$\frac{\partial B_{10}}{\partial \bar{x}} + 2\frac{\partial B_{1,0}}{\partial \bar{t}} + 2\mathrm{i}UB_{10} = 0 \tag{A 20}$$

and the reconstruction formulas:

$$u_{11} = B_{11}\mathrm{e}^z + \mathrm{i}\left(\frac{\partial B_{10}}{\partial \bar{t}} + \mathrm{i}UB_{10}\right)(1 + 2z)\mathrm{e}^z \tag{A 21a}$$

$$v_{11} = -\mathrm{i}\frac{\partial B_{10}}{\partial \bar{y}}\mathrm{e}^z \tag{A 21b}$$

$$w_{11} = -\mathrm{i}B_{11}\mathrm{e}^z + \left(\frac{\partial B_{10}}{\partial \bar{t}} + \mathrm{i}UB_{10}\right)(1 + 2z)\mathrm{e}^z \tag{A 21c}$$

A.2.3. *Second harmonic*

The second harmonic terms of second order of ϵ for the divergence of the Euler equation (A 3) are:

$$-\frac{1}{2}u_{10}^2 + \frac{1}{2}\left(\frac{\partial w_{10}}{\partial z}\right)^2 + \mathrm{i}\frac{\partial u_{10}}{\partial z}w_{10} = 4p_{20} - \frac{\partial^2 p_{20}}{\partial z^2} \tag{A 22}$$

Using the results (A 10) from leading order, gives:

$$0 = 4p_{20} - \frac{\partial^2 p_{20}}{\partial z^2} \tag{A 23}$$

which has the solution:

$$p_{20} = A_{20}\mathrm{e}^{2z} \tag{A 24}$$

The second harmonic terms of second order of ϵ in the dynamic surface equation (A 4b) are:

$$p_{20} - B_{20} + \frac{1}{2}B_{10}\frac{\partial p_{10}}{\partial z} = 0 \qquad \text{at } z = 0 \tag{A 25}$$

Using the results (A 8–A 9) from leading order and the solution for p_{20} (A 24), gives:

$$A_{20} = B_{20} - \frac{1}{2}B_{10}^2 \tag{A 26}$$

The second harmonic terms of second order of ϵ in the Euler equation and the kinematic surface equation (A 2a–c, A 4) are respectively:

$$-\mathrm{i}u_{20} + \frac{\mathrm{i}}{4}u_{10}^2 + \frac{1}{4}w_{10}\frac{\partial u_{10}}{\partial z} = -\mathrm{i}p_{20} \tag{A 27a}$$

$$-\mathrm{i}v_{20} + \frac{\mathrm{i}}{4}u_{10}v_{10} + \frac{1}{4}w_{10}\frac{\partial v_{10}}{\partial z} = 0 \tag{A 27b}$$

$$-\mathrm{i}w_{20} + \frac{\mathrm{i}}{4}u_{10}w_{10} + \frac{1}{4}w_{10}\frac{\partial w_{10}}{\partial z} = -\frac{1}{2}\frac{\partial p_{20}}{\partial z} \tag{A 27c}$$

$$-\mathrm{i}B_{20} + \frac{\mathrm{i}}{4}u_{10} = \frac{1}{2}w_{20} + \frac{1}{4}B_{10}\frac{\partial w_{10}}{\partial z} \qquad \text{at } z = 0 \tag{A 27d}$$

Using the results (A 10) from first order and the solution for p_{20} (A 24, A 26), gives:

$$u_{20} = v_{20} = w_{20} = p_{20} = 0 \tag{A 28a}$$

$$B_{20} = \frac{1}{2}B_{10}^2 \tag{A 28b}$$

Note that the second order contributions is not explicit functions of the current field.

A.3. *Third order terms*

The first harmonic terms of third order of ϵ for the divergence of the Euler equation (A 3) are:

$$u_{20}u_{10}^* + \frac{1}{2}\frac{\partial w_{20}}{\partial z}\frac{\partial w_{10}^*}{\partial z} - \frac{\mathrm{i}}{2}\frac{\partial u_{20}}{\partial z}w_{10}^* + \mathrm{i}\frac{\partial u_{10}^*}{\partial z}w_{20} + \mathrm{i}u_{10}\frac{\partial U}{\partial \bar{x}} + \mathrm{i}v_{10}\frac{\partial U}{\partial \bar{y}}$$

$$= -\frac{1}{2}\frac{\partial^2 p_{10}}{\partial \bar{x}^2} - \mathrm{i}\frac{\partial p_{11}}{\partial \bar{x}} + \frac{1}{2}p_{12} - \frac{1}{2}\frac{\partial^2 p_{10}}{\partial \bar{y}^2} - \frac{1}{2}\frac{\partial^2 p_{12}}{\partial z^2} \tag{A 29}$$

Using the results (A 8–A 10, A 17–A 18, A 28) from first and second order, gives:

$$\frac{\partial^2 p_{12}}{\partial z^2} - p_{12} = -2\mathrm{i}\frac{\partial B_{11}}{\partial \bar{x}}\mathrm{e}^z - \frac{\partial^2 B_{10}}{\partial \bar{x}^2}\mathrm{e}^z - \frac{\partial^2 B_{10}}{\partial \bar{y}^2}\mathrm{e}^z - 2\frac{\partial^2 B_{10}}{\partial \bar{x}^2}z\mathrm{e}^z - 2\mathrm{i}B_{10}\frac{\partial U}{\partial \bar{x}}\mathrm{e}^z \tag{A 30}$$

which has the solution:

$$p_{1,2} = A_{12}(\bar{x}, \bar{y}, \bar{z}, \bar{t})\mathrm{e}^z + \alpha(\bar{x}, \bar{y}, \bar{z}, \bar{t})z\mathrm{e}^z + \beta(\bar{x}, \bar{y}, \bar{t})z^2\mathrm{e}^z \tag{A 31}$$

where

$$\alpha = -\mathrm{i}\frac{\partial B_{11}}{\partial \bar{x}} - \frac{1}{2}\frac{\partial^2 B_{10}}{\partial \bar{y}^2} - \mathrm{i}B_{10}\frac{\partial U}{\partial \bar{x}}$$

$$\beta = -\frac{1}{2}\frac{\partial^2 B_{10}}{\partial \bar{x}^2}$$

The first harmonic terms of third order of ϵ in the dynamic surface equation (A 4b) are:

$$\frac{1}{2}p_{12} - \frac{1}{2}B_{12} + \frac{1}{4}B_{20}\frac{\partial p_{10}^*}{\partial z} + \frac{1}{4}B_{10}^*\frac{\partial p_{20}}{\partial z} + \frac{1}{2}B_{10}\frac{\partial \bar{p}_1}{\partial z}$$

$$+\frac{1}{2}\zeta\frac{\partial p_{10}}{\partial z} + \frac{1}{16}B_{10}^2\frac{\partial^2 p_{10}^*}{\partial z^2} + \frac{1}{8}|B_{10}|^2\frac{\partial^2 p_{10}}{\partial z^2} = 0 \qquad \text{at } z = 0 \qquad \text{(A 32)}$$

Using the results (A 8–A 9, A 13, A 28–A 28) from first and second order, and the solution for p_{12} (A 31), gives:

$$A_{12} = B_{12} + \frac{3}{8}B_{10}^2 B_{10}^* - B_{10}\zeta \qquad \text{at } z = 0 \qquad \text{(A 33)}$$

The first harmonic terms of third order of ϵ in the Euler equation and the kinematic surface equation (A 2a–c, A 4a) are respectively:

$$\frac{1}{2}\frac{\partial u_{11}}{\partial \bar{t}} - \frac{\mathrm{i}}{2}u_{12} + \frac{1}{2}\frac{\partial u_{10}}{\partial \bar{x}}U + \frac{\mathrm{i}}{2}u_{11}U + \frac{1}{2}\frac{\partial u_{10}}{\partial \bar{y}}V + \frac{1}{2}u_{10}W + \frac{1}{2}u_{10}\frac{\partial U}{\partial \bar{x}} + \frac{1}{2}v_{10}\frac{\partial U}{\partial \bar{y}}$$

$$-\frac{\mathrm{i}}{4}u_{20}u_{1,0}^* + \frac{\mathrm{i}}{2}u_{10}^*u_{20} + \frac{1}{4}w_{20}\frac{\partial u_{10}^*}{\partial z} + \frac{1}{4}w_{10}^*\frac{\partial u_{20}}{\partial z} = -\frac{1}{2}\frac{\partial p_{11}}{\partial \bar{x}} - \frac{\mathrm{i}}{2}p_{12} \qquad \text{(A 34a)}$$

$$\frac{1}{2}\frac{\partial v_{11}}{\partial \bar{t}} - \frac{\mathrm{i}}{2}v_{12} + \frac{1}{2}\frac{\partial v_{10}}{\partial \bar{x}}U + \frac{\mathrm{i}}{2}v_{11}U + \frac{1}{2}\frac{\partial v_{10}}{\partial \bar{y}}V + \frac{1}{2}v_{10}W + \frac{1}{2}u_{10}\frac{\partial V}{\partial \bar{x}} + \frac{1}{2}v_{10}\frac{\partial V}{\partial \bar{y}}$$

$$-\frac{\mathrm{i}}{4}u_{20}v_{10}^* + \frac{\mathrm{i}}{2}u_{10}^*v_{20} + \frac{1}{4}w_{20}\frac{\partial v_{10}^*}{\partial z} + \frac{1}{4}w_{10}^*\frac{\partial v_{20}}{\partial z} = -\frac{1}{2}\frac{\partial p_{11}}{\partial \bar{y}} \qquad \text{(A 34b)}$$

$$\frac{1}{2}\frac{\partial w_{11}}{\partial \bar{t}} - \frac{\mathrm{i}}{2}w_{12} + \frac{1}{2}\frac{\partial w_{10}}{\partial \bar{x}}U + \frac{\mathrm{i}}{2}w_{11}U + \frac{1}{2}\frac{\partial w_{10}}{\partial \bar{y}}V + \frac{1}{2}w_{10}W$$

$$-\frac{\mathrm{i}}{4}u_{20}w_{10}^* + \frac{\mathrm{i}}{2}u_{10}^*w_{20} + \frac{1}{4}w_{20}\frac{\partial w_{10}^*}{\partial z} + \frac{1}{4}w_{10}^*\frac{\partial w_{20}}{\partial z} = -\frac{1}{2}\frac{\partial p_{12}}{\partial z} \qquad \text{(A 34c)}$$

$$\frac{1}{2}\frac{\partial B_{11}}{\partial \bar{t}} - \frac{\mathrm{i}}{2}B_{12} - \frac{\mathrm{i}}{4}u_{20}B_{10}^* + \frac{\mathrm{i}}{2}u_{10}^*B_{20} + \frac{\mathrm{i}}{2}B_{11}U$$

$$+\frac{1}{2}\frac{\partial B_{10}}{\partial \bar{x}}U + \frac{1}{2}\frac{\partial B_{10}}{\partial \bar{y}}V + \frac{\mathrm{i}}{8}B_{10}^2\frac{\partial u_{10}^*}{\partial z}$$

$$= \frac{1}{2}w_{12} + \frac{1}{4}B_{20}\frac{\partial w_{10}^*}{\partial z} + \frac{1}{2}B_{10}^*\frac{\partial w_{20}}{\partial z} + \frac{1}{2}\zeta\frac{\partial w_{10}}{\partial z}$$

$$+\frac{1}{16}B_{10}^2\frac{\partial w_{10}^*}{\partial z} + \frac{1}{8}|B_{10}|^2\frac{\partial^2 w_{10}}{\partial z^2} \qquad \text{at } z = 0 \qquad \text{(A 34d)}$$

Combining these equations with the results (A 10, A 17–A 18, A 21, A 28) from first and second order, and the solution for p_{12} (A 31, A 33), gives:

$$0 = \frac{\partial B_{11}}{\partial \bar{x}} + 2\frac{\partial B_{11}}{\partial \bar{t}} + \mathrm{i}\frac{\partial^2 B_{10}}{\partial \bar{t}^2} - \frac{\mathrm{i}}{2}\frac{\partial^2 B_{10}}{\partial \bar{y}^2} + \mathrm{i}B_{10}^2 B_{10}^*$$

$$+2\mathrm{i}B_{11}U - 6\frac{\partial B_{10}}{\partial \bar{t}}U - 5\mathrm{i}B_{10}U^2 + 2\frac{\partial B_{10}}{\partial \bar{y}}V + B_{10}\frac{\partial U}{\partial \bar{x}} \qquad \text{(A 35)}$$

which combined with (A 20) leads to the space evolution of the current modified cubic

nonlinear Schrödinger equation, NLSC, (2.5) where $B = B_1$ and the bars are dropped to simplify the notation.

More on the derivation of the NLSC equation can be found in Hjelmervik & Trulsen (2009).

REFERENCES

BOTTIN, R. R. JR. & THOMPSON, E. F. 2002 Comparisons of physical and numerical model wave predictions with prototype data at Morro Bay harbor entrance, California. *U. S. Army Engineer.*

DYSTHE, K. B. 1979 Note on the modification to the nonlinear Schrödinger equation for application to deep water waves. *Proc. R. Soc. Lond. A* **369**, 105–114.

DYSTHE, K. B., KROGSTAD, H. E. & MÜLLER, P. 2008 Oceanic Rogue Waves. *Annu. Rev. Fluid Mech.* **40**, 287–310.

GERBER, M. 1987 The Benjamin–Feir instability of a deep water Stokes wavepacket in the presence of a non–uniform medium. *J. Fluid Mech.* **176**, 311–332.

GONZÁLEZ, F. I. 1984 A case study of wave–current–bathymetry interactions at the Columbia river entrance. *J. Phys. Oceanogr.* **14**, 1065–1078.

GRAMSTAD, O. & TRULSEN, K. 2007 Influence of crest and group length on the occurrence of freak waves. *J. Fluid Mech.* **582**, 463–472.

HJELMERVIK, K., OMMUNDSEN, A. & GJEVIK, B. 2005 Implementation of non–linear advection terms in a high resolution tidal model. *University of Oslo, preprint.*

HJELMERVIK, K., LYNGE, B. K., OMMUNDSEN, A. & GJEVIK, B. 2008 Interaction of tides and storm surges in the Tjeldsunet channel in northern Norway. *Ocean Dynamics* (submitted).

HJELMERVIK, K. & TRULSEN, K. 2009 The current modified nonlinear Schrödinger equation which allows vorticity. *University of Oslo, preprint,* (to be submitted).

JONSSON, I. G. 1990 Wave–current interactions. In *The Sea, Ocean Eng. Sci.* (ed. by B. Le Mhaut & D. M. Hanes), pp. 65–120, Wiley-Interscience, Hoboken, N. J.

KHARIF, C. & PELINOVSKY, E. 2003 Physical mechanisms of the rogue wave phenomenon. *Eur. J. Mech. B/Fluids* **22**, 603–634.

LAVRENOV, I. V. 1998 The wave energy concentration at the Agulhas current off South Africa. *Natural Hazards* **17**, 117–127.

LAVRENOV, I. V. & PORUBOV, A. V. 2006 Three reasons for freak wave generation in the non–uniform current. *Eur. J. Mech. B/Fluids* **25**, 574–585.

LO, E. Y. & MEI, C. C. 1985 A numerical study of water–wave modulation based on a higher–order nonlinear Schrödinger equation. *J. Fluid Mech.* **150**, 395–416.

LONGUET–HIGGINS, M. S. & STEWART, R. W. 1961 The changes in amplitude of short gravity waves on steady non–uniform currents. *J. Fluid Mech.* **10**, 529–549.

MACIVER, R. D., SIMONS, R. R. & THOMAS, G. P. 2006 Gravity waves interacting with narrow jet–like current. *J. Geophys. Res.* **111**, C03009.

MACMAHAN, J. H., THORNTON, E. B. & RENIERS, A. J. H. M. 2006 Rip current review. *Coastal Engineering* **53**, 191–208.

MEI, C. C. 1989 The applied dynamics of ocean surface waves. *World Scientific Publishing Co., Singapore.*, ISBN 9971–50–789–7

MORI, N., LIU, P. C. & YASUDA, T. 2002 Analysis of freak wave measurements in the sea of Japan. *Ocean Engineering* **29**, 1399–1414.

MUSLU, G. M. & ERBAY, H. A. 2004 Higher–order split–step Fourier schemes for the generalized nonlinear Schrödinger equation. *Mathematics and Computers in Simulation* **67**, 581–595.

ONORATO, M., OSBORNE, A. R., SERIO, M., RESIO, D., PUSHKAREV, A., ZAKHAROV, V. E. & BRANDINI, C. Freely decaying weak turbulence for sea surface gravity waves. *Phys. Rev. Lett.* **89**, 144501.

PEREGRINE, D. H. 1976 Interaction of water waves and currents. *Adv. Appl. Mech.* **16**, 9–117.

PEREGRINE, D. H. & SMITH, R. 1979 Nonlinear effects upon waves near caustics. *Phil. Trans. R. Soc. Land. A* **292**, 341–370.

SOCQUET–JUGLARD, H., DYSTHE, K. B., TRULSEN, K., KROGSTAD, H. E. & LIU, J. 2005

Probability distributions of surface gravity waves during spectral changes. *J. Fluid. Mech.* **542** 195–216.

STEWARTSON, K. 1977 On the resonant interaction between a surface wave and a weak surface current. *Mathematika* **24**, 37–49.

STOCKER, J. D. & PEREGRINE, D. H. 1999 The current–modified nonlinear Schrödinger equation. *J. Fluid Mech.* **399**, 335–353.

TAYFUN, M. A. 1980 Narrow-band nonlinear sea waves. *J. Geophys. Res.* **85**, 1548–1552.

TRULSEN, K. & DYSTHE, K. B. 1996 A modified nonlinear Schrödinger equation for broader bandwidth gravity waves on deep water. *Wave Motion* **24**, 281–289.

TURPIN, F–M., BENMOUSSA, C. & MEI, C. C. 1983 Efects of slowly varying depth and current on the evolution of a Stokes wavepacket. *J. Fluid Mech.* **132**, 1–23.

WHITE, B. S. & FORNBERG, B. 1998 On the chance of freak waves at sea. *J. Fluid Mech.* **335**, 113–138.

WHITE, B. S. 1999 Wave action on currents with vorticity. *J. Fluid Mech.* **386**, 329–344.

WU, C. H. & YAO A. 2004 Laboratory measurements of limiting freak waves on currents. *J. Geophys. Res.* **109**, C12002.

ZAKHAROV, V. E. 1968 Stability of periodic waves of finite amplitude on the surface of a deep fluid. *J. Appl. Mech. Tech. Phys.* **9**, 86–94.